Multiscale simulations in organic electronics: Applications to polymer wrapping of single-walled carbon nanotubes, bulk charge mobilities and organic-organic interfaces

Angela Poschlad
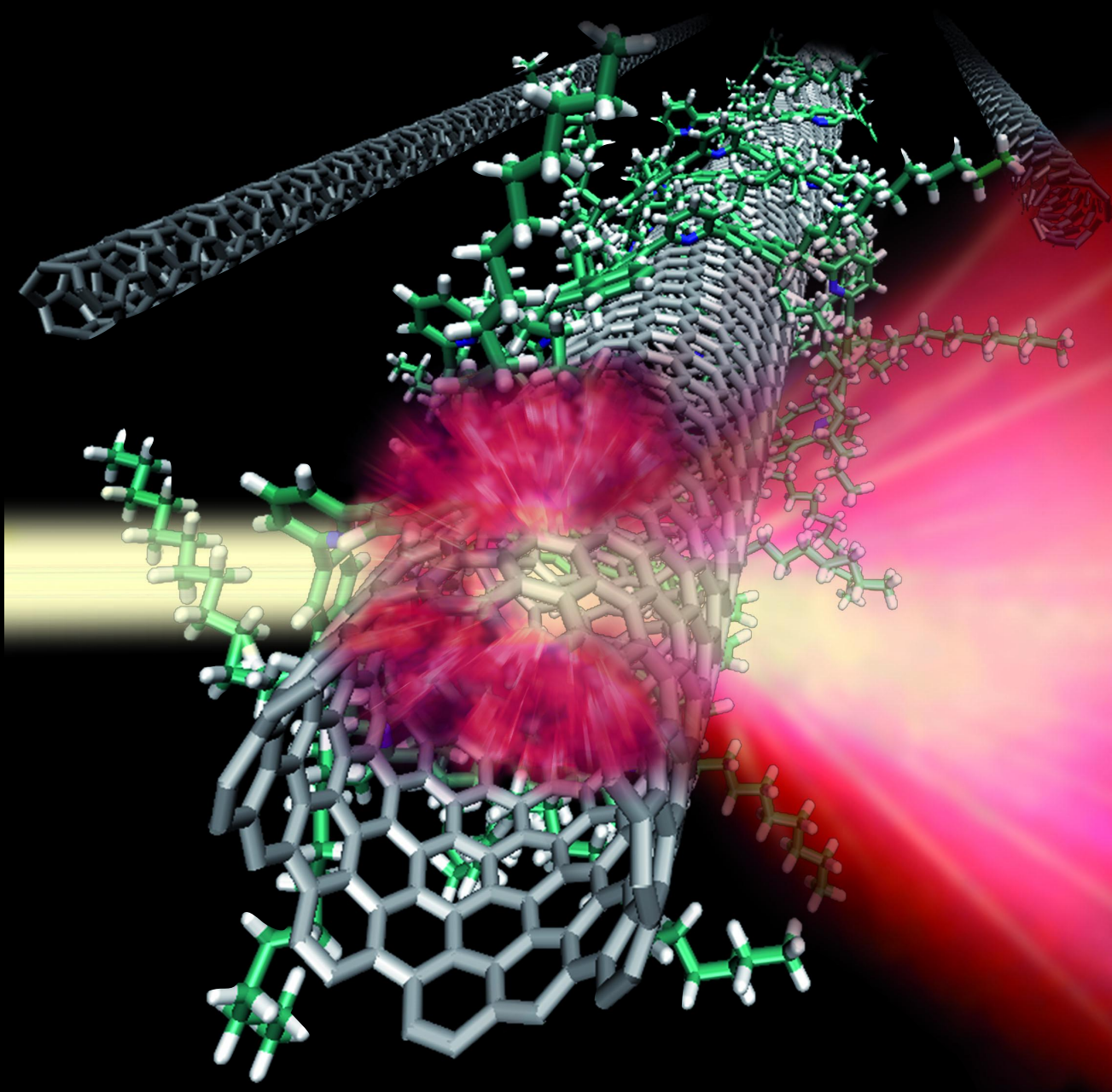
Multiscale simulations in organic electronics: Applications to polymer wrapping of single-walled carbon nanotubes, bulk charge mobilities and organic-organic interfaces

Zur Erlangung des akademischen Grades eines

DOKTORS DER NATURWISSENSCHAFTEN

von der Fakultät für Physik des
Karlsruher Instituts für Technologie

genehmigte

DISSERTATION

von

Dipl. Phys. Angela Poschlad
aus Hattingen a.d. Ruhr

Tag der mündlichen Prüfung: 27.06.2014
Referent: Prof. Dr. Wolfgang Wenzel
Korreferent: Prof. Dr. Gerd Schön

Contents

Contents

1. Introduction

Modern life without electronic devices is not imaginable as they penetrate every aspect of our lives. Many children, for example, cannot imagine a life without their smartphones and modern hospitals are unthinkable without electronic equipment. With declining use of incandescent light bulbs, even modern light sources will soon have their own integrated circuit.

All modern electronic devices are based on transistors. The first patents on the so called solid-state amplifier, *i.e.* the solid-state field effect transistor (FET), were filed by Lilienfeld in 1925-1928 [1–3] and Heil in 1934 [4]. Lilienfeld describes his concept as "a method of and apparatus for controlling the flow of an electric current between two terminals of an electrically conducting solid by establishing a third potential between said terminals" [1]. In the 1940s, Haynes and Shockley experimented at Bell Telephone Laboratories with Germanium-crystal-based transistors [5]. The use of transistors enabled the creation of the 'second generation' of computers [6]. "For their researches on semi-conductors and their discovery of the transistor effect", Shockley, Bardeen and Brattain were jointly awarded the Nobel Prize in Physics in 1956 [7].

Technological advances in transistor design and the significant reduction of production costs per unit triggered an astounding boost in electronics applications. This development led Moore to recognize and forecast a constant exponential rise in the number of electronic components per integrated circuit (IC) as early as 1965 [8]. His prediction came true and today this trend - shown by Wgsimon[1] in Figure 1.1[2] - is well known as "Moore's Law".

The observed exponential trend is largely driven by a rapidly miniaturization process of transistor components. Current processing units are based on transistors that are only a few nanometers in diameter [9], while in 1972, the production of a modern metal-oxide-semiconductor field-effect transistor (MOSFET) involved a 10 micrometer process [10].

---

[1]Wgsimon: http://commons.wikimedia.org/wiki/User:Wgsimon
[2]CC BY-SA 3.0: http://creativecommons.org/licenses/by-sa/3.0/legalcode

Microprocessor Transistor Counts 1971-2011 & Moore's Law

Figure 1.1.: Transistor counts in dependence of the dates of introduction. The development overt time shows an constant exponential rise. By Wgsimon (CC BY-SA 3.0)

Today, modern smartphones and other wearables (wearable electronic devices) have computing power that is comparable to early supercomputers, *e.g.* the smartphone Samsung I5500 Galaxy 5 reaches in the Linpack benchmark [11] roughly 10 Mflops [12] while the supercomputer CRAY-1, built in 1976, reached 12 Mflops. In comparison, the Cray XK7, built in 2012,[3] has 17.59 Pflops, *i.e.* $17.59 \cdot 10^9$ Mflops.

With rising computing power, more precise simulation methods and simulation of larger system sizes have become feasible, enabling the study of nature in far greater detail, ranging from quantum dot problem to full airplane simulation. The importance of materials simulation to the scientific community at large was particularly emphasized when advances in modeling molecular systems were awarded with the last years Nobel Prize in

---

[3]At the time of this writing, this is the highest Cray in the top 10 list of supercomputers

Chemistry in 2013. Martin Karplus, Michael Levitt and Arieh Warshel received the prize for their development of multiscale models for complex chemical systems [13].

In search of new, more efficient and cheaper materials, research groups began looking at organic semiconductors as device layers in the 1980s. In 1987, the first so-called organic electroluminescent diodes (OLEDs) were reported by Tang *et al.* [14]. 25 years later the more advanced version of this technology, active-matrix organic light-emitting diodes (AMOLED) can be found in selected television and smartphone displays [15].

Materials used in organic electronic devices differ substantially in their nature from their inorganic counterparts. Many devices use materials based on small molecules, such as pentacene, some are based on polymers and others require robust single-walled carbon nanotubes (SWCNTs) [16]. Their intrinsic properties can also differ, *e.g.* while crystalline materials are known to possess a high charge carrier mobility [17], amorphous semiconductors typically have a charge mobility that is several orders of magnitude lower [18]. High charge carrier mobility is important for efficient charge separation at the interface of organic photovoltaic devices. The longer the transport of the exciton takes to travel to the interface, *i.e.* the donor-acceptor heterojunction, the higher is the chance of recombination leading to decrease in charge collection efficiency. In transistors and OLEDs, the charge mobility therefore determines the response time, short transit time, and maximal switching frequency [19].

While organic electronic devices are already present in industrial-grade devices, many fundamental aspects of the underlying physics are still largely unknown. Consequently, there has been great interest in understanding and ultimately predicting the behavior of organic electronic components in the material simulation community with the goal of improving the design process of these components [20–22]. Simulations, in addition to being a cost efficient materials pre-screening tool, can offer insights that are not available through experiments.

One of the challenges is the identification and fabrication of organic surrogates for inorganic semiconductors. Unfortunately, organic materials often possess less attractive properties compared to their inorganic counterparts. For example, the typical charge mobility of organic semiconductors is much smaller than, for example, the charge mobility of silicon. As the charge mobility is responsible for the limitation in response time of devices and essential for efficient photovoltaics, organic materials with high charge carrier mobility are needed. Therefore, it is important to develop a model, which is capable of predicting charge mobility. In this thesis, a new developed model for charge mobility

prediction is applied to amorphous and crystalline organic semiconductors and the results are compared with experimental data ranging over many orders of magnitude.

Once a promising material was identified, the candidate is checked for ways into mass-production. For the single-walled carbon nanotubes, which have phenomenal properties, production of chemically pure species with respect to diameter and chirality remains challenging. SWCNTs have intrinsic properties depending on their diameter and angular pattern [23] and therefore need purification for successful application. Single-walled carbon nanotubes cannot be synthesize selectively in an inexpensive way and do not reach the purity accustomed to, for example, inorganic materials. Instead, mixtures of miscellaneous nanotubes are commonly produced [24, 25].

For this reason, many sorting procedures for SWCNTs have been explored [26, 27]. One widely explored idea is the development of molecules that selectively bind only to specific SWCNTs, which may then easily be separated by centrifugation. While the use of DNA [28] was found to be a powerful tool, it is too expensive for mass-production. Thus, polymers were tested [29–38], which have some similarities to DNA, but are less expensive and can easily be produced efficiently and cheaply.

In our days, the search of selective polymers requires extensive synthesis and experiments for each candidate. To reduce the number of these costly experiments reliable simulation methods would be very helpful. Previous simulations focused only on one or few polymers and tend to reach qualitative results at best [29, 33] because the time-scale of polymer wrapping is very large. In this thesis, a new multiscale model is developed to simulate the wrapping of polymers on single-walled carbon nanotubes. This model aims to predict the selectivity of polymers towards SWCNTs. At the example of conjugated polymers with different complexity, this model is tested and compared to experimental data.

The utilization of organic materials results in new types of interfaces within a device, *e.g.* organic-organic and organic-inorganic. The simulation of processes at organic-organic interfaces proved challenging [20] and often only idealized systems are analyzed. For a better understanding, realistic interface morphologies are required. Also the transition from bulk to interface region is of high interest. In this work, the extension of the interface into the bulk material is analyzed for different material orientations at the interface.

To summarize, this thesis focuses on three aspects involving multiscale materials simulation: the first topic of research addresses the estimation of charge carrier mobilities in organic semiconductors via a sophisticated ab-initio workflow. Second, simulation of

realistic morphologies of organic-organic crystalline interfaces is described. Finally, the simulation of the ability of polymers to sort SWCNTs is addressed.

In more detail, the structure of the thesis is as follows: first, in Chapter 2, a general theoretical framework for understanding the presented work is established. The chapter presents an overview to the subject areas that form the foundation for the rest of the thesis, including the concepts to describe hopping transport of charge carriers in organic semiconductors and important aspects involved in organic heterojunctions. Furthermore, an overview of the application and production of single-walled carbon nanotubes is given. Additionally, the second chapter includes a new coarse-grained approach to model the wrapping of polymers on single-walled carbon nanotubes. While many theoretical studies make qualitative statements regarding how polymers wrap themselves around SWCNTs [29–38], the new model yields quantitative results by covering the whole configuration space of polymers on each SWCNT at feasible costs.

The topics require the simulation of molecules and molecular systems on various length scales, whereby, each one requires a different model and method. Therefore, chapter 3 introduces the main computational methods and applications used for the simulation of different length scales. Density Functional Theory (DFT) is presented first, followed by an explanation of the MNDO method. Afterwards, the concepts of Molecular Dynamics, classical force fields and the essential simulation methods are discussed.

Chapter 4 focuses on the calculation of the intrinsic charge carrier mobility of organic semiconductors, which is especially important to OLEDs [39–41]. While a number of phenomenological semi-analytical models were developed [42], this thesis uses the new analytical formula that can directly incorporate data from first principles simulations [43] to analyze the mobility. In order to test this approach, a complex *ab-initio* based workflow was developed and applied to seven different organic materials, five of which are amorphous and two are crystalline materials. Computations of the required quantum mechanical material properties, namely, the reorganization energy, the electronic coupling parameter and the local energy disorder, have been performed from DFT calculations. The influence of the input morphology is analyzed as well as the impact of different DFT functionals and basis sets. This allows for an estimate of the quality of the predicted charge carrier mobility.

After examining the charge carrier mobility, the thesis turns from the intrinsic material bulk properties towards organic interfaces. Many processes in organic devices take place at the interface and therefore a profound knowledge of realistic interface morphology is of

high importance [20]. In Chapter 5 the simulations of realistic morphologies of organic-organic interfaces are analyzed at the example of two crystalline materials. The aim is the identification of disorder regions and their dependence on the crystal planes facing the interface.

Chapter 6 deals with the interface between single-walled carbon nanotubes and conjugated polymers. It addresses the polymer aided sorting process of single-walled carbon nanotubes in respect to their diameter. The new model developed in section 2.5 describing the wrapping process with only few parameters is applied. In contrast to many MD studies on polymer wrapping, the coarse-grained model can span the whole configuration space for polymers on each SWCNT making quantitative predictions possible [44, 45]. At the example of four pyridine containing co-polymers and two more complex 9,9-dioctylfluorene containing co-polymers the polymer wrapping model is tested against experimental data.

The thesis concludes with a summary of the work in Chapter 7 including an outlook for continuing work on possible improvements.

2. General theoretical framework

The theoretical background forming the foundation of this thesis is presented in this chapter and the requirements of the thesis specific workflows are outlined.

A successful study in molecular materials simulations often includes the combination of several simulation steps with a number of very different approaches. A general overview on simulations of multiple scales and the connection of the given theoretical models with the required level of detail in the simulated systems are given. Section 2.2 then, describes the requirements in detail and the complexity of the workflow for estimating the charge carrier mobility in organic materials with charge carrier hopping. Afterwards, disorder at organic-organic interfaces is introduced. Section 2.4 presents single-walled carbon nanotubes and, their applications and challenges in utilizing them. Finally, a new model for describing the wrapping process of polymers around single-walled carbon nanotubes is developed from scratch, which will be used in a later chapter to predict the selectivity of the polymers towards nanotubes, facilitating thereby the nanotube sorting.

2.1. Simulating on multiple scales

Multiscale modeling of materials is one of the important aspects in successfully simulate and calculate materials properties and phenomena. Each simulation and the problem addressed with it, has its own optimal model to be treated with as shown in Figure 2.1, and the treatment of most physical effects requires the combination of several models.

A reasonable choice of model largely depends on the length scale and, for time dependent problems, on the duration of the investigated phenomenon. In general, the larger the system size and the longer the simulated time, the larger the need for generalization and approximation within the model. Small systems with few atoms and electrons on short time scales can be treated with full quantum mechanical models in a feasible manner. For systems that are more complex atomistic models focusing on classical treatment of
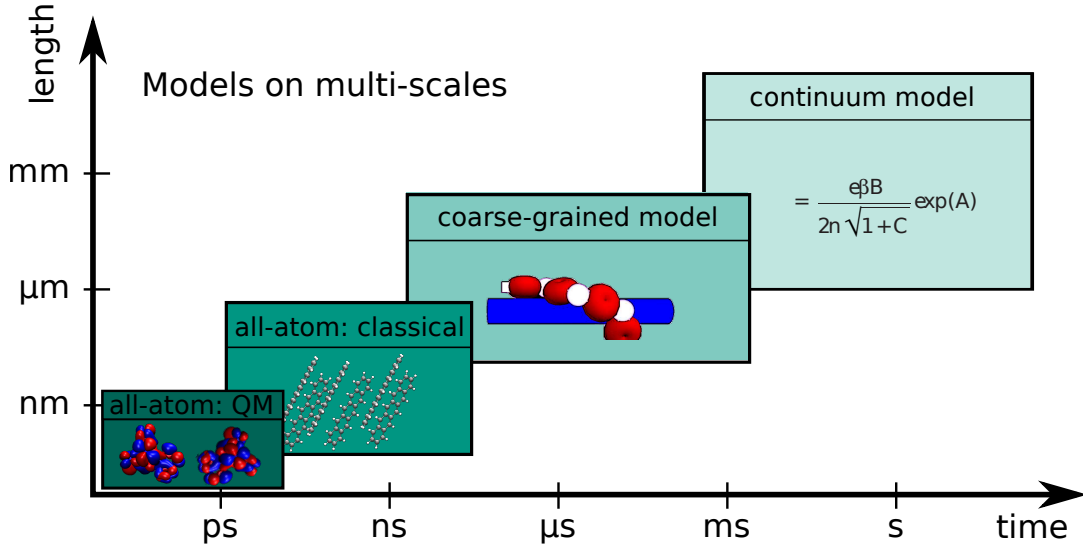
Figure 2.1.: Schematic overview of models employed on different length and time scales. Depending on the length scale indicated on the y-axis and time dependence of problems given on the x-axis different models are applied. Small systems with a few atoms and on short time scales are best treated by quantum mechanical (QM) all-atom models such as density functional theory. For larger systems that are usually more complex classical all-atom models such as Molecular Dynamics can be used. With large size and complexity it might be beneficial to use roughly approximating coarse-grained models and for slow phenomena and large scales of more than few μm continuous models are best utilized.

atoms can be used. Such force field based models typically grow with $O(N^2)$. Thus, with increasing system size and complexity, it might become beneficial to use averaging coarse-grained models and for slow phenomena and large scales of more than a few μm continuous models are best employed.

All-atom: Quantum mechanical model Quantum mechanical (QM) models focus on the electrons in the system and on solving the time-independent Schrödinger equation

$$H\Psi = E\Psi \tag{2.1}$$

where H is the Hamilton operator, E the system's energy and Ψ the wave function. This leads to a tightly coupled many-body problem with a high number of degrees of freedom. The equation is only solvable for simple cases with only a few particles involved. Consequently, methods using this model require simplifications and potent assumptions. A widely used method is the Density Functional Theory described in chapter 3.1.

All-atom: Classical atomistic model   For larger systems with many atoms and molecules the importance of QM effects declines and the system can be treated with classical all-atom models. Unlike the QM models, classical models focus on the atoms in the system and replace single electrons with effective potentials. The motion is handled by classical mechanics through various potentials representing different aspects of interactions. While QM focuses on the Schrödinger Equation, Molecular Dynamics (MD) is based on classical mechanics, especially on Newton's second law

$$m\ddot{x} \;=\; -\nabla_x V(x) \tag{2.2}$$

with the atomic mass m, the second time derivative of position x, the nabla operator ∇ and the potential V depending on the position x. The well-known method of this model is Molecular Dynamics described in chapter 3.3.

Coarse-Grained models   Coarse-graining can mean using highly abstracted units and leaving out many details. A comprehensive overview on "coarse-grained modeling of soft condensed matter" can be found Reference in [46]. Owing to the lowered number of objects and therefore the reduced number of degrees of freedom the simulations become less resource intensive while the accuracy for specific problems can be kept. This enables researching of new fields and problems which cannot be addressed by QM or atomistic models. Coarse-graining has to be done carefully, to avoid the loss of important aspects of the phenomena studied. Many different coarse-grained models (CG) have been developed [47–53]. However, the reusability of these models is low owing to the specialized nature of the problems.

As an example of coarse-graining, the development of a new CG model can be followed in Section 2.5 where the polymer wrapping around single-walled carbon nanotubes is explained step by step.

Continuous models   Continuous models are characterized by parametrized equations, *e.g.* for calculating macroscopic properties, such as the charge carrier mobility. The parameters can be obtained from experimental data or calculated, approximated etc. by other methods. Continuous models assume well-behaved characteristics within the scope of application.

2.2. Charge carrier mobility in organic semiconductors

Charge carrier mobility plays a significant role in most electronic devices. While the charge mobility is an intrinsic material quantity, the underlying process takes place on molecular level. In organic materials in van-der-Waals regime with weakly coupled molecules, hopping transport is the dominating effect, i.e. by charge hopping from one molecule i to the next molecule j.

2.2.1. From Markus theory to charge mobility

The hopping process can be described by the Master Equation [39, 43]

$$\frac{dp_i}{dt} = \sum_i p_i \omega_{ij}(1 - p_i) - p_i \omega_{ij}(1 - p_j) \tag{2.3}$$

with p_i being the probability of a charge on molecule i, ω_{ij} the hopping rate for a charge transfer from molecule i to molecule j. The sum over all probabilities is equal to the number of charge carriers in the system $\sum_i p_i = N_{carriers}$.

The theoretical foundation for rates in this hopping process was developed by Marcus in 1956 [40]. "For his contributions to the theory of electron transfer reactions in chemical systems" the Royal Swedish Academy of Sciences awarded the Nobel Prize in Chemistry in 1992 to Marcus [54]. The charge carrier transfer rate, or Marcus rate, is given by equation

$$\omega_{if} = \frac{2\pi}{\hbar} |J_{if}|^2 \sqrt{\frac{\beta}{4\pi\lambda}} \exp\left(-\beta \frac{(\lambda + \Delta E)^2}{4\lambda}\right) \tag{2.4}$$

Next to the different constants, such as $\beta = \frac{1}{k_B T}$ and $\hbar$ defined as Planck constant h divided by 2π, three material parameters are used: the reorganization energy λ, the electronic coupling J_{ij} and the energy disorder ΔE.

Rodin *et al.* derived an analytical formula for an upper bound charge carrier mobility estimation based on effective medium theory [43]. They solved the Master Equation using the Marcus rates and concluded the formula

$$\mu = \frac{e\sqrt{\pi}(\beta\lambda)^{3/2}}{2n\hbar\sqrt{1 + \frac{\beta\sigma^2}{\lambda}}} exp\left[-\frac{(\beta\sigma)^2}{4} - \beta\frac{\lambda}{4}\right] M \frac{\langle J^2 r^2 \rangle}{\lambda^2} \tag{2.5}$$

This equation includes the elementary charge e, the dimension n, and four material parameters, namely the effective reorganization energy λ, the averaged electronic coupling

$\langle J^2 r^2 \rangle$, the effective energy disorder σ and the average number of hopping partners per molecule M.

2.2.2. Modular multiscale workflow for charge carrier mobility

The calculation of charge carrier mobility requires understanding of the effects on molecular level. All material specific parameters required by Equation 2.5 are calculated by *ab-initio* methods but rely on a realistic morphology to work on. In general, there are three major parts in the workflow requiring distinct methods and models.

1. Generation of a realistic morphology (DFT, MD)

2. QM parameter determination (DFT)

3. Application of analytical formula (Continuous model)

2.2.2.1. Generation of realistic morphologies with Molecular Dynamics

The modeling of a realistic morphology depends on the material. For crystals on the one hand, the easiest way to obtain the crystal structure is the usage of the Cambridge Crystallographic Data Centre (CCDC) [55] which contains "the information on many hundred thousands of crystal structure information". The structure itself can be assembled *e.g.* by the Mercury package [56]. On the other hand, amorphous semiconductors can be modeled using either Molecular Dynamics, introduced in Chapter 3.3, or molecular deposition based on Monte Carlo code [57]. The amorphous structures described and analyzed for their charge carrier mobility were prepared with the Molecular Dynamics package GROMACS [58–61] using the rapid cooling approach described in section 3.3.2.

2.2.2.2. QM parameter from first principles

On realistic morphologies the hopping process of charge carrier transfer can be studied. Therefore, a profound understanding and treatment of effects on molecular level is required. In this work all essential material parameters are calculated from *first principles*, meaning no experimental data or fitting is used. The procedures for obtaining the four effective parameters

- (Effective) reorganization energy λ

2. General theoretical framework

- Electronic coupling parameter $\langle J^2 r^2 \rangle$

- Average transfer partners per hopping site M

- (Effective) energy disorder σ

are implemented in a tool called Shredder (Research group Wenzel, Institute of Nanotechnology, Karlsruhe Institute of Technology) based on DFT methods, which are described in chapter 3.1. In the following text, the methods and ideas behind the procedures in Shredder are discussed starting with the reorganization energy λ, followed by an insight to the electronic coupling calculations of molecule pairs and at last the energy disorder σ treatment.

Reorganization energy   The reorganization energy λ for the charge hopping process describes the energy required to relax the molecular structure when changing the number of electrons, *i.e.* when adding or taking away one electron as illustrated in Figure 2.2. The figure shows the schematic energy profiles as harmonic potentials for two orbitals dependent on the molecule's geometry with four highlighted points. Point 1 represents the ground-state energy $E(1)$ of the relaxed neutral molecule. When charging, the energy level $E(2)$ at point 2 is reached. Point 3 represents the energy $E(3)$ of the charged molecule in the relaxed structure. Finally, point 4 marks the energy $E(4)$ of the neutral molecule in the molecule structure of point 3.

The reorganization energy λ results from the energy difference of $E(2)$ and $E(3)$:

$$\lambda = E(2) - E(3) \tag{2.6}$$

In a charge transfer (hopping) process two molecules are involved. Therefore, the required effective material parameter λ_{eff} for the mobility calculation has to combine the reorganization energies from both molecule relaxations. This is done by summing up both reorganization energies. The calculation of the effective reorganization energy - here for hopping in pure materials - is done in four DFT steps [62].

1. Relaxation of neutral molecule in vacuum ($E_{\text{neutral, relaxed}} = E(1)$)

2. Single point calculation of charged molecule on the relaxed geometry of the neutral molecule ($E_{\text{charged, fixed}} = E(2)$)

3. Relaxation of charged molecule in vacuum ($E_{\text{charged, relaxed}} = E(3)$)
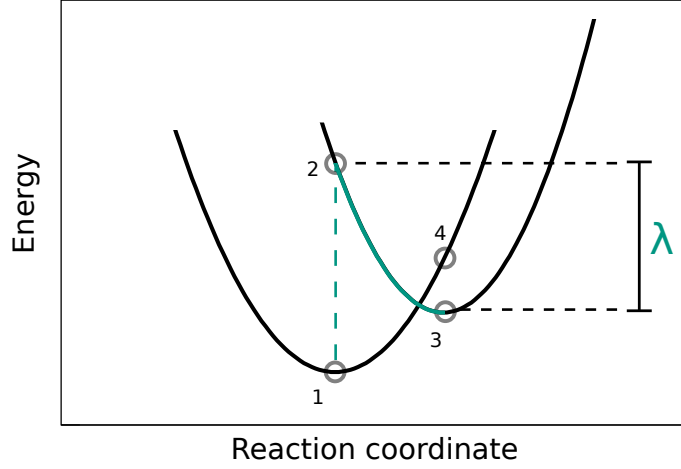
Figure 2.2.: Schematic diagram of charge carrier hopping to obtain the reorganization energy λ assuming harmonic potential energy surfaces of the neutral and charged states of the molecule. Four points are marked by gray circles: Point 1 marks the ground-state energy of the relaxed structure of the uncharged molecule. Point 2 represents the energy of the molecule geometry of point 1 but charged, with only the electronic orbital structure relaxed. The third point marks the energy of the geometrically and electronically relaxed charged structure. And finally, point 4 shows the uncharged energy of the charged relaxed geometry. The reorganization energy than is calculated by $\lambda = E(2) - E(3)$.

4. Single point calculation of neutral molecule on the relaxed geometry of the charged molecule ($E_{\text{neutral, fixed}} = E(4)$)

The effective reorganization energy is calculated using Equation 2.7.

$$\lambda_{eff} = \lambda_1 + \lambda_2 = E(2) - E(3) + E(4) - E(1) \tag{2.7}$$

The DFT calculations to obtain the energies $E(1)$ to $E(4)$ do not rely on harmonic potential approximations as shown in the schematic in Figure 2.2. Instead, the accurate energies are calculated. In the following work the reorganization energy λ always refers to the effective reorganization energy λ_{eff} combining the energies of both molecules taking part in the hopping process.

Electronic coupling and average number of hopping partners   The electronic coupling J_{ij} [63, 64] between the molecule pairs (i, j) determines the hopping process on molecular

2. General theoretical framework

layer as illustrated in Figure 2.3 a). The coupling is calculated according to

$$J_{ij} = \frac{F_{ij} - \frac{1}{2}(F_{ii} + F_{jj})S_{ij}}{1 - S_{ij}S_{ij}} \tag{2.8}$$

with the orbital overlap integral $S_{ij} = \int \phi_i^* \phi_j dr - \delta_{ij}$ for the orbitals ϕ_i and the Fock matrices F_{ij}. The larger the orbital coupling, the higher the probability of charge transport between the molecules.
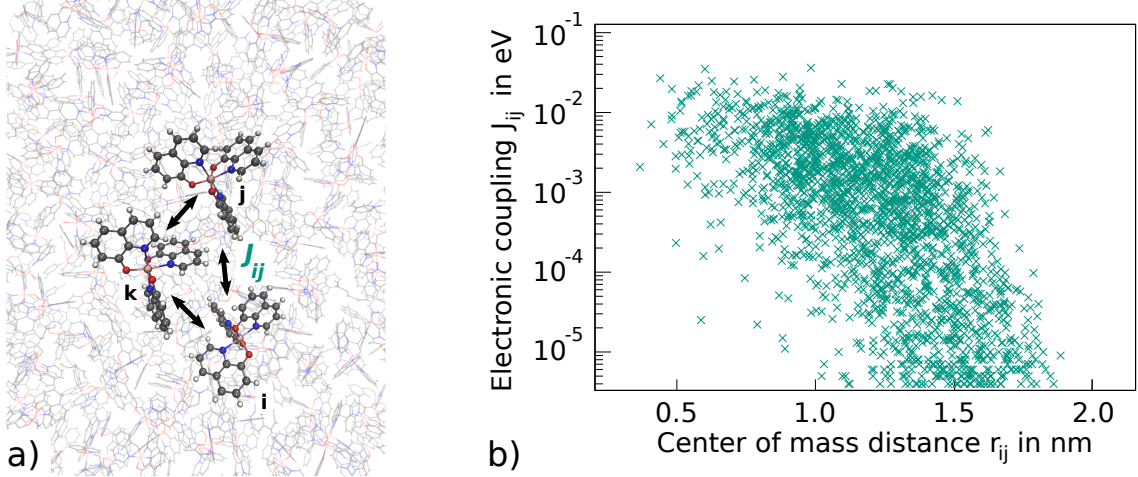
Figure 2.3.: Electronic coupling J_{ij} [63, 64] for each pair (i,j) on molecular level. a) Schematic figure of pair coupling between molecules i, j and k. b) Example distribution for the electronic coupling J_{ij} of highest occupied molecular orbitals (HOMO) in NNP dimer calculations in dependence of the center of mass distance r_{ij} of the molecules. The electronic coupling declines exponentially with the center of mass distance.

Electronic coupling calculations are done on dimers, *i.e.* DFT calculations of molecule pairs with fixed coordinates in vacuum. For the mobility calculation, the electronic coupling J_{ij} is averaged together with the distance $r_{ij} = |R_i - R_j|$ of the center of masses R_i and R_j of the molecules. This average adds up to the electronic coupling parameter $\langle J^2 r^2 \rangle$ when divided by the number of addends according to Equation 2.9. Only non-zero contributions of the coupling J_{ij}, *i.e.* J_{ij} within the accuracy of the code, are considered in the summation over the square of the product of J_{ij} and the center-of-mass distance r_{ij}.

$$\langle J^2 r^2 \rangle = \frac{\sum (J_{ij} r_{ij})^2}{N} \Big|_{J_{ij} \neq 0} \tag{2.9}$$

Far hops and strong coupling enhance the mobility. The average electronic coupling J_{ij} falls exponentially with the center-of-mass distance r_{ij} of the molecule pairs consistent

with quantum tunneling. An example is given in Figure 2.3 b) showing the dependence of the coupling J_{ij} on the center-of-mass distance r_{ij} at the example of the highest occupied molecular orbital (HOMO) of material NNP[1]. The coupling decreases with increasing center-of-mass distance r_{ij}. This exponentially drop with the distance limits the impact of far hops.

Energy disorder   In the analytical formula 2.5 the energy disorder σ enters the exponent in square, indicating that the charge carrier mobility μ is highly sensible of it. A profound calculation of the effective energy disorder is therefore of high importance. It is calculated from the electronic orbital energies E_i. In case of holes transport the studied orbital is the highest occupied molecular orbital (HOMO) and in case of electron transport the lowest unoccupied molecular orbital (LUMO).

The energy disorder can be described as global property σ_{global} or local one σ_{local}. The global energy disorder $\sigma_{global} = \sigma_{global}(E_i)$, shown in Equation 2.11, with

$$E_{mean} = \sum_{i=1}^{N} E_i/N, \tag{2.10}$$

is based on the orbital energy distribution of single molecules. The local energy disorder $\sigma_{local} = \sigma_{local}(\Delta E_{ij})$, according to Equation 2.12, accounts for the energy difference $\Delta E_{ij} = E_i - E_j$ of neighboring molecule pairs. Since the hopping charge transport is a local process, this work uses the local energy disorder for the mobility estimation. The distributions of the HOMO energy E_i and HOMO energy difference ΔE_{ij} of neighboring molecule pairs for the example of DEPB are depicted in Figure 2.4 a) and b), respectively. According to the hopping model, the distributions E_i and $\Delta(E_{ij})$ are expected to be Gaussian. The agreement with the fitted Gaussian, added in black, can clearly be seen for $\Delta(E_{ij})$.

$$\sigma_{global} = \sigma(E_i) = \sqrt{\frac{\sum_{mols}(E_i - E_{mean})^2}{N_{mols} - 1}} \tag{2.11}$$

$$\sigma_{local} = \frac{1}{\sqrt{2}}\sigma(\Delta E_{ij}) = \frac{1}{\sqrt{2}}\sqrt{\frac{\sum_{pairs}(E_i - E_j)^2}{N_{pairs} - 1}} \tag{2.12}$$

The reliable calculation of molecular orbital energies E_i is done with DFT methods. A first approximation for these energies can be obtained by calculations with fixed coordinates in

---

[1] N1,N4-di(naphthalene-1-yl)-N1,N4-diphenylbenzene-1,4-diamine
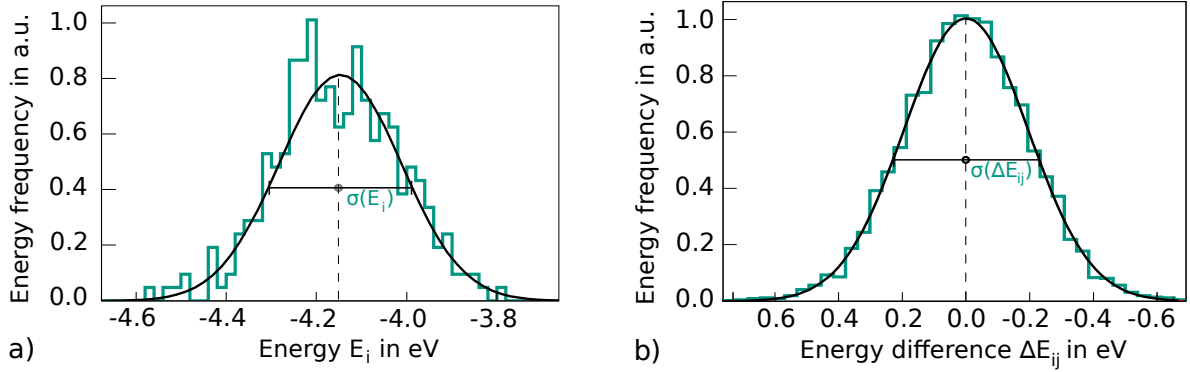
Figure 2.4.: Energy disorder in the highest occupied molecular orbitals (HOMO) in DEPB morphology. In black, a Gaussian is added, fit to the histogram values. The standard deviation of the distributions gives the value for the energy disorder within the material. a) Distribution of the HOMO energies E_i calculated by DFT methods on molecular level. The global energy disorder $\sigma(E_i)$ complies with formula 2.11. b) Distribution of the pair energy difference ΔE_{ij} between neighboring molecules calculated by DFT methods on molecular level. The effective local energy disorder $\sigma_{eff} = \sigma_{local}$ is obtained by formula 2.12 using $\sigma(\Delta E_{ij})$.

vacuum for each molecule in the system. But this approach neglects all the surrounding molecules, especially their long range electrostatic interactions. A better approach is to calculate the molecules in matrix, where all surrounding molecules are represented by either their dipole or point charges on each atom, *i.e.* electrostatic potential charges (ESP) explained in section 3.1.2. The environment will influence the electron orbitals and the energies of the quantum mechanically treated molecule, which in turn interacts electrostatically with its environment. Thus, to obtain an accurate energy landscape, a self-consistent loop for the dipole or ESP feedback calculation is required.

The energy disorder σ in crystals is expected to be near zero since a crystal structure accounts for highly periodic systems. However, there can be differences within the crystal unit cell. The main contribution to the energy disorder in crystals arises from the difference in the molecule's orbitals of the molecules within the unit cell. The amorphous structures are expected to have a larger energy disorder caused by the various unique molecular geometries present in the samples.

2.3. Important interface properties and phenomena

Towards the simulation of organic devices such as organic light emitting diodes (OLEDs), the simulation of bulk properties, *e.g.* the charge carrier mobility is one important step. Another crucial aspect is the examination of the processes taking place at the interfaces.

Joining distinct materials causes an abrupt change in the electrostatic potential for molecules near the interface. A direct consequence of interfacing distinct materials is the shift in the work function [65, 66]. The molecules adjust to the new environment and this transition can lead, for example, to an interfacial dipole layer or charge transfer [66]. Furthermore, in organic photovoltaics, the dissociation of exitons is a major process taking place at the organic heterojunctions between electron donor and electron acceptor materials [20, 67–69]. Also, the creation of geminate pairs at interfaces has been studied [70]. Although these phenomena are subject to theoretical studies [20, 68, 70–75], only few studies included the impact of realistic morphologies so far. Experimentally, an impact of the disorder on the processes at the organic-organic interfaces has been reported, *e.g.* by Zimmerman *et al.* [74]. They found a dependence of the polaron-pair recombination on the interfacial disorder at C_{60} heterojunctions.

While the simulation of pure (bulk) materials requires rather small samples and is treated with periodic boundaries, the simulation of organic interfaces demands larger simulation boxes accounting for the distinct molecular length scales and reducing edge effects. For example, interfaces can be periodically expanded in two dimensions along the interface plane, but not readily perpendicular to it. Also, especially for crystalline materials, the distinct periodicities can prevent a common periodic box within a reasonable system size. In Chapter 5, a theoretical study of the induced disorder at the interface of two organic crystals is presented.

2.4. Single-walled carbon nanotubes

Carbon nanotubes (CNT) were first introduced by Iijima of the NEC corporation in 1991. In 'Helical microtubules of graphitic carbon' [76] he announced the synthesis of needle-like coaxial tubes of graphene sheets as illustrated in Figure 2.5. Two years later he was able to produce single-walled carbon nanotubes (SWCNT) [77] for which fantastic properties were predicted [78], such as distinct electronic conduction and high mechanical strength

and stability.
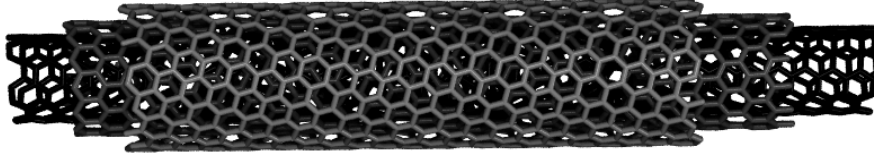
Figure 2.5.: Model of nested carbon nanotubes.

Single walled carbon nanotubes can be thought of being wrapped graphene sheets. The nanotubes can be characterized by two indices (n, m) according to Hamadas notation [78] defining the path it takes to circle the tube's circumference. A general figure is shown in Figure 2.6 a) and specifically for nanotube (8,4) in Figure 2.6 d).

n and m are the numbers of hexagons passed to reach the point (n,m) which joins back in (0,0) to form the tube. The structures for (n,n) are called *armchair* and (n,0) *zigzag* structures referring to the arrangement of hexagons along the circumference.

The SWCNTs differ in diameter and angular pattern, *i.e.* the chiral angle θ. The angle can range from $\theta = 0°$ in zigzag structured nanotubes, such as (10,0) in Figure 2.6 b), to $\theta = 30°$ in armchair-like circumference tubes like (6,6) shown in Figure 2.6 c). These two SWCNT groups (n,0) and (n,n) are symmetrical nanotubes. Other combinations of n and m correspond to asymmetric geometries like (8,4) depicted in Figure 2.6 d) and e). These non-symmetric tubes have a so-called handedness to the left or right, *i.e.* the hexagons follow a clockwise or counter-clockwise pattern.

Each SWCNT type (n, m) possesses unique intrinsic properties such as diameter, chiral angle and electronic conductance [23]. Thereby, the electronic structure is defined mostly by the hexagonal pattern and not by the length. While all SWCNTs with $n = m$ are metallic and $(n - m)/3 \in \mathbb{N}$ exhibit a low bandgap [79], the rest of the tubes is semiconducting with falling bandgap as the diameter rises [80, 81].

Single-walled carbon nanotubes are studied in different areas of research from medicine to electronics [16]. Several compounds found in electronic devices such as field-effect transistors (FET) [82] or thin-film transistors (TFT) [83], were fabricated using SWCNTs. These applications take advantage of the semiconducting nature of SWCNTs. Shulaker *et al.* published a paper on a carbon nanotube computer [82]. In spite of developing methods for further shrinking of electronic devices his group at Stanford University was able to build a computer fabricated using SWCNTs based transistors. Their nanotubes
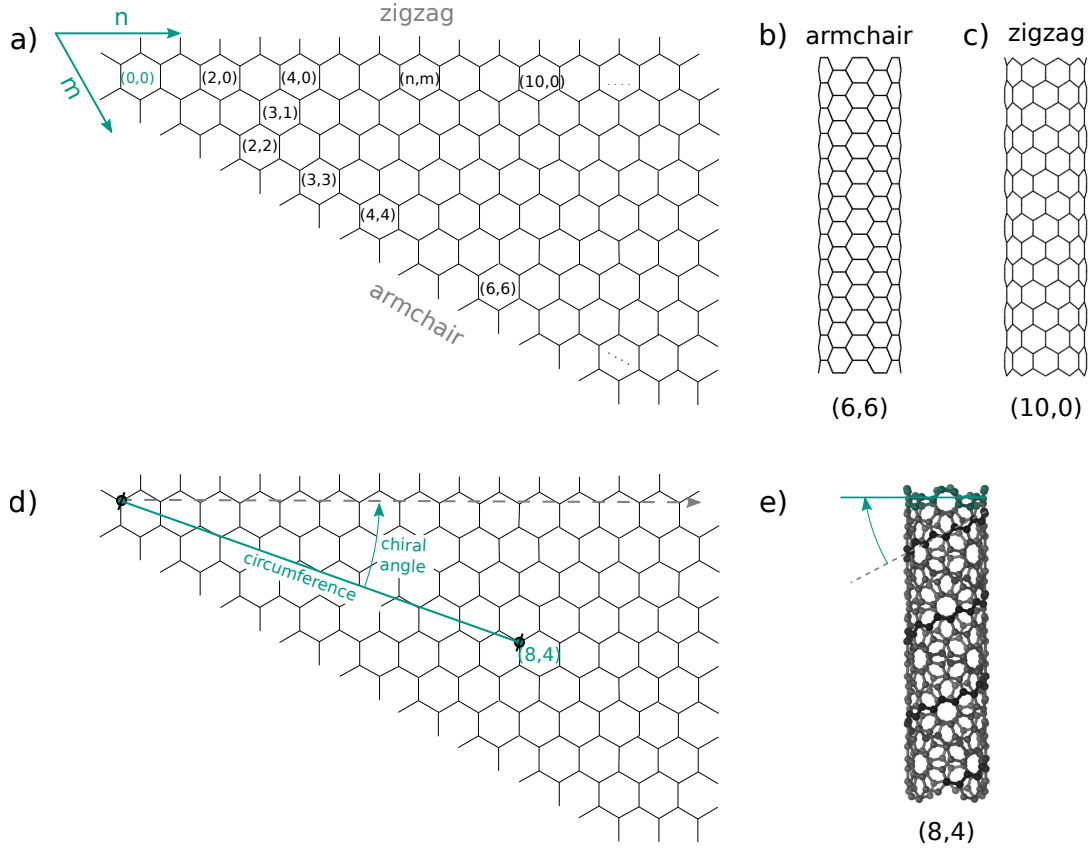
Figure 2.6.: a) (n,m) indices defining single-walled carbon nanotubes on graphite lattice. b) Example of armchair nanotube $(n, n) = (6, 6)$. c) Example of zigzag nanotube $(n, 0) = (10, 0)$. d) Illustrated circumference path on graphene sheet for (8,4) nanotube. e) Figure of (8,4) nanotube with a diameter of 0.829 nm and a pitch angle of $\theta = 19.1°$

were prepared on a special designed plate prohibiting metallic SWCNTs. Working in a biological environment a different characteristic is of importance. Kam *et al.* used SWCNTs as a biological transporter in cancer cell destruction [84]. The method profits from the optical absorptive nature of the SWCNTs and the lack of toxicity of SWCNTs in the human body.

For all these applications the corresponding SWCNTs are required to have properties fitting the applications' needs. Unfortunately, the SWCNT production methods create a composition of several SWCNT types with a variation in diameter and chiral angle. In current selection experiments, wide range SWCNT mixtures are used, *e.g.* produced by high pressure CO disproportionation of Fe(CO)$_5$ (HiPco) [24, 85–88] or by Co/Mo catalysts (Co-Mo-CAT) [25, 89].

2. General theoretical framework

The SWCNTs in mixtures typically are detected by analyzing the bandgap fluorescence [90] while dispensed in aqueous solution. Good dispersion with weak selectivity can be achieved, for example, by using an aqueous solution with sodium cholate in D_2O. The detection requires a scan over a range of excitation wavelengths and the measurement of the corresponding emission wavelengths. Figure 2.7 shows the intensity of the emission wavelengths in dependence of the excitation wavelengths[2].
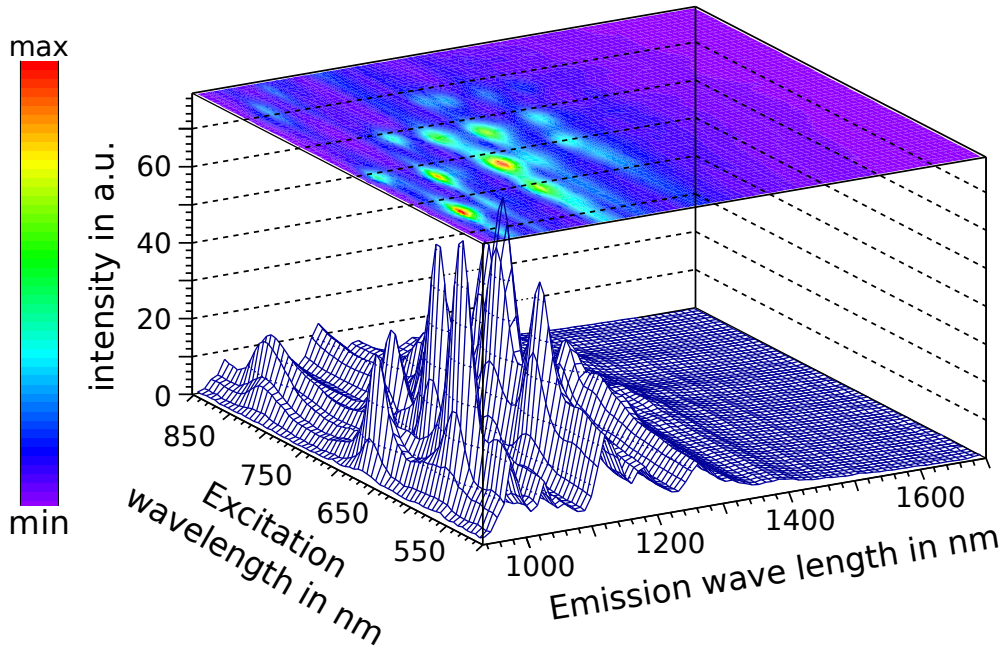
Figure 2.7.: Photoluminescence measurement data for detection of SWCNTs dispersed in aqueous solution with weakly selective sodium cholate in D_2O. The intensity of the emission wavelengths is shown in dependence of the excitation wavelength. The color reflects the intensity where each peak corresponds to one specific SWCNT type.

Photoluminescence spectroscopy can only detect semiconducting SWNTs. The measurements are done to determine the amount of the distinct semiconducting SWCNT types in a mixture. Each peak corresponds to one specific tube as described by Bachilo *et al.* [91]. The intensity can be used to estimate the amount of this SWCNT type in the mixture.

[2]The photoluminescence data were obtained by Nicolas Bertron and Fabien Lamasson from the research group of Marcel Mayor.

20

The higher the emission intensity, the higher the amount of corresponding SCWNT type.

Spectroscopy of HiPco-based mixtures detects SWCNTs of different angular pattern with diameters ranging between 0.7 nm and 1.4 nm [24, 85, 92]. Also, the distribution of SWCNTs is not equally spread and varies from tube to tube. Thus, for the employment in electronic devices, the SWCNT mixtures have to be sorted to filter the tubes with the required unique properties.

In search of efficient sorting procedures of the SWCNTs physics and chemistries have been explored [26]. By centrifugation, *e.g.* the heterogeneous mixtures can be sorted by mass. Unfortunately, the weight of the SWNTs is not discriminating in diameter or electronic properties owing to the varying length of SWCNTs produced. By using density-gradient ultracentrifugation, however, sorting by diameter, bandgap and electronic type was reported [93, 94]. For purifying the heterogeneous mixture in terms of semiconductance, Zhang *et al.* used a destructive method by gas-phase reaction [27]. Also, sorting procedures using deoxyribonucleic acid (DNA) [95–99] have been studied intensely. The particular strength of using DNA is the attainable precise modeling of a unique arrangement which can pick specific tubes over other ones. This DNA origami [28] is powerful but extremely complex as it involves a huge number of unique 'staple strands' and thus expensive. Qian *et al.* on the other hand, exploited structural symmetries to assembly defined geometries with only a few distinct DNA strands. Furthermore, many highly selective polymers were reported [30–34, 38, 44, 45, 100–110]. Polymers are quite cheap in production and qualify for mass-processing. Unfortunately, the theoretical background of polymer wrapping around single-walled carbon nanotubes is not fully understood yet.
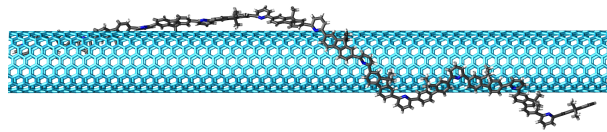
Figure 2.8.: Schematic of a wrapping conjugated polymer on a single-walled carbon nanotube.

Several theoretical investigations on distinct, mostly conjugated, polymers for sorting SWCNTs have been reported [29–38, 44, 45]. The simulations applied, lean on Molecular Dynamics methods. Owing to the nature of polymers, the simulated systems represent a many-body problem with a huge intrinsic phase space leading to slow convergence, if

at all, and often poorly covered. Therefore, often, only one or few SWCNTs were taken into account in the studies [29, 31, 32, 35, 36, 38]. At the end of a long simulation run in equilibrium, typically one conformation is found (or not). A common aspect in studies on polymer wrapping is the flat orientation of the conjugated orbitals in the backbone of the polymer on the SWCNT surface as shown in Figure 2.8. This leads to an overlap of the π-electron systems of polymer and SWCNT. For a deeper insight into the underlying mechanism, restricting the phase space of the problem seems to be a good approach.

2.5. Implementation of a coarse-grained polymer wrapping model

One of the questions addressed in this work is the prediction of polymer wrapping around single-walled carbon nanotubes. As mentioned in the last section, the process takes place in a mixture of polymers and nanotubes in a solvent on longer time-scales, *i.e.* longer than a few nano seconds (ns). MD simulations of polymers and SWCNT in solvent are highly resource and time intensive. They converge extremely slowly and only small parts of the phase space are covered [33]. Therefore, in this work, a different approach was used.

Here, a coarse-grained polymer wrapping model (CG-PWM) is investigated. CG-PWM is built on the assumption of the existence of a limited number of conformations of polymers wrapping around SWCNTs in the configuration space.

The polymer wrapped SWCNTs can be described by the grand canonical partition function Z summing over all conformations:

$$Z = \sum_i e^{\frac{N_i \mu - E_i}{k_B T}} \tag{2.13}$$

with the occupation number N_i of the conformation i, the total energy E_i, the chemical potential μ, the temperature T and the Boltzmann constant k_B. The probability p_i to find a wrapped conformation i of specific SWCNT and polymer is given by equation:

$$p_i = \frac{1}{Z} e^{\frac{N_i \mu - E_i}{k_B T}} \tag{2.14}$$

Within these conformations, low-energy formations are expected to be preferably formed. For a discrimination of SWCNT types - identified by (n,m) - one has to add all contributions of various lengths of conformations of (n,m)-SWCNTs together.

The binding free energy cannot be calculated straightforward. Wang *et al* [111] used free energy perturbation molecular dynamics with restraining potentials to gain the binding energy. But the formation of wrapped conformations reduces the configuration space of the polymers and therefore affects the entropy. Calculating the binding free energy therefore is insufficient. Following the work of O'Connell *et al* [108] and Kato *et al* [112, 113], who analyzed the thermodynamics of the reversible solubilization of single-walled carbon nanotubes with the help of DNA or polymers, the upper bound of change in entropic cost can be approximated by

$$\Delta S = -k_B \ln\left(3^{n-2}\right) = -k_B \left(n - 2\right) \ln\left(3\right) \tag{2.15}$$

where n is the number of free dihedrals in the polymer backbone. This entropic cost is polymer specific. For the polymers studied in this thesis this cost lies around 0.4 eV to 1.1 eV.

The first goal in developing CG-PMW was the mathematical construction of all conformations relevant to the selectivity process. This was achieved by identifying a common pattern in reported conformations found by Molecular Dynamics studies of polymer wrapping [29–33, 36, 38, 100, 108]. These studies report wrapping conformations with conjugated moiety forming electron orbital overlaps with the SWCNT surface indicating a major role of π-π stacking between the polymers and the SWCNT in the wrapping process.

Maximizing the areal overlap between conjugated electron systems and the SWCNT surface is achieved when the polymer moiety lies flat on the effective diameter reflecting the van-der-Waals distance. This positional restriction is formulated in two equations. For convenience, without loss of generality, the SWCNT's axis is aligned along the z-axis and positioned through the origin (0,0,0). Equation 2.16 demands the center $\vec{c} = (x, y, z)^{-1}$ of the conjugated moiety having a distance from the SCWNT axis of half the effective diameter D_{eff} with $D_{eff} = D_{\text{SWCNT}} + 2 \cdot d_{\text{vdW}}$ defined as the sum of the SWCNT diameter D_{SWCNT} and the effective van-der-Waals distance d_{vdW} between the polymer and the SWCNT [114].

$$x^2 + y^2 \quad = \quad (D_{eff}/2)^2 \tag{2.16}$$

The second requirement is addressed by Equation 2.17 expressing the alignment of the conjugated molecule plane with the SWCNT surface. Exploiting the SWCNT axis alignment along the z-axis, this can be formulated using the center position $\vec{c}$ and the normal

$\vec{n} = (a, b, c)^{-1}$ of the conjugated plane.

$$|y \cdot b + z \cdot c| \quad = \quad \max \tag{2.17}$$

Additionally, all atoms of the polymer cannot penetrate the effective SWCNT diameter.

Next, the degrees of freedom need to be reduced while conserving the underlying wrapping mechanism. This is done via extensive approximations which, in the end, have to be validated to represent the wrapping process.

2.5.1. Model approximations

A first approximation is done by neglecting the solvent. The solvent allows the dispersed polymers to unfold and be attracted by SWCNTs.

SWCNT representation as cylinder   Many polymers are found to show a diameter dependent selectivity. If chirality plays a minor role in the wrapping process, the SWCNT can be reduced to the geometrical form approximated by a cylinder with corresponding effective diameter D_{eff}. Additionally, as the SWCNT is a rigid molecule, a constant
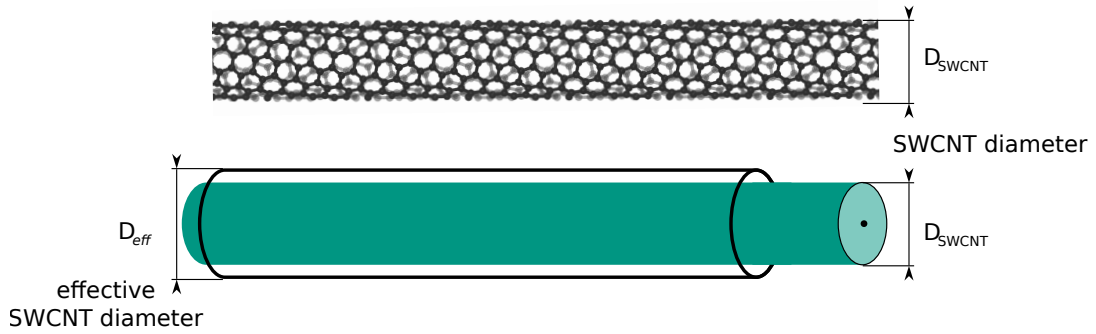
Figure 2.9.: Replacement of SWCNT by cylinder with effective tube diameter.

energy contribution of the SWCNT E_{NT} is expected, *i.e.* $E_{\mathrm{NT}} = const.$

Constant contact interaction of polymer and SWCNT   Furthermore, the lack of dependence on the chiral angle reported [32] suggests that the interaction potential between the SWCNT and the polymer does not depend on the orientation of the conjugated polymer on the surface. The energy contribution to the total system energy, therefore, is expected to be constant for each polymer chain link. For distinct polymers which are of

the same length the interaction energy between polymer and SWCNT is approximated with a constant, $E_{\text{pNT}} = const$.

Omitting of polymer alkyl chains   Several MD studies [30, 31] suggest that the major function of alkyl chains is related to the solubility. For the wrapping process itself, the side chains are likely to play a minor role. The MD studies report side chains on the SWCNT but also pointing into the solvent. Therefore, the side chains are discarded.

Rigid body geometry   Additionally, most reported conjugated systems are known to form stable conformations [115]. Thus, disregarding the vibration modes and fixing the relative coordinates, the moieties are replaced by rigid objects. Still, for the wrapping process the backbone has to be flexible and the two positional restrictions require two degrees of freedom to be matched with. In Figure 2.10 three steps for replacing the polymer by building blocks are presented.

First, the molecular geometry, *i.e.* all bonds and angles, are fixed (Figure 2.10 a)). Then, the rotation axes a and b are identified. They are connected in fixed angles γ and δ. The hinges mark the origins of the dihedral rotations (see Figure 2.10 b)). Finally, as two rotational degrees of freedom are required, two moieties are joint in one building block as depicted in Figure 2.10 c). To provide maximized electron orbital overlap, the hinge in the larger conjugated system is taken as central point $\vec{c}$ for the positioning.

In summary, in the geometrical coarse-grained model, polymers are treated as rigid building blocks. Each building block carries two intrinsic degrees of freedom allowing it to flex the polymer's backbone while adjusting to the SWCNT surface. Since the relative positional information is conserved, the conformations can be transferred straightforward to an all-atom representation, *e.g.* for further refinement.

2.5.2. Energy consideration

In this thesis the system is analyzed for its energy contributions and the decisive contribution is identified. Neglecting the solvent, the total interaction energy E_{tot} between one polymer and one SWCNT for a start can be summarized by Equation 2.18.

$$E_{tot} = E_p + E_{\text{pNT}} + E_{\text{NT}} \tag{2.18}$$
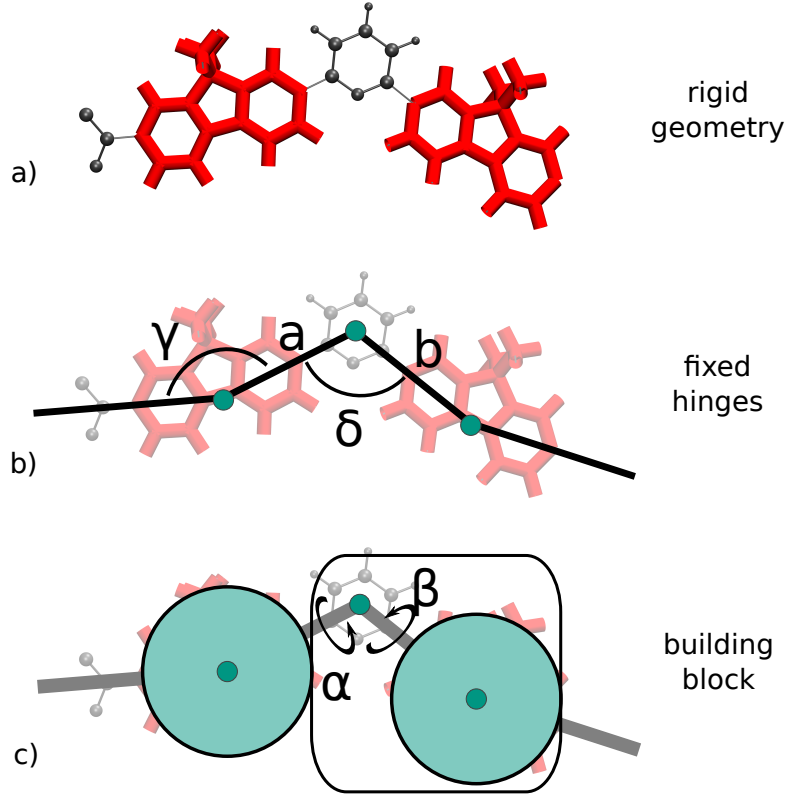
Figure 2.10.: Steps towards representation of polymer by building blocks at the example of a conjugated polymer with two moieties. a) Rigid body model: Fixed optimized geometry. b) Hinges and sticks along the polymer backbone. Note: the angles γ and δ are fixed and the sticks a and b form the axes of rotation. c) Building block for polymer representation in the model. The two angles α and β are the only degrees of freedom at this point.

In here, E_p is the inner polymer energy, E_{NT} the inner SWCNT energy and E_{pNT} represents the interaction energy between the polymer and the SWCNT.

The energies E_{NT} and E_{pNT} are assumed to be constant for each wrapped polymer/SWCNT pair as mentioned above. Furthermore, the representation of polymer chain links by building blocks leads to a separation of the inner polymer energy into two parts given in Equation 2.19.

$$E_p = E_{pd} + E_{pr} \tag{2.19}$$

with E_{pd} representing the energy contribution from the free dihedrals and E_{pr} being the rest of the polymer inner energy.

After fixing all but two dihedrals within each building block, E_{pr} is constant. Equation 2.18 can be written as

$$E_{tot} = E_{\mathrm{pd}} + E_{\mathrm{pr}} + E_{\mathrm{pNT}} + E_{\mathrm{NT}} \approx E_{\mathrm{pd}} + const \tag{2.20}$$

The only discriminating energy left in the wrapping process is the energy correlated with the bending of the polymer from its relaxed geometry. This energy can be calculated from the energy potential of the dihedral rotation.

Each building block contributes two energies to E_{pd} corresponding to the dihedral angles. Therefore, each conformation can be assigned an intrinsic total energy.

As noted before, the model postulates the low-energy conformations to be a key criterion. All mathematically constructed conformations therefore have to be weighted by their total energy. This can be done, for example, by using a Boltzmann-like weighting factor w shown in Equation 2.21.

$$w = e^{-kE_{\mathrm{pd}}} \tag{2.21}$$

Neglecting constant energetic contributions including the entropic cost introduced in Equation 2.15 leads to an unknown energetic threshold dividing stable from unstable conformations. This results in an unknown plain energy cutoff for low-energy conformations. Using the Boltzmann-weighted energies, the influence of this threshold can be eased.

2.5.3. Model implementation

To address polymers with CG-PWM, first molecular structure data have to be obtained. This can be done, for example, by using DFT. On the optimized structures, the hinges and axes are identified and taken as input data for the model. Furthermore, the dihedral energy potential surfaces for each rotatable dihedral has to be calculated beforehand. This potential surface is taken as lookup table for the two energy contributions of each successfully placed building block.

The model was implemented using a recursive approach. The building blocks are placed one by one until the requirements cannot be matched or the maximal number of building blocks was reached.

The first dihedral rotation is used to match Equation 2.16 while the second rotates the conjugated moiety to lie flat on the nanotube surface, *i.e.* checking Equation 2.17. In doing so, a maximal number of four distinct arrangements for each building block is accessible corresponding to the rotations to the left and right. For a polymer with ten building blocks, this leads to the maximal number of $4^{10} \approx 10^6 = 1.000.000$ theoretical conformations for each turn. Also, the relative orientation of the first building block in respect to the SWCNT's axis is varied to cover the configuration space. Applied for each effective SWCNT diameter, all possible conformations of polymers on SWCNTs can be constructed.

2.5.4. Summary

A coarse-grained model simulating polymer wrapping around single-walled carbon nanotubes has been developed and implemented. The model is based on the identification of common patterns reported in MD studies on polymer wrapping. The model reduces the complexity of the problem to only a few parameter, *i.e.* the optimized molecular structure, two rotational degrees of freedom in backbone dihedrals and their energy profile. An efficient implementation was achieved by using an recursive approach.

Using a coarse-grained model instead of all-atom MD shows one important advantage: Owing to the long simulation time requirements in MD only limited number of conformations of wrapping polymers can be obtained which gives only a qualitative insight to the problem. The new developed coarse-grained model opens up the ability for quantitative estimates of wrapping affinity for polymers on different nanotubes.

3. Computational modeling methods

The specific simulations presented in this thesis, being multiscale in their nature, require detailed information coming from a number of different time/length scales. The numerical methods treating these scales in an accurate fashion have been developed within the last few decades. In this chapter a short description of the basic concepts behind each of the used methods is presented.

For example, while the intrinsic molecular properties such as reorganization energy, are addressed by the quantum mechanics based density functional theory, the morphology generation is done by classical Molecular Dynamics, as feasibility vs. accuracy is of importance.

Section 3.1 gives an introduction to the density functional theory (DFT) followed by the MNDO method (modified neglect of diatomic overlap), while classical all-atom Molecular Dynamics (MD) is presented last.

3.1. Quantum mechanical framework: Density functional theory

Density functional theory (DFT) is a quantum mechanical method to determine the ground state electron density of many electron systems in an electrostatic potential, *e.g.* in molecules. Electron-electron interactions are handled in a mean field level allowing for big systems opposed to correlated theories, *i.e.* systems with several hundred atoms.

3.1.1. From Schrödinger's equation to density functional theory

Starting from the Schrödinger Equation 2.1, several approximations are required towards DFT, starting with the *Born-Oppenheimer Approximation* [116]. The Born-Oppenheimer

approximation uses the large difference in electron and nucleon masses. Electrons react quasi instantaneously to a change of nuclei potentials, allowing to decouple electron and ionic wave functions. DFT then solves the electronic part of the many-body Hamiltonian:

$$\left[-\frac{\hbar^2}{2m} \sum_{i=1}^{N} \nabla_i^2 + \sum_{i=1}^{N} v(\vec{r_i}) + \sum_{i=1}^{N} \sum_{j>i}^{N} U(\vec{r_i}, \vec{r_j}) \right] \Psi = E\Psi \tag{3.1}$$

where the first term represents the kinetic energy of the electrons, with $\hbar$ as the Planck's constant h divided by 2π, the electron mass m, the number of electrons in the system N and the nabla operator ∇. The second term describes the interaction of the electrons on positions $\vec{r_i}$ with the field v generated by the nuclei. The last term represents the interaction between the single electrons.

Hohenberg and Kohn "proved that there exists a universal functional of the [electron] density, $F[n(\vec{r})]$, independent of $v(\vec{r})$, such that the expression

$$E \equiv \int v(\vec{r})n(\vec{r})d\vec{r} + F[n(\vec{r})] \tag{3.2}$$

has as its minimum value the correct ground-state energy associated with $v(\vec{r})$." [117] With the electron density $n(\vec{r})$ defined in Equation 3.3 where the electron density is represented as a scalar product of one-electron wave-functions ψ, called Kohn-Sham orbitals.

$$n(\vec{r}) = 2 \sum_{i} \psi_i^*(\vec{r})\psi_i(\vec{r}) \tag{3.3}$$

Hohenberg and Kohn stated that knowing the exact functional $F[n(\vec{r})]$ will lead to an exact solution of the Schrödinger equation. In real life, the functional is not known and has to be approximated as well as a basis set for the Kohn-Sham orbitals has to be chosen.

3.1.2. Energies, orbitals and potentials from DFT calculations

Properties on molecular level, such as molecular bond lengths, can be calculated using DFT methods. The energy of the ground state as well as the orbitals are calculated by default since the theory bases on them. Other properties such as electrostatic potential or bond lengths and angles are further important data. The following pages give some examples on how molecular properties are obtained with DFT and why they are important for this work.

Ground-state energy calculations

The most relevant quantity calculated by DFT is the energy of the ground state. This energy typically is calculated starting with the determination of the electronic structure. The electronic structure or the charge density is calculated with fixed nuclear coordinates while the electron configuration with the minimal energy is determined. In geometry optimization, the nuclear coordinates are varied and the energy is calculated. With this procedure the smallest energy by electronic structure calculation is sought. When the search for minimum is converged, the optimized molecular geometry is found.

For molecules in realistic morphologies, *i.e.* non-relaxed molecules, the energy is calculated with fixed nuclei positions. This leads to unique energy levels for distinct molecules in the electrostatic environment. From these differences the energy disorder can be calculated which is an important parameter for charge transport.

Electron orbital localization

Another interesting point is the localization of electron orbitals. When the relaxed electronic structure is known, the densities pertinent to the single orbitals can be visualized. Especially the localizations of the highest occupied molecular orbital (HOMO) and the lowest unoccupied molecular orbital (LUMO) are often of interest, *e.g.* the overlap of HOMO and LUMO of neighboring molecules determines the probability of charge transfer through tunneling as described in Chapter 4.

Electrostatic potential and point charges

Point charges of real electron densities of a molecule are used to approximate the electrostatic potential produced by the molecule. In Molecular Dynamics, described in the following section 3.3, the point charges are used to determine the electrostatic force on each atom originating from the surrounding molecules.

The easiest way to calculate point charges is using Mulliken charges. Mulliken charges are obtained by projecting the electron orbital on the atom centered spherical harmonics. These charges were found to reproduce the electrostatic field of the molecules only poorly [118, 119].

3. Computational modeling methods

In 1984 Kollmann et al. [120, 121] suggested another method for calculating the point charges. Their approach is geared to reproduce the actual electrostatic potential. Electrostatic potential charges (ESP) are fitted charges. In contrast to Mulliken charges which are basis set dependent, ESP charges are directed to reproduce the electrostatic potential of the ground-state. For this purpose the electrostatic potential is calculated on several spheres around the atoms and the point charges are fitted to reproduce this potential. This method fulfills the requirements for the classical treatment of the electrostatic potential.

When calculated in vacuum, ESP charges tend to overestimate the electrostatic nearfield. A refined model of restricted ESP charges (RESP) [122] was published by Bayly *et al.* in 1993. Penalty functions are introduced to pull the atomic charges towards smaller values.

Calculation of the dihedral energy potential surface with fixed coordinates

Outside of quantum mechanics the potentials of changes in the molecular structure are often used to approximate energy costs of movements away from the optimal configuration. These potentials can be used in classical force fields, introduced in section 3.3.1. In this work, the potential for the proper dihedral in polymer backbones is used in a coarse-grained approach. With DFT a robust potential can be obtained. For this, the dihedral of the optimized structure is rotated and the ground-state energy with fixed coordinates is calculated in regular steps. From the obtained energies, the dihedral energy potential surface can be estimated, e.g by using B-splines or linear approximation in case of detailed data. In similar fashion other potentials can be obtained, *e.g.* for bond stretching and angle bending.

3.1.3. QM package Turbomole

The molecular properties on DFT level for this thesis were obtained by the *ab-initio* DFT code Turbomole [123] (Turbomole GmbH, Karlsruhe, Germany). With Turbomole two different functionals have been used. Functional BP86 using generalized gradient approximations (GGA) [124, 125] and the hybrid functional B3-LYP [124, 126]. Basis sets SV(P) [127] and TZVP [128] were used. If not stated otherwise, the calculations were done in the combination BP86 functional with SV(P) basis set.

3.2. Semi-empirical quantum chemistry method MNDO

The semi-empirical MNDO method (modified neglect of diatomic overlap) is based on the Hartree Fock approximation (HF) [129]. Hartree Fock assumes the all electron wave function of a many electron system to be the antisymmetrized product of uncorrelated single electron wave functions. Single electrons thereby interact with the charge density created by the other electrons.

The total energy E, for example, of a molecule is calculated in HF by Equation 3.4 where the first term holds the single electron energy and the electron-electron interactions are covered by the second term.

$$E = 2 \sum_i H_i + \sum_{i,j} \left(2 J_{ij} - K_{ij} \right) \tag{3.4}$$

MNDO now neglects non-local parts of the exchange integrals within K_{ij} [130]. Instead, the non-local coulomb integrals J_{ij} are then parametrized such that experimental quantities as heat of formation or dipole moments are reproduced by the equivalents derived in the model [131].

In this thesis, the semi-empirical quantum chemistry package MOPAC [132] (Molecular Orbital PACkage) (Stewart Computational Chemistry, Colorado Springs, CO, USA) was used. The charge calculations with MOPAC done in this work use the PM6 parametrization [133].

3.3. Classical all-atom mechanics framework: Molecular Dynamics

Molecular Dynamics (MD) is an atomistic approach to simulate materials. Electrons are replaced by effective potentials and point charges to reflect the electrostatic interaction between the atoms. While QM methods base on the Schrödinger Equation, MD bases on classical mechanics, especially on Newton's second law (see Equation 2.2). With classical potentials the system is simulated as a multi-particle ensemble. Neglecting quantum mechanical effects despite the quantum mechanical nature of the particles, MD approximates the interactions between the particles by effective potentials, so called 'force fields'.

The following section 3.3.1 focuses on the details of MD force fields used in this work.

3. Computational modeling methods

Details on the simulation steps can be found in section 3.3.2. And finally, the software packages used are introduced and typical simulation cases are discussed in section 3.3.3.

3.3.1. Force Fields for Molecular Dynamics

The force field is a complex accumulation of different effective interaction potentials corresponding to the different interaction types. A typical representation is shown in Equation 3.5.

$$V_{\text{FF}} = V_{\text{bond}} + V_{\text{angle}} + V_{\text{dihedral}} + V_{\text{LJ}} + V_{\text{Coulomb}} \tag{3.5}$$

The potential V_{Coulomb} for the Coulomb interaction is well defined (see Equation 3.6) and V_{LJ} for the Lennard-Jones interaction has widely used standard notations (see Equation 3.7).

$$V_{\text{Coulomb}} = \frac{1}{4\pi\varepsilon_0\varepsilon_r} \sum_{i<j} \frac{q_i q_j}{r_{ij}} \quad \text{with} \quad r_{ij} = |\vec{r_i} - \vec{r_j}| \tag{3.6}$$

$$V_{\text{LJ}} = \sum_{i<j} \left[\left(\frac{\sigma_{ij}}{r_{ij}}\right)^n - 2\left(\frac{\sigma_{ij}}{r_{ij}}\right)^m \right] \quad \text{with} \quad n > m \tag{3.7}$$

In contrast, other interactions are normally approximated by harmonic potentials in case of the potentials V_{bonds} for bond stretching between two atoms and V_{angle} for the angle bending. Furthermore, the (proper) dihedrals are represented with a more complex equation taking the multiplicity, *i.e.* periodic behavior within the rotation of 2π, into account.

Each potential consists of many parameters describing the interaction between atom groups of different atomic types. The parameters are fitted to achieve a good overall agreement with experimental data such as density or glass transition temperature. For different purposes distinct force fields can be used. Most of the force fields, such as AMBER [134], OPLS-AA [135] and CHARMM [136], have their origin in the field of proteins simulation and nucleic acids simulations such as protein folding or docking simulations. In special cases, force fields specific to each material are prepared [137].

In this work, the Generalized Amber Force Field (GAFF) is used [138, 139]. GAFF was designed as a general force field for (small) organic molecules. The separate potential contributions building the force field are listed in equations 3.6 and 3.8 to 3.11. These equations give a good impression of the amount of parameters needed to represent realistic

dynamics. A and B parametrize the Lennard-Jones potential. Parameters r_{eq} and θ_{eq} are the equilibrium bond lengths and angles, respectively. K_r, K_θ and V_n are force constants. The dihedral potential needs the multiplicity n and the torsion angle γ. Each group of atom types requires a separate set of these parameters.

$$V_{\text{LJ}} = \sum_{i<j} \left[\frac{A_{ij}}{r_{ij}^{12}} - \frac{B_{ij}}{r_{ij}^{6}} \right] \tag{3.8}$$

$$V_{\text{bond}} = \sum_{bonds} K_r (r - r_{eq})^2 \tag{3.9}$$

$$V_{\text{angle}} = \sum_{angles} K_\theta (\theta - \theta_{eq})^2 \tag{3.10}$$

$$V_{\text{dihedral}} = \sum_{dihedrals} \frac{V_n}{2} \left[1 + \cos(n\phi - \gamma) \right] \tag{3.11}$$

The different chemical structures in organic molecules lead to various atom types, which means, that not only the element is important for the force constant, but also their surrounding. For carbon, there are five different atom types implemented, depending on the chemical bonding. This leads, for example, to slightly different bond distances between simple single bonded carbon atoms, carbon in an aromatic ring, double bonded and triple bonded C-C connections. GAFF includes parameters for elements C, N, O, H, S, P, F, Cl, Br, and I for most of their chemical combinations. That means, that for most organic molecules GAFF can be used without making adaptions.

3.3.2. Molecular Dynamics simulations

MD simulations are carried out in short simulation time steps where each atom is moved according to the acting forces. After each time step the forces are updated to the new particle positions. The maximal time step is limited by the fastest movement on atomic level to avoid artifacts and molecular and atomic clashes. Typically the frequency of hydrogen movements sets the limit to about 2 femto seconds (fs) for room temperature. Longer time steps can lead to extreme forces causing high velocities and simulation instabilities. The observables, such as kinetic and potential energy, density, radial distribution function, pressure and disorder, are determined by averaging system snapshots over a sufficiently long simulation time period of an equilibrated system.

3. Computational modeling methods

3.3.2.1. Simulation modes

Structure optimization mode by energy minimization   To avoid extreme forces at the beginning of a simulation where the atoms can be far from optimal positioning, all MD packages offer an energy minimization mode. With a "steepest descent" algorithm the system is moved along the potential energy gradients into an energy minimum. This model typically leads to a local minimum which often is sufficient for a successful simulation start.

Structure relaxation process   Before reliable results can be produced in MD simulations the simulated molecular system has to reach an equilibrium state. The time until an equilibrium state is reached is called relaxation phase. To fasten the relaxation process a higher temperature than the temperature used in the main simulation can be used to enable the system to overcome higher energy barriers more easily. A good indicator for equilibrium is the system energy. Typically, the total energy is rapidly changing at the beginning of a simulation and over time stabilized within a certain energy range.

Simulation in equilibrium for determination of observables   When the equilibrium phase is reached, the simulation reproduces realistic molecular behavior. The observables, such as kinetic and potential energy, density, pressure and disorder, are then determined by averaging system snapshots over a sufficiently long simulation time period of an equilibrated system.

3.3.2.2. Thermostats for temperature control

In MD simulations, the temperature T is an important parameter and the temperature control a major challenge. The starting temperature or the distribution of velocities of the atoms is not expected to correlate with the simulation temperature. At start, the simulated system has to be heated or cooled down to match the desired temperature. Afterwards the simulation temperature has to be kept (roughly) constant.

Several thermostats were developed to achieve a constant or correct average temperature. The temperature is regulated by the distribution of the total kinetic energy E_{kin}. The relation between kinetic energy and the temperature T is given in Equation 3.12 and 3.13 where k_B represents the Boltzmann constant, N the number of particles and v_i the velocity

of each particle.

$$E_{kin} \;\; = \;\; \sum_{i=1}^{N} \frac{1}{2} m_i v_i^2 \tag{3.12}$$

$$T \;\; = \;\; \frac{2}{3Nk_B} E_{kin} = \frac{2}{3Nk_B} \sum_{i=1}^{N} \frac{1}{2} m_i v_i^2 \tag{3.13}$$

In this work the Nose-Hoover thermostat [140–142] and Berendsen thermostat [143] where used.

3.3.2.3. Periodic boundary conditions

At the edge of a materials cluster, non-realistic behavior can occur. Especially when one is interested in the bulk structure it is advised to simulate with periodic boundary conditions (pbc). Also the simulation in explicit solvent requires pbc to ensure an overall coverage of the solved system. With this condition the system is duplicated around the original system in such a way, that the left edge of the system "sees" the material at the right edge. This explanation is a highly simplified view on the actual implementations in MD packages. With pbc the evaluation of potentials is a challenge especially for long-range interactions such as electrostatics.

While short-range interaction potentials such as Lennard-Jones can be treated with a cutoff radius, *e.g.* 12 Å, in electrostatics this causes unnatural distortion. Electrostatics is one major part of the force fields in MD and due to the long-range character the computational costs are quite high. For such long-range interactions different efficient methods have been developed. A widely selected method to treat long-range electrostatics is the Particle-Mesh Ewald Method (PME). It is combined with a local treatment of charges in the near-field segregated by a cutoff parameter. The accuracy and efficiency of PME was analyzed by Petersen [144].

NP(T) ensemble The simulation with constant number of atoms N, constant pressure P and constant simulation temperature T is required to simulate phase transitions occurring between the simulation start at starting temperature and the reaching of the simulation temperature. The NPT ensemble is also used to cluster the molecules when, for example, the starting condition is a randomly filled box.

The constant pressure ensures a drive towards compact systems while the molecules have enough space in the variable volume V to adjust to each other. Over time, after a wavering start, the density will rise and consolidate. All simulations with NPT ensemble used in this thesis used the Parrinello-Rahman method for pressure coupling [145, 146].

NVT ensemble Another widely used ensemble is the simulation with constant number of atoms N, constant volume V and constant temperature T (NVT). This simulation mode uses a constant size of simulation box and moves the atoms within this box. For solid state materials without phase transition at the simulation start this is a typical setting.

If there is no (common) periodicity expected, for example when two crystalline structures with largely different lattices are simulated, either a huge box has to be taken or no periodic boundary conditions can be applied. In the latter case the system has to be large enough so that edge effects do not affect the simulation of the studied phenomena in the bulk or at the interface between the two materials.

3.3.2.4. Amorphous morphology via rapid cooling

Rapid cooling approach can be used to model a realistic amorphous morphology starting from the chemical formula. First, the optimized molecular structure and the point charges generating the electrostatic potential are obtained using DFT calculations (see section 3.1.2). With this information a first starting box randomly filled with the requested number of molecules is created. From here on, Molecular Dynamics (MD) takes over with applied periodic boundary conditions.

First, the energy of the morphology is minimized ensuring a robust starting system. To overcome high, unnatural energy barriers possibly created within the random structure, the system then is simulated for a short time period (10 ps) in a closed, isochore and isothermal boundary (NVT ensemble) at $T = 800\ K$. In the starting volume the molecules have enough space to adjust to the surrounding environment. Next step is a 1 ns simulation still at high temperature of $T = 800\ K$ but now with applied constant external pressure $P = 1\ bar$. The simulation in this closed, isobar and isothermal condition (NPT ensemble) ensures the assembly of a compact morphology. Afterwards, the system is cooled down within 2.5 ns from $T = 800\ K$ to room temperature at $T = 300\ K$ in a simulated annealing protocol with constant pressure. Finally, the system is simulated

further 1 ns in equilibrium phase. All the steps together allow the generation of a realistic relaxed morphology for further analysis.

3.3.3. The Molecular Dynamics packages GROMACS and Amber

Several Molecular Dynamic packages are available, open source and commercial ones. Relevant for the presented work are the commercial code Amber [147] (University of California, San Francisco) and the good scalable open-source package GROMACS [58] (Stockholm Center for Biomembrane Research, Stockholm, Sweden and Biomedical Centre, Uppsala, Sweden).

The selected force field GAFF was developed for the Amber package and the force field structure of parameters is not compatible for direct implementation in GROMACS. For the data conversion from Amber to GROMACS, the group of Yonea wrote the ACPYPE package [138, 148, 149], the recommended tool to use GAFF with GROMACS.

Although introduced as atomistic approach, GROMACS provides a straightforward way to use it as a coarse-grained package. The atoms are treated as abstract units with defined interactions. This can be utilized by replacing atom types with more complex units, *e.g.* whole molecules or amino acids.

4. Ab-initio based charge carrier mobility prediction

The first challenge faced in this thesis addresses the prediction of the intrinsic charge carrier mobility of organic semiconductors. To match efficiencies of classic devices, *e.g.* on silicon basis, organic materials with high charge carrier mobility are required. Measurements of charge mobilities involve, for example, time-of-flight experiments (TOF) [150, 151]. From the transition time t_{tr} of the charge carriers through a material, the mobility μ is calculated. The relation between drift time and mobility is given in Equation 4.1. [152]

$$t_{tr} \quad = \quad \frac{L^2}{\mu V_0} \tag{4.1}$$

In here, t_{tr} is the transition time, μ the charge carrier mobility, L the covered distance and V_0 the applied electric field.

These measurements require several steps from synthesis and preparation of the material to the actual TOF experiment. As organic materials typically have low charge carrier mobilities, many different materials have to be analyzed to find suitable candidates. Scanning over a large numbers of new materials, though, is time intensive and costly.

Therefore, reliable ways to predict the charge mobilities by simulations are desired. It is important to develop a model, which is capable of predicting charge mobilities ranging over many orders of magnitude. Here, a new developed model for charge mobility prediction, introduced in section 2.2, is applied to five amorphous and two crystalline organic semiconductors and the results are compared with experimental data.

The organic materials selected for this study are listed in Figure 4.1. In alphabetical order, the amorphous materials are DEPB (1,1-bis-(4,4'-diethylaminophenyl)-4,4-diphenyl-1,3,butadiene), mBPD (N4,N4'-di(biphenyl-3-yl)-N4,N4'-diphenylbiphenyl-4,4'-butadiene), NNP (N1,N4-di(naphthalen-1-yl)-N1,N4-diphenylbenzene-1,4-diamine), pFFA (N,N'-bis-[9,9-dimethyl-2-fluorenyl]-N,N'-diphenyl-9,9-dimethylfluorene-2,7-diamine) and
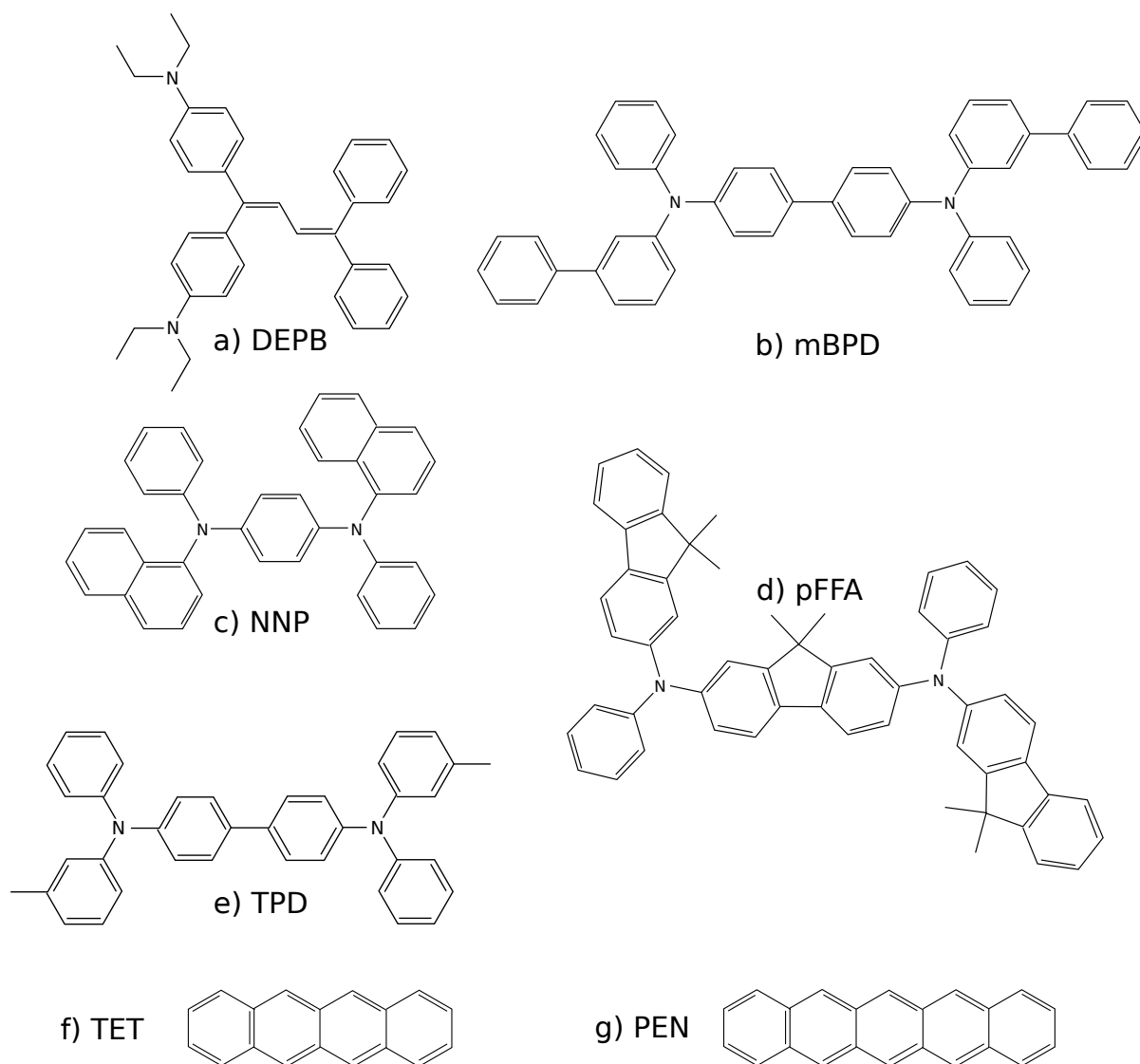
Figure 4.1.: Chemical formulae for the amorphous materials ($a - e$) and crystalline
materials ($f + g$) analyzed for their charge carrier mobility.
a) 1,1-bis-(4,4'-diethylaminophenyl)-4,4-diphenyl-1,3,butadiene (DEPB)
b) N4,N4'-di(biphenyl-3-yl)-N4,N4'-diphenylbiphenyl-4,4'-diamine (mBPD)
c) N1,N4-di(naphthalene-1-yl)-N1,N4-diphenylbenzene-1,4-diamine (NNP)
d) N,N'-bis-[9,9-dimethyl-2-fluorenyl]-N,N'-diphenyl-9,9-dimethylfluorene-
2,7-diamine (pFFA)
e) N,N'-diphenyl-N,N'-bis-(3-methylphenylene)-1,1'-diphenyl-4,4'-diamine
(TPD)
f) tetracene (TET)
g) pentacene (PEN)

TPD (N,N'-diphenyl-N,N'-bis-(3-methylphenylene)-1,1'-diphenyl-4,4'-diamine). The two crystalline materials are tetracene and pentacene. Their hole mobility has been addressed by Lee *et al.* [18] where no reliable model for hole mobility prediction over several orders of magnitude was found.

The workflow for charge carrier mobility estimation is based on Equation 2.5 and starts with the preparation of the material morphology. On this morphology, four QM parameters are calculated by DFT, *i.e.* the reorganization energy, the electronic coupling parameter, the average number of hopping partners and the local energy disorder. Finally, the mobility is calculated with the acquired parameters. The dependence of calculated results as function of both MD and DFT model is investigated.

4.1. Morphology preparation with Molecular Dynamics

Following the steps for rapid cooling in 3.3.2 five Molecular Dynamics morphologies for the five amorphous organic semiconductors with 300 molecules each were prepared[1]. As a first reliability check for the morphologies the density was the calculation from the simulated systems. The density and box boundaries are listed in Table 4.1. A comparison with experimental data cannot be done here as to the knowledge of the author no experimental data has been published on these materials at the time of writing. But in general, a density near and above $1 \frac{g}{cm^3}$ is expected. The dependence of the calculated mobility on the system size is addressed by am additional morphology with 500 DEPB molecules.

Determination of crystal morphologies The other two materials taken into account for the mobility trend analysis are the crystalline tetracene and pentacene. The crystal morphologies were generated with the Mercury package [56] with data listed in Table 4.2 obtained from the CCDC [55, 153, 154]. For pentacene 288 molecules and for tetracene 308 molecules were added.

Based on these morphologies, the QM parameters $\langle J^2 r^2 \rangle$ and σ, required for the mobility estimation, can be calculated. But first, the reorganization energy λ is addressed. The calculation procedure for λ depends only on the internal degrees of freedom of the molecules. Starting from the chemical formula, the calculation is done on single molecules in vacuum.

---

[1]Morphologies were prepared by Tobias Neumann from the research group of Wolfgang Wenzel

4. Ab-initio based charge carrier mobility prediction

Table 4.1.: Properties of generated MD morphologies with 300 molecules each and for DEPB another one with 500 molecules. The material density was averaged over 100k simulation snapshots taken over $1ns$. The edge length of the MD simulation box varies under periodic boundary conditions from simulation time step to time step with applied NPT ensembles. The listed values are taken from the last simulation snapshot.

material	density in $\frac{g}{cm^3}$	box edge length in nm
DEPB	1.009	6.275300
DEPB (500)	1.010	7.437352
mBPD	1.102	6.615257
NNP	1.121	6.112160
pFFA	1.039	7.143676
TPD	1.072	6.214204

Table 4.2.: Crystal parameters for tetracene and high temperature (HT) pentacene and references used for morphology generation with Mercury package. a, b and c represent the cell length of the crystal's unit cell, α, β and γ the angles between the cell edges.

crystal	a	b	c	α	β	γ	density in $\frac{g}{cm^3}$
tetracene [153]	7.900	6.030	13.530	100.30	113.20	86.30	1.301
pentacene (HT) [153, 154]	7.900	6.060	16.010	101.90	112.60	85.80	1.335

4.2. Molecular parameters from DFT

4.2.1. Reorganization energy

For the materials studied in this work, λ is the first parameter calculated for mobility estimation. Based on the chemical structure, the (effective) reorganization energies λ for charge transport in all seven materials are calculated according to the procedure explained in Section 2.2.2. For the DFT calculation the functional B3-LYP and the basis set TZVP are selected. The results listed in Table 4.3 are used for all following charge carrier mobility calculations.

Table 4.3.: Reorganization energy λ for the selected materials calculated with DFT with functional B3-LYP and TZVP basis set. First, the values for the five amorphous materials DEPB, mBPD, NNP, pFFA and TPD are given, followed by data for the crystalline materials tetracene and pentacene.

material	λ_{HOMO} in eV	λ_{LUMO} in eV
DEPB	0.3305	0.4396
mBPD	0.2602	0.3145
NNP	0.4312	0.1616
pFFA	0.1866	0.1553
TPD	0.2823	0.4957
tetracene	0.0996	0.1398
pentacene	0.1088	0.1256

With reorganization energies around $\lambda_{\mathrm{HOMO}} \sim 0.1 eV$ and $\lambda_{\mathrm{LUMO}} \sim 0.13 eV$ for crystalline materials are, as expected, lower than the values of the amorphous materials. NNP shows the highest reorganization energy λ_{HOMO} for the hole transfer while λ_{LUMO} for electron transport is highest for DEPB and TPD. Since the reorganization energy acts similar to an energy barrier for the transfer process, a large reorganization energy slows down the mobility.

4.2.2. Electronic coupling and number of transfer partners

The electronic coupling J_{ij} [63, 64] between the molecule pairs (i, j) determines the hopping process on molecular level. The larger the orbital coupling, the higher the probability

of charge transport between the molecules.

The number of molecule pairs grows quadratic with the number of molecules in the system, but the coupling is a local effect. For efficient usage of computing resources, only pairs within a certain range are considered for the effective coupling contribution. Here, the maximal atom-atom distance $r_{ij,aa}$ of neighboring molecules was set to 0.6 nm. A cutoff based on the center-of-mass distance $r_{ij,com} = r_{ij}$ of the molecules can also be used. While for sphere-like molecules $r_{ij,com}$ is more efficient, applied to long molecules like mBPD or pentacene many pairs would be found without any orbital overlaps others could be misses.

The numbers of pairs N_{pairs} found per system are listed in Table 4.4. According to Equation 2.9, the number of pairs with non-zero coupling contribution is required. Therefore, the number of contributing pairs to the charge transfer is added. N_{HOMO} is the number of non-zero contributions for the HOMO coupling, contributing to the hole transport, and N_{LUMO} is the number of pairs with LUMO coupling involved in the electron transfer. A few percent of the pairs have no orbital overlap in amorphous materials. This observation and the knowledge that the mean electronic coupling falls exponentially with the molecule distance, the cutoff of 0.6 nm seems to be justified.

From the number of pairs N_{HOMO}, N_{LUMO} and the total number of molecules in the system N_{mols}, the average numbers of hopping partners, *i.e.* the parameters M_{HOMO} and M_{LUMO} for the mobility calculation, can be determined following Equations 4.3 and 4.3, respectively.

$$M_{\mathrm{HOMO}} = N_{\mathrm{HOMO}}/N_{mols} \tag{4.2}$$

$$M_{\mathrm{LUMO}} = N_{\mathrm{LUMO}}/N_{mols} \tag{4.3}$$

The average number of transfer partners for electron transport is higher than the number for hole transport, except for NNP. The higher coupling for electron transfer suggests a higher electron than hole mobility. All pair related numbers can be found in Table 4.4.

For the mobility estimation, according to Equations 2.5 and 2.9, the electronic coupling J_{ij} is averaged together with the distance r_{ij} between the center of masses of the paired molecules. The distance between any two molecules is fixed for a given morphology. The result for the orbital coupling, however, depends on the DFT accuracy. Since the error on DFT level is not known, two different functionals were used to calculate the effective coupling. The more complex functional B3-LYP is expected to deliver more accurate values but takes more computing resources. In Figure 4.2 the obtained values for the seven systems are displayed. The data obtained with BP86/SV(P) is shown in

Table 4.4.: Number of molecule pairs in the morphologies. For the amorphous materials the numbers obtained from the final MD structure are listed. First, the values for the five amorphous structures are given, followed by the data for the two crystals. For the total number of pairs N_{pairs} only neighboring molecules with a maximal atom-atom distance $r_{ij,aa}$ of 0.6 nm are considered. The numbers for the hole transport N_{HOMO} and electron transport N_{LUMO} only count pairs with an electronic coupling $J_{ij} \neq 0$, *i.e.* larger than the numerical accuracy. Together with the number of molecules in the system the average number of transfer partners M per molecule is calculated. The electronic couplings were calculated using data from DFT calculations using functional BP86 and basis set SV(P).

material	N_{mols}	N_{pairs}	N_{HOMO}	M_{HOMO}	N_{LUMO}	M_{LUMO}
DEPB	300	2708	2640	8.80	2667	8.89
	500	4703	4568	9.14	4617	9.23
mBPD	300	2926	2648	8.83	2672	8.91
NNP	300	2559	2414	8.05	2314	7.71
pFFA	300	2554	2358	7.86	2418	8.06
TPD	300	2821	2685	8.95	2739	9.13
tetracene	308	2459	2459	7.98	2459	7.98
pentacene	288	2026	2026	7.03	2020	7.01

light green, the data from B3-LYP/TZVP are marked in black. On the left hand side, $\langle J^2 r^2 \rangle$ for HOMO related data is shown, the right side shows the values obtained for LUMO. As expected, the values for the crystalline materials clearly show a higher value for $\langle J^2 r^2 \rangle$ corresponding to the expected higher charge mobility. Additionally, with only one exception, the coupling parameter obtained with the larger basis set TZVP and the more complex functional are higher.
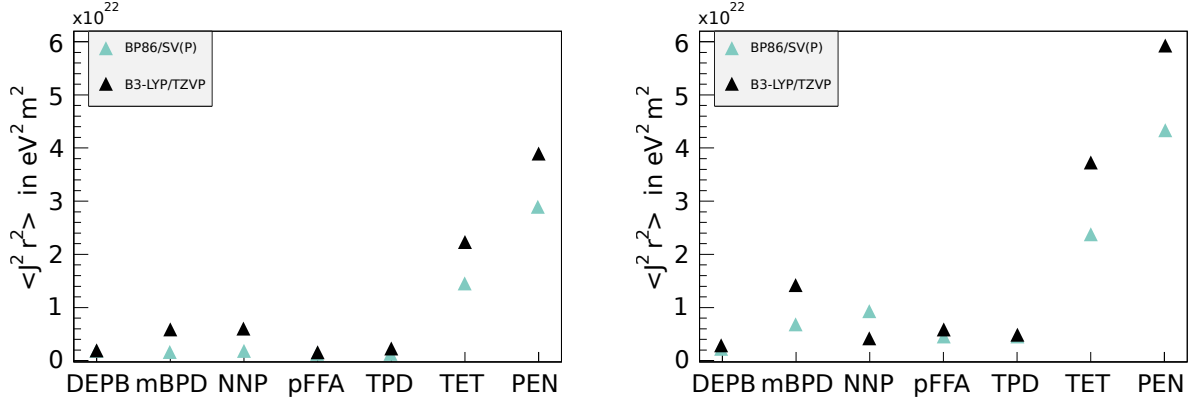
Figure 4.2.: Electronic coupling parameter $\langle J^2 r^2 \rangle$ of the molecular orbitals for different materials with varied functional/basis set settings - BP86/SV(P) (light green) and B3-LYP/TZVP (black). Left: Data for highest occupied molecular orbitals (HOMO) Right: Data for lowest unoccupied molecular orbitals (LUMO).

Beyond the dependency on the settings on DFT level, the parameter $\langle J^2 r^2 \rangle$ largely depends on the morphology. While the crystal morphology is well defined, the amorphous materials are created by MD simulations. As mentioned in the MD section 3.3, reliable values for observables in MD simulations are typically obtained by averaging over several snapshots taken during simulation in equilibrium. Although the morphology is expected to be realistic, thermic aspects such as molecule movements can influence the molecular orientations from simulation step to simulation step. Next, the parameter $\langle J^2 r^2 \rangle$ is calculated on snapshots of the same equilibrated systems at different simulation times. Additionally, the influence of the system size is analyzed at the example of DEPB, where systems with 300 and 500 molecules are compared.

As expected, the values for $\langle J^2 r^2 \rangle$ differ from snapshot to snapshot shown for HOMO in Figure 4.3. The ratio of the uncertainty lies between 5.33% and 8.82%. On the left side of Figure 4.3, the parameter values for $\langle J^2 r^2 \rangle$ obtained from ten snapshots of the amorphous materials are depicted. In addition to the single computed parameters displayed in the
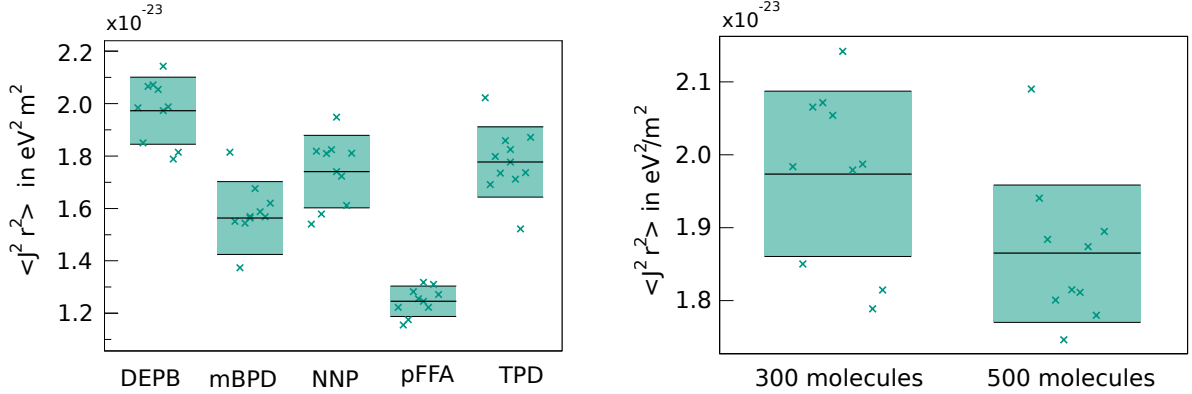
Figure 4.3.: Electronic coupling of the highest occupied molecular orbitals (HOMO) in amorphous materials for several different MD snapshots (cross marker). All snapshots for one material are taken from the same simulation within equilibrium phase. The mean value is marked by a black horizontal line surrounded by a light green area marking the width of the uncertainty, *i.e.* the standard deviation. Left: $\langle J^2 r^2 \rangle$ of MD snapshots for different materials. Right: $\langle J^2 r^2 \rangle$ of MD snapshots of DEPB morphologies for different system size.

figure, the averaged value is highlighted with a horizontal line surrounded by a light green area representing the standard deviation of the values. While pFFA shows only small deviation of 4.5%, the other material reveal large fluctuations around 6-9%. The influence of the system size, shown in Figure 4.3 right hand side, is less distinct than the effect of thermal fluctuation between each representative morphology. The averaged value for the larger DEPB system lies within the standard deviation of the smaller system and most values obtained from the snapshots of the larger system lie within the spread of the smaller DEPB system. The standard deviation is with 5.3% smaller than in the larger system with 6.4%. For more accurate results smaller samples can be used.

To summarize, Tables A.1 and A.2 in the appendix list all calculated parameters $\langle J^2 r^2 \rangle$ for HOMO and LUMO. For the systems where different snapshots are considered, the standard deviation is added. Overall, a good agreement between the different DFT configurations can be seen. According to this data, the crystals are expected to have the highest charge mobility. Reading from linear dependency of the mobility μ on $\langle J^2 r^2 \rangle$ in Equation 2.5 the uncertainty of $\langle J^2 r^2 \rangle$ directly correlates to the uncertainty of μ. In case of the larger morphologies, this means, that the additional computing resources and costs are high compared to the small gain in accuracy. The usage of higher basis sets and more complex functionals, in contrast, seems to be a good investment of computing resources.

The next step towards charge carrier mobility estimation is the consideration of the energy disorder σ, the final missing parameter for the charge carrier mobility estimation. The energy disorder has the largest impact in the mobility and has to be determined carefully.

4.2.3. Energy disorder σ

The reliable calculation of molecular orbital energies E_i is done with DFT methods. A first approximation for these energies can be achieved with calculations with fixed coordinates in vacuum for each molecule in the system. This approach neglects all the surrounding molecules, especially the long range electrostatic field. A better approach is to calculate the molecules in matrix, where all surrounding molecules are represented by either their dipole or point charges on each atom, *i.e.* ESP charges explained in section 3.1.2. The environment will influence the electron orbitals and the energies of the quantum mechanically treated molecule, which in turn interacts electrostatically with its environment. Thus, to obtain an accurate energy landscape, a self-consistent loop for the dipole or ESP feedback calculation is required.
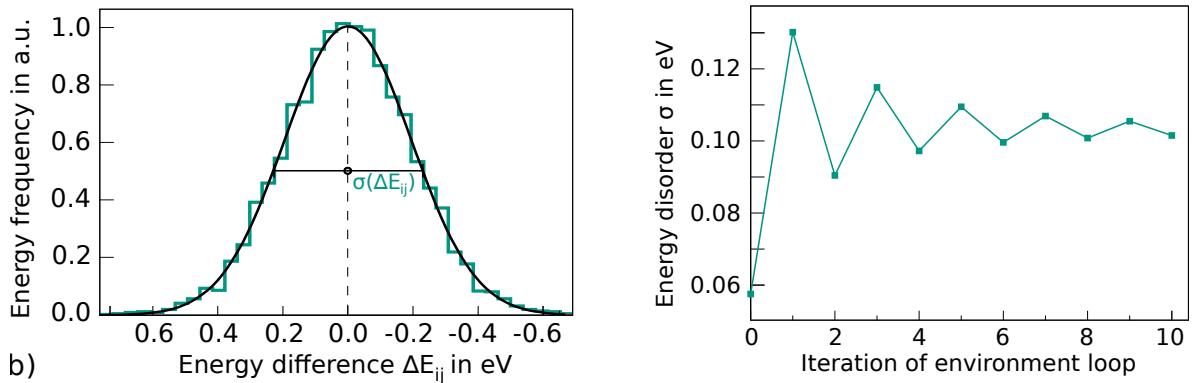
Figure 4.4.: Example for the energy disorder of neighboring pairs on molecular level for the highest occupied molecular orbitals (HOMO) of DEPB. Left: Distribution of the pair energy difference ΔE_{ij} between neighboring molecules calculated with DFT. The effective local energy disorder σ_{eff} is obtained by formula 2.12. In black, a Gaussian is added, fitted to the histogram values. The standard deviation of the distribution gives the value for the energy disorder $\sigma(\Delta E)$ within the material. Right: Calculated energy disorder σ of the molecular system after each loop of the self-consistent environment calculation.

In Figure 4.4 left hand side, the (self-consistent) local energy distribution of DEPB is

shown. The influence of the environment and the feedback loops on the local energy disorder is given in Figure 4.4 right hand side. For each iteration in the environment loop σ is calculated. As one can see, the energy disorder σ oscillates from iteration to iteration and slowly converges to a steady value. Adding a damping factor to the changes of the recalculated ESP charges or dipoles will fasten the convergence process.

The energy disorder σ in crystals is expected to be near zero since a crystal structure accounts for highly periodic systems. However, there are differences within the crystal's unit cell. Pentacene's and tetracene's unit cells consist of two molecules. The main contribution to the energy disorder in crystals arise from the difference in the molecule's orbitals of these two molecules in the unit cell. The amorphous structures are expected to have a larger energy disorder caused by the various molecular geometries present in the samples.

Following the same procedure as for the calculation of the electronic coupling parameter, first the energy disorder is calculated on one morphology per material using different functionals and basis sets. Additionally, different methods for the representation of the environment - dipoles and ESP charges - are tested. The calculation of the ESP charges takes an additional computing step after computing the dipoles but are expected to represent the environment in more detail.
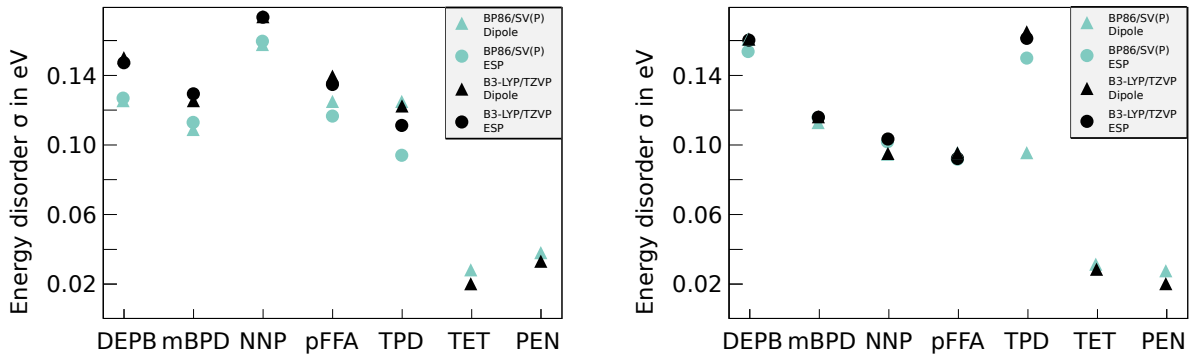
Figure 4.5.: Energy disorder σ calculated for different materials with varied environment representation and different functional/basis set settings. The results for the dipole representation of the environment is marked by triangles, the results with ESP charges marked by circles. The BP86/SV(P) and B3-LYP/TZVP settings are denoted by light green and black colors, respectively. Left: Energy disorder of the highest occupied molecular orbitals (HOMO). Right: Energy disorder of the lowest unoccupied molecular orbitals (LUMO).

4. Ab-initio based charge carrier mobility prediction

The results of the calculation are presented in Figure 4.5 - left the results for HOMO and right the results for LUMO are depicted. As expected, the crystalline materials have the lowest energy disorder, pointing to a high charge carrier mobility. NNP shows the widest distribution of orbital energy levels and should therefore have a much smaller charge carrier mobility.

The influence of the MD snapshot of the amorphous materials and the system size was investigated with the basic settings of dipole environment with functional BP86 and basis set SV(P). The data for HOMO are shown in Figure 4.6. For each material all snapshots are taken from the same simulation within equilibrium phase. In the appendix, all calculated values for the energy disorder are listed in Table A.3 for HOMO and Table A.4 for LUMO.
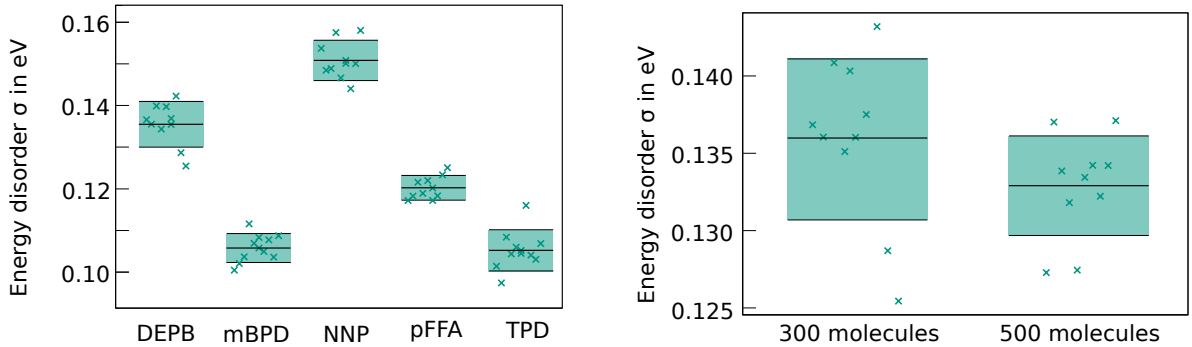
Figure 4.6.: Energy disorder σ of the highest occupied molecular orbitals (HOMO) in amorphous materials for several MD snapshots. The crosses mark the individual disorder values for the snapshots, while the average value of the disorder is marked by a black horizontal line surrounded by an light green area denoting the width of the standard deviation. Left: Energy disorder σ of MD snapshots for different materials. Right: Energy disorder σ of MD snapshots of DEPB morphologies with different system size.

On the left side of Figure 4.6 the values for the different materials with 300 molecules are presented. The right side shows the comparison of the DEPB systems with 300 and 500 molecules. In addition to the individual disorder values for each snapshot in the figure, the disorder average is highlighted with a horizontal line surrounded by a light green area representing the standard deviation of the energy disorder. In comparison to the electronic coupling parameter in Figure 4.3, the energy disorder σ shows a much lower scattering from snapshot to snapshot, ranging between 2.39% and 4.61%, shown in Figure 4.6. The deviation in the disorder parameters obtained by different snapshots is

again the lowest for pFFA as with the case of electronic coupling, shown in the previous section in Figure 4.3.

The changes arising from the system size shown in Figure 4.6 right hand side is small. The average local energy disorder σ of the larger DEPB system lies well within the deviation seen in the smaller one. Also the deviation in the larger system overlaps almost completely with the one of the smaller system. The accuracy for the large system is much better, but the average values differ little. However, owing to the high sensibility of the mobility formula 2.5 also small changes have large impact. This also counts for the other materials.

With the energy disorder covered, the last parameter for the charge carrier mobility estimation is calculated. But before discussing the calculated charge carrier mobility, first the correlation between the electronic coupling parameter $\langle J^2 r^2 \rangle$ and the energy disorder σ within the MD snapshots is analyzed.
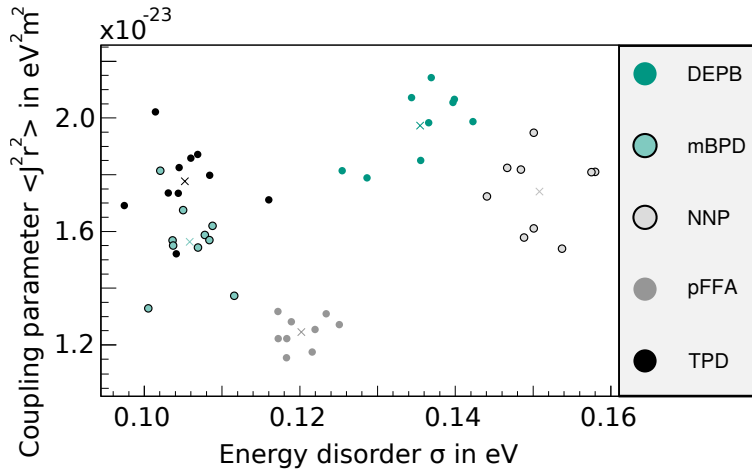
Figure 4.7.: Electronic coupling parameter $\langle J^2 r^2 \rangle$ in dependence of the calculated energy disorder σ for each snapshot. The circles represent parameter pairs on the same morphology. The crosses mark the pair of averaged parameter per material.

Both parameters, σ and $\langle J^2 r^2 \rangle$, rely on the morphology. To decide if the calculation of these parameters can be done independently, i.e on different morphologies, or if they require the same morphology for consistency, it is necessary to know if the pair of parameters is independent or shows a correlation with the morphology. In Figure 4.7 the coupling parameter $\langle J^2 r^2 \rangle$ is plotted against the disorder parameter σ obtained on the same morphology snapshots. The single values are marked with circles and the averaged values are marked with crosses.

The distribution of the parameter pairs shows low correlation. In terms of Pearson's correlation coefficient for a sample [155], the correlation lies between 0.003 for NNP and 0.042 for DEPB where 0 is no correlation and 1 is maximal correlation. The calculation of these parameters is therefore independent of the morphology. The steps of electronic coupling analysis and energy disorder examination can be done separately.

4.3. Charge carrier mobility in effective medium theory

After successful determination of the material parameters on molecular level, now, the charge carrier mobility is calculated according to Equation 2.5. The reorganization energy λ is related to the energy barrier along the reaction coordinate, slowing down the transfer. The same applies to the energy disorder σ. The smaller the energy disorder, the higher probability for charge transfer and the higher the charge carrier mobility μ. Also, as one can see in formula 2.5, high electronic coupling and larger mean distances covered with one charge hop will increase the mobility. All mobilities obtained are listed in Table A.5 for hole transport and in Table A.6 for electron transport in the appendix. The materials at hand are so called hole transport materials. Therefore, this section focuses on the hole mobility only.

Before making the comparison between the experimental data and the estimated charge carrier mobilities μ the method's accuracy is discussed. The accuracy of the mobility depends on the accuracy of the calculated parameters. For the six molecular systems with several snapshots considered an uncertainty s_μ for the mobility μ can be calculated according to the propagation of uncertainty of independent samples written in Equation 4.4. As impact factors σ and $\langle J^2 r^2 \rangle$ are considered while only one value for λ and M for each material are used as listed in Table 4.3 and Table 4.4. The propagation of uncertainty in independent samples is given as

$$s_\mu \;=\; \sqrt{\left(\frac{\delta\mu}{\delta\sigma}\right)^2 s_\sigma^2 + \left(\frac{\delta\mu}{\delta\langle J^2 r^2\rangle}\right)^2 s_{\langle J^2 r^2\rangle}^2} \tag{4.4}$$

with the uncertainties s_σ and $s_{\langle J^2 r^2\rangle}$ of the parameters σ and $\langle J^2 r^2 \rangle$ and with the two derivatives

$$\frac{\delta\mu}{\delta\sigma} \;=\; -\left(\frac{\beta^2}{2} + \frac{\beta}{\beta\sigma^2 + \lambda}\right)\sigma\mu \tag{4.5}$$

$$\frac{\delta\mu}{\delta\langle J^2 r^2\rangle} \;=\; \frac{\mu}{\langle J^2 r^2\rangle} \tag{4.6}$$

Table 4.5.: Uncertainties in the estimation of the hole mobility μ_{HOMO} obtained by data from BP86/SV(P) calculations with dipole environment of different snapshots per system.

material	$\left(\frac{\delta\mu}{\delta\sigma}\right) s_\sigma$ in cm^2/Vs	$\left(\frac{\delta\mu}{\delta\langle J^2r^2\rangle}\right) s_{\langle J^2r^2\rangle}$ in cm^2/Vs	s_μ in cm^2/Vs	s_μ in %
DEPB	5.54e-06	0.58e-06	5.57e-06	61.89
DEPB (500)	4.50e-06	0.65e-06	4.54e-06	37.13
mBPD	9.71e-05	2.76e-05	10.1e-05	32.32
NNP	2.42e-07	0.32e-07	2.44e-07	59.63
pFFA	3.57e-05	0.55e-05	3.61e-05	29.80
TPD	1.31e-04	0.22e-04	1.33e-04	44.27

The impact of the smaller relative uncertainty s_σ of the energy disorder σ on the mobility is expected to be higher then the impact of the relative uncertainty $s_{\langle J^2r^2\rangle}$ in the electronic coupling parameter $\langle J^2r^2\rangle$ as mentioned before. With the formula at hand, this can be confirmed. Table 4.5 lists the absolute contribution of the uncertainties s_σ and $s_{\langle J^2r^2\rangle}$ for HOMO as well as the resulting absolute and relative total uncertainty s_μ in the mobility. Without exception, the impact of s_σ is higher than for $s_{\langle J^2r^2\rangle}$ although the relative uncertainty for σ is lower. The high sensibility on σ causes the combined uncertainty to be much higher than the sum of the single relative uncertainty percent points. In total, s_μ lies between 29.80% and 61.89%. The consideration of the larger morphology for DEPB lowers the uncertainty from 61.89% substantially to 37.13%. Nonetheless, within this range of uncertainty from the method, only the order of magnitude in mobility can be expected to be matched. Also, this uncertainty only reflects the impact of the method and does not reflect the impact of the uncertainty on DFT level coming from the functionals and limited basis sets.

The experimental data published [18, 152, 156–164], refer to the hole mobility. All relevant published experimental data found are collected in Table 4.6, listing mobilities and the corresponding publication(s).

A summary of all calculated hole mobility values and the experimental data is shown in Figure 4.8 where the experimental data is displayed in gray bars with the range of experimental values highlighted with a light gray area. The mobility estimations coming from the amorphous materials with considered snapshot influence, based on BP86/SV(P) with dipole environment are represented as dark green areas for the uncertainty region

Table 4.6.: Experimentally measured hole mobility for all seven materials with corresponding publications.

material	hole mobility in cm^2/Vs	corresponding paper
DEPB	$5 - 8 \times 10^{-05}$	[18, 158]
mBPD	5.3×10^{-05}	[18, 156]
NNP	1.6×10^{-04}	[18, 156]
pFFA	1.1×10^{-03}	[157]
TPD	$\sim 1 \times 10^{-04}$	[18, 152, 158]
	$0.7 - 2 \times 10^{-03}$	[156]
	$O(10^{-04})$	[158][2]
	1.1×10^{-3}	[157]
tetracene	0.5	[159]
	0.4	[18]
	0.15	[160]
pentacene	3	[18, 161]
	$5 - 7$	[18, 162]
	1.5	[164]
	$0.3 - 1.5$	[163]

and a black line within for the mobility calculated with the mean values for σ and $\langle J^2 r^2 \rangle$. Hole mobility values for the same settings for the crystalline material are marked with a light green triangle. For all estimations only one value per material was used for the reorganization energy λ listed in Table 4.3 and for the average number of transfer partner M taken from Table 4.4. No points are added for the crystals with partial charge environment since unreasonable energy disorder values above 1 were obtained. Maybe using RESP charges from Bayly *et al.* [122] could improve these results.

In the comparison with the experimental mobilities, at the first sight, NNP stands out with a much too low mobility estimation. Roughly two orders of magnitude off is the estimation. The reason for this seems to be the high energy disorder. In contrast, the calculated hole mobilities for the other species lie within one order of magnitude of the experimental data. Within this range, all settings do not differ much. The B3-LYP/TZVP calculations, which are assumed to be more accurate, for mBPD, TPD and the two crystals lie near the data obtained with BP86/SV(P) while for DEPB, NNP and pFFA the values show lower charge mobility estimation.

4.4. Summary and outlook

The applied sophisticated workflow for charge carrier mobility estimation is a unique procedure covering amorphous and crystalline materials and is suitable for predictions over several orders of magnitude. As unique feature, the workflow is based solely on *ab-initio* calculations. In comparison with other approaches studied by Lee *et al.* this workflow gives reasonable values for most of the analyzed materials. This result indicates that charge carrier mobility in many organic semiconductors is well described by an effective medium theory. The detailed study on the influences within the method showed that more detailed computation on DFT level can improve the predictive power of the method. Especially the energy disorder can be treated more accurately. As seen, the rather small deviations in the energy disorder lead to large uncertainties in the mobility. The consideration of polarons can improve the determination of an accurate energy disorder for hole and electron transport. This requires a separate environment treatment for each molecule. Furthermore, the reorganization energy in this work is calculated in vacuum. Within the material, the molecules have less space to adjust the molecule's geometry. This consideration can lead to high changes in the reorganization calculation.
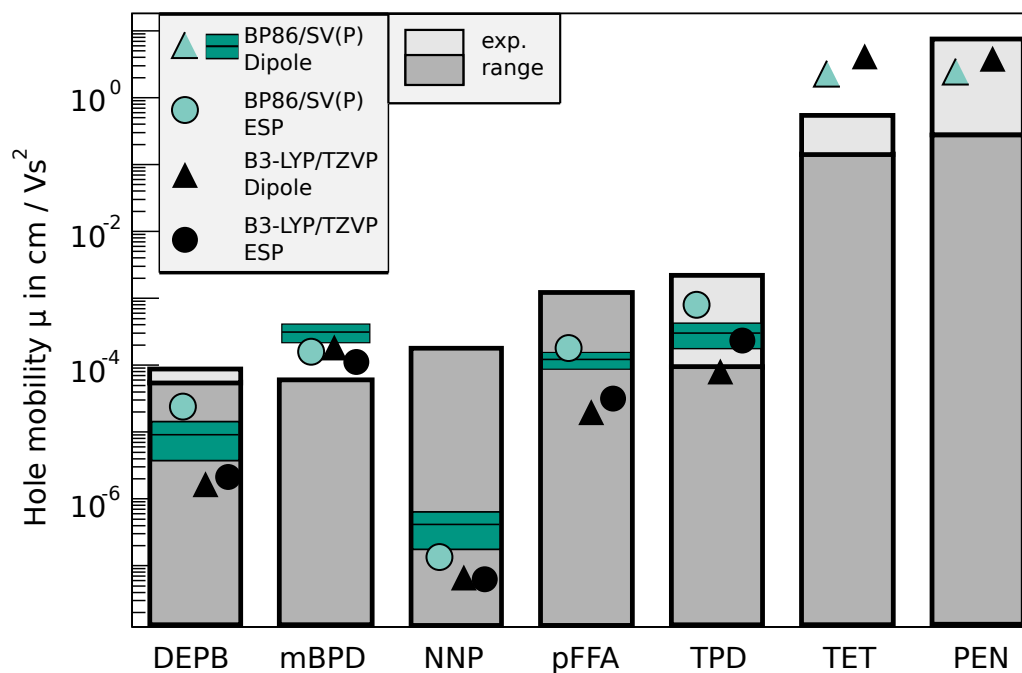
Figure 4.8.: Mobilities for hole transfer from Tables 4.6 and A.5. The gray bars mark the experimental values. The light gray represents the spread of published measured data. The data from this work refer to systems with about 300 molecules. The parameters used for mobility calculation of the light green triangles were obtained with BP86/SV(P) functional/basis set and an dipole environment. For the amorphous materials, the data is represented by a dark green area with horizontal black line marking the averaged value coming from the snapshots and the area of uncertainty. The light green circles show the data for BP86/SV(P) functional/basis set and a environment of partial charges. The black marker come from DFT calculations with B3-LYP/TZVP functional/basis set. The triangle mark data for dipole environment and the circles mark the mobilities for partial charge environment.

Another aspect requiring improvement is the information on the directional dependence of charge carrier transport. Pentacene is known to conduct especially well perpendicular to the molecule's long axis. This implies the high share of charge transfer along the π-π stacking direction [165]. The directional dependence of charge transfer cannot be covered with the analytical formula 2.5 for charge transfer. Instead, the calculated mobility is near the mobility along the preferred transfer direction. This part has the largest impact on the effective parameters.

The modular structure of the workflow makes it suitable for an implementation in a workflow engine, e.g. UNICORE. The separate calculation steps are independent from each other as explained. This also means that parts can be exchanged, e.g. to adjust calculations to other software packages available or adjust the complexity, e.g. the functional and basis sets used with DFT, to match available resources. Also, the integration into a more complex workflow for a whole device simulation is possible.

5. Interface-induced disorder

Typical organic electronic devices consist of several layers with differing intrinsic materials properties. After concentrating on the bulk materials properties such as charge carrier mobility in the previous chapter, here the focus lies on the interface between two organic, crystalline layers. Different work functions of the adjacent materials induce polarization, work function shift, the creation of geminate pairs [70] and dissociation of excitons [67]. Molecular disorder at the interface has a major impact on these phenomena [71, 72]. Therefore, understanding of the details of interface morphology, *i.e.* the molecular arrangements, is crucial. Here, a morphological study of the interface between crystalline pentacene (PEN) and perylene-3,4,9,10-tetracarboxylic dianhydride (PTCDA) is presented [71]. It was found that the interface-induced amount of disorder spreads differently into the two layers and is correlated with the choice of the corresponding crystal plane. The PTCDA crystalline layers are in general weakly distorted at the interface, while large regions of pentacene layer become disordered. In some interface arrangements, vacancies were observed, as well.

5.1. Preparation of morphologies

This work focuses on the interface between the two organic crystals pentacene and PTCDA (see Figure 5.1). Both crystals come in different polymorphs [154, 166]. In this work, only one modification for pentacene and one for PTCDA are used. For pentacene, the high temperature phase was selected, for which Yoneya *et al.* showed that this phase is more stable than the low-temperature phase, which will undergo a transition into the high temperature phase [154] when in contact with a substrate or exposed to vacuum. For PTCDA, the α modification was chosen. The crystal configurations for PEN and PTCDA are presented in Table 5.1 listing the crystal cell dimensions a, b and c and the angles α, β and γ between the cell edges.
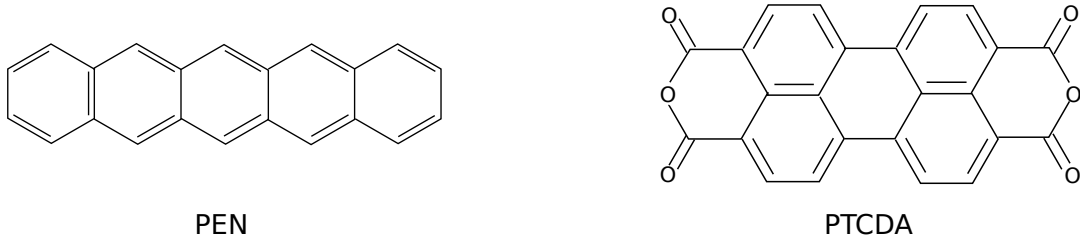
Figure 5.1.: Chemical formulae for perylene-3,4,9,10-tetracarboxylic dianhydride (PTCDA) and pentacene (PEN).

Table 5.1.: Crystal parameters for pentacene and PTCDA modifications used in this work.

crystal	a in Å	b in Å	c in Å	α in °	β in °	γ in °
pentacene (HT) [153, 154]	7.900	6.060	16.010	101.90	112.60	85.80
α-PTCDA [166]	3.740	11.96	17.34	90.0	98.8	90.0

An interface is build by two material surfaces, *i.e.* in this case crystal planes. Some materials, such as pentacene, show a substrate dependent alignment of molecules in crystal growth process [167]. Therefore, three different planes, denoted by the Miller indices (i, j, k), were selected for both materials. For PTCDA the three planes (102), (212) and (-221) were selected. While the plane (102) is a flat surface with herringbone pattern of the two molecules in the unit cell, the planes (212) and (-221) show a zigzag structure originating in the herringbone structure. The crystal planes (001), (010) and (100) were selected for pentacene. The (001) plane is characterized by the pentacene molecules standing on the plane while planes (010) and (100) expose the long axes of the molecules.

The distinct periodicities of the unit cells of both crystals prevent the use of periodic boundary conditions in Molecular Dynamics simulations. To avoid edge effects, simulations were performed using large systems with an analysis restricted to the inner part. Each crystal was arranged to fill a $10 \times 10 \times 5 \ nm^3$ box. The combination of these 3×3 planes led to nine different interface plane arrangements according to Figure 5.2 b). The crystal boxes were then joint in a distance of 0.3 nm as the estimated van-der-Waals distance of the molecules to build the $10 \times 10 \times 10 \ nm^3$ simulation boxes. This way, the influence of the joint crystal surfaces on the morphology can be studied in dependence of the different planes facing each other. As indicated in Figure 5.2 a), the selection of the interface planes leaves the relative orientation against each other as a rotational degree of freedom. In Molecular Dynamics, the overcoming of large energy barriers is difficult. To find the optimal relative orientation of the planes several simulations were started for
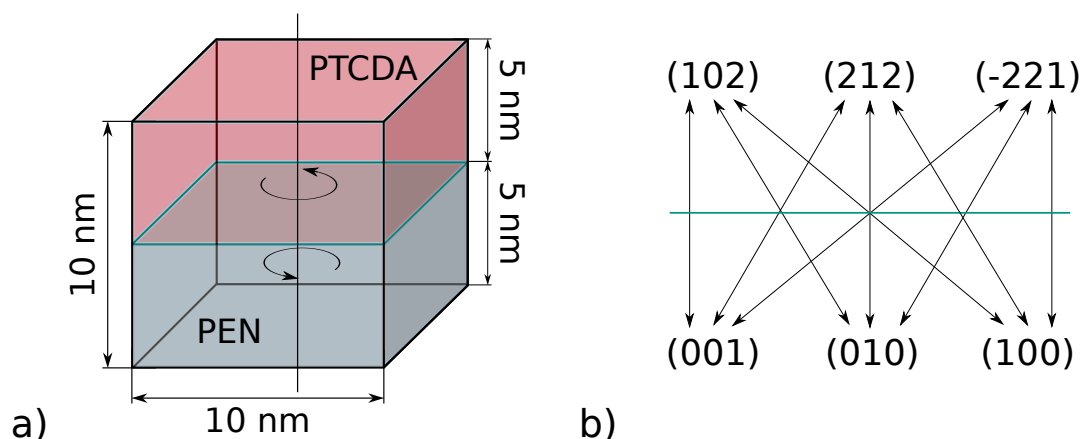
Figure 5.2.: Simulation box setup. a) Schematic overview of the simulation box of the size $10 \times 10 \times 10$ nm^3. The PTCDA crystal fills the upper half and the pentacene crystal the bottom half of the simulation box. The implicated rotations perpendicular to the interface plane indicate the rotational degree of freedom of the crystal surfaces towards each other. b) Combination of 3×3 surfaces to build the interface indicated by Miller indices. For PTCDA the crystal surfaces (102), (212) and (-221) are used. For pentecene (001), (010) and (100) are used.

each plane pair with the planes rotated against each other.

For the molecular representation in MD the force field GAFF [138, 139], was selected. The input files for the MD runs were generated with the ACPYPE package [148, 149] using ESP charges obtained with MOPAC [132]. A general check of the molecules' geometry was performed to verify a good representation of the molecules in the force field. A comparison between experimental [168], *ab-initio* [169] and MD data of this work is found in Table 5.2 presenting values of selected bonds and angles for a pentacene molecule. The MD simulation is in good agreement with the experimental and *ab-initio* data. This justifies the use of GAFF with MD for the material.

5.2. Interface simulations with Molecular Dynamics

After an energy minimization of the structures, the approximated interface distance of 0.3 nm is assumed relaxed and all force peaks are eliminated. After the minimization process, all systems were simulated with a time step of 0.5 fs for a simulation time of

Table 5.2.: Comparison of pentacene bonds and angles between experimental [168], *ab-initio* [169] and MD data from this work.

Bonds in pentacene in Å				Angles in pentacene in °		
bond	experiment	*ab-initio*	MD	angle	experiment	MD
C1-C2	1.441	1.43	1.397	C19-C18-C17	121	120.2
C2-C3	1.358	1.38	1.394	C18-C17-C16	123	120.1
C3-C4	1.428	1.44	1.395	C17-C16-C15	124	120.1
C4-C5	1.381	1.4	1.399	C16-C15-C14	124	120.3
C5-C6	1.409	1.42	1.395	C15-C14-C13	123	120.2
C6-C7	1.396	1.43	1.395	C14-C13-C12	119	119.8
C4-C21	1.453	1.43	1.403	C18-C17-C8	119	119.8
C6-C19	1.464	1.46	1.403	C16-C15-C10	118	119.9
C-H	n.a.	1.1	1.088	C8-C17-C16	118	119.8
				C10-C15-C14	118	119.8
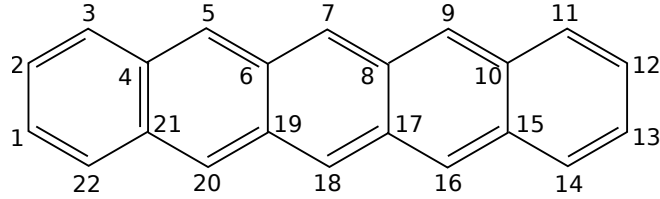
3 ns at a temperature of 300 K. A Berendsen thermostat [143] modeled the external thermal bath. The van-der-Waals interaction was cut at 1.2 nm and the electrostatics at 5 nm. The relative permittivity was set to $\epsilon_r = 4$ according to Wang *et al.* [170].

For the systems with the same planes facing the interface, the differences in mean energy per molecule delivers information on the local minimum of the simulations' phase space. The energy development of the PTCDA-(-221)/PEN-(100) interfaces is shown in Figure 5.3. The mean energy per molecule, after equilibrium was reached, is added as lines. The simulation with the lowest mean energy per molecule was taken as the most stable one and selected for further analysis.

After identifying the nine interface systems with lowest energy - one for each plane pair - the outer regions of these systems were cut to avoid contamination by edge effects. In the outer regions, the molecular behavior would not be physical. For the analysis of the morphology at the interface and in the bulk phase, an inner cube of the dimension $8 \times 8 \times 8$ nm^3 was cut around the system's center.

Figure 5.3.: Development of mean energy per molecule during simulation of PTCDA-(-221)/PEN-(100) interfaces. After convergence, the mean energy per molecule (lines) was fitted to the single snapshot energies (triangles).

5.3. Analysis of induced disorder at PTCDA/pentacene interfaces with distinct orientations

In order to quantify the disorder in the materials, the disorder parameter φ was used. The distribution of φ reflects the deviation of the morphology from the crystal bulk phase. φ is the pitch angle between the normal of the molecule's plane and the normal of the interface plane as depicted in Figure 5.4. The distribution of this angle for all molecules in the system along the normal of the interface indicates the spread of the disorder from the interface. The larger the deviation of φ from the crystal bulk value(s) the larger is the disorder in the layer. The thermic motion of the molecules in the force field potential at $300\,K$ induces a slight deviation from the ideal crystal bulk values.

Figures 5.5, 5.6 and 5.7 show the results for the nine different interface arrangements, sorted by the PTCDA interface plane from (102) over (212) to (-221). On the left hand side, the inner core after simulation is depicted. The green line marks the interface plane perpendicular to the image plane. The graph next to the morphology shows the distribution of the disorder parameter φ ranging between 0° and 180° in dependence of the distance to the interface. Far from the interface, the disorder parameter is approximately
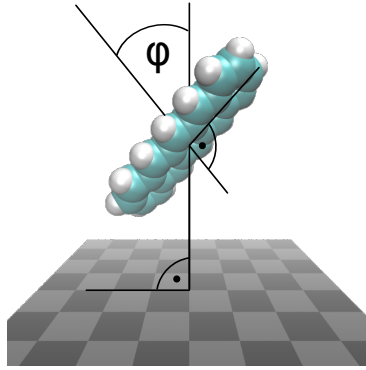
Figure 5.4.: Scheme for the pitch angle φ chosen as disorder parameter. The pitch angle φ is defined as the angle between the normal of the molecule's plane and the normal on the interface plane, here shown at the example of pentacene.

the crystal bulk value smeared by thermal movement. A divergence towards the interface denotes a disorder region induced by the interface electrostatics.

Two patterns can be observed in the equilibrated morphologies. The first pattern is the formation or better the retention of vacancies at the interface formed by standing pentacene plane (001) and zigzag surfaces (212) and (-221) of PTCDA shown in Figure 5.6 top and Figure 5.7 top. The two combinations PTCDA-(212)/PEN-(001) and PTCDA-(-221)/PEN-(001) preserve the crystal structure within each crystal. Only the first row of standing pentacene at the interface in PTCDA-(212)/PEN-(001) is slightly tilted to stand straighter. This indicates a strong and stabilizing interaction of π-π stacking within the crystals.

As second pattern, disorder is induced at the interface in most simulations. The unequal spread of disorder in pentacene and PTCDA is striking. While pentacene adapts to the new electrostatic environment at the interface, the PTCDA molecules stay in a stable crystal formation. This suggests a stronger intermolecular packing in PTCDA than in pentacene. For the PTCDA crystal plane (102) though, a tipping of the molecule planes can be observed. The pentacene molecules exposed to the zigzag structure of the PTCDA planes (212) and (-221) fill up the empty space at the interface drifting to the PTCDA crystal side. In filling the empty space at the interface formed with the pentacene plane (010) the pentacene molecules show a larger deviation of the disorder parameter than the molecules of the (100) plane.
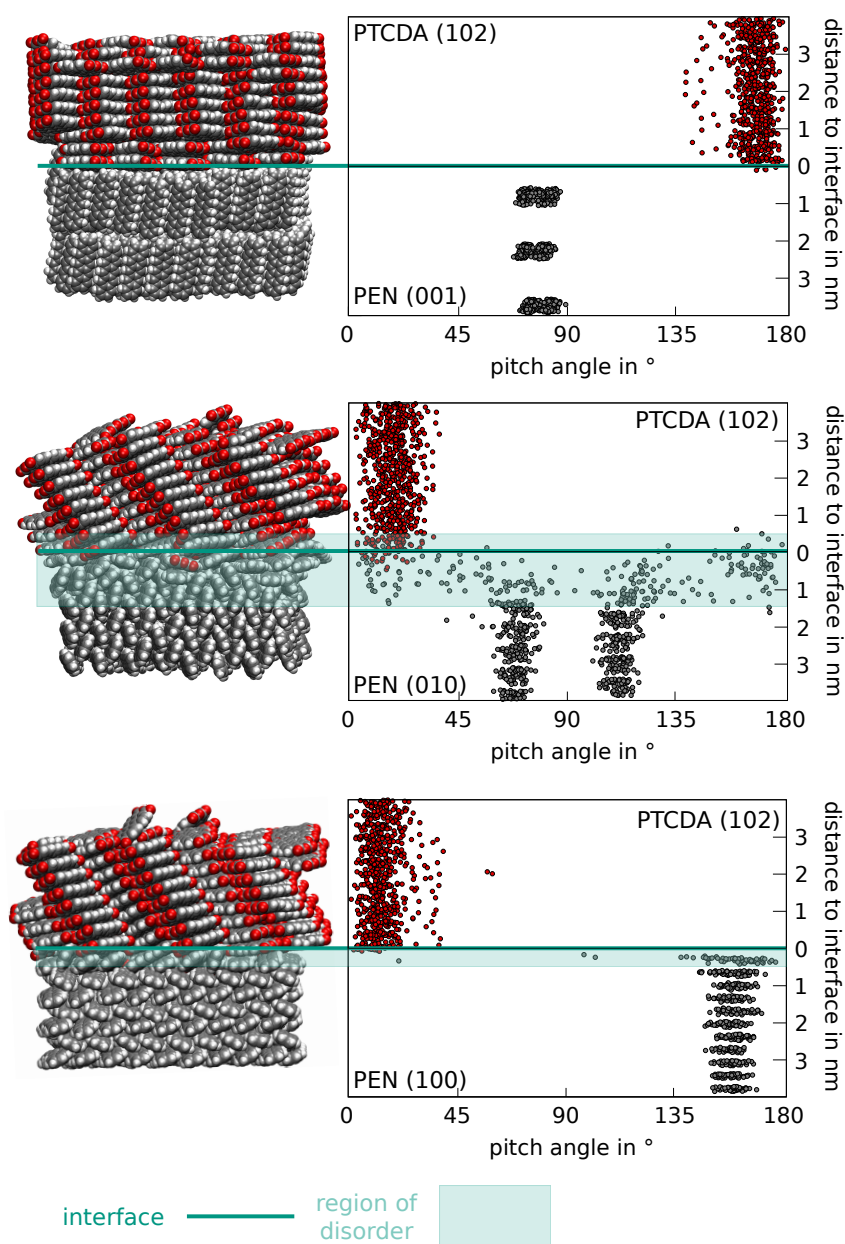
Figure 5.5.: Molecular disorder at (102)-PTCDA interface with three different pentacene (PEN) crystal orientations ((001), (010) and (100)). On the left, a snapshot of the inner cube is depicted. The graphs on the right side show the pitch angle φ (see Figure 5.4) in dependence of the distance to the interface. The region of disorder is highlighted in light green. Outside the disorder region, the crystals are in their bulk phase.

Figure 5.6.: Molecular disorder at (212)-PTCDA interface with three different pentacene (PEN) crystal orientations ((001), (010) and (100)). On the left, a snapshot of the inner cube is depicted. The graphs on the right side show the pitch angle φ (see Figure 5.4) in dependence of the distance to the interface. The region of disorder is highlighted in light green. Outside the disorder region, the crystals are in their bulk phase. In addition, interface PTCDA-(212)/PEN-(001) shows vacant sections, indicated with a light gray area.

Figure 5.7.: Molecular disorder at (-221)-PTCDA interface with three different pentacene (PEN) crystal orientations ((001), (010) and (100)). On the left, a snapshot of the inner cube is depicted. The graphs on the right side show the pitch angle φ (see Figure 5.4) in dependence of the distance to the interface. The region of disorder is highlighted in light green. Outside the disorder region, the crystals are in their bulk phase. In addition, interface PTCDA-(-221)/PEN-(001) shows vacant sections, indicated with a light gray area.

5.4. Summary and outlook

Two distinct effects can be observed at the interfaces of PTCDA and pentacene, namely, induced disorder and vacancies. Depending on the choice of the Miller-indices at the interface, the disordered region can extend between 0 *nm* and 1.6 *nm* from the interface into the material.

The simulations in this work based on static atomic charges, *i.e.* electrostatic potential (ESP) charges obtained from DFT calculations of single molecules in vacuum. The amount of disorder observed in the presented Molecular Dynamics simulations can be seen as upper bound at the interface of PTCDA and pentacene as no environment feedback loop for the calculation of ESP charges was implemented. The nature of electrostatic potential at the interface becomes more accessible when obtained charges reflect the local nature of their environment, *e.g.* by routine recalculation of charges with QM, semi-empirical methods, or by using polarizable force fields (AMOEBA) [171]. The effect of conservation of bulk properties, *i.e.* large interfacial vacancies, is likely to remain unchanged in simulations that are more accurate.

6. Polymer wrapping for nanotube sorting

In the previous chapters, two important aspects within the simulation of organic devices were treated with the focus on materials of small organic molecules. But organic electronic devices can also be composed of other organic materials, like polymers or carbon structures such as graphene or single-walled carbon nanotubes (SWCNTs). The selection of the right single-walled carbon nanotube type is essential for the proper functionality of devices and other applications since each SWCNT type possesses unique intrinsic properties such as diameter and bandgap [80, 81]. But the processes of mass-production of SWCNT deliver a mixture of a wide range of SWCNT types [25, 86]. A sorting mechanism using polymers seems promising for a capable sorting process. However, a broad and efficient prediction of selection ability of polymers for SWCNTs is not available. Here, the newly developed coarse-grained polymer wrapping model (CG-PWM) - introduced in chapter 2.5 - is applied to study the selectivity of polymers on SWCNTs quantitatively. The ability of the model to predict the selectivity is tested for four pyridine containing co-polymers (Section 6.2) and two more complex 9,9-dioctylfluorene containing co-polymers (Section 6.3).

CG-PWM can describe the wrapping process with only few parameters and, in contrast to methods used to date, CG-PWM can span the whole configuration space making quantitative predictions possible. With the help of CG-PWM, for example, time consuming experiments can be limited to pre-screened candidates for which the model shows a good ability for the selection process. Furthermore, by studying the underlying mechanism of the wrapping process, also a directed search for new polymers can be performed.

The prediction of the polymers' sorting ability starts with the consideration of the probability to find the wrapped conformation i of specific SWCNTs with a polymers given in Equation 2.14. In this equation the probability depends on the SWCNT type (n,m) and the SWCNT length. For the actual sorting and the following application of the SWCNTs,

only the SWCNT type identified by the indices n and m is the important property. Consequential, and taking Equation 2.19 into account, here, the selectivity s and the relative selectivity $p_{(n,m)}$ towards a (n,m)-SWCNT are defined:

$$s(k) \;=\; \sum_{i} e^{kE_{pd,i}} \tag{6.1}$$

$$p_{(n,m)}(k) \;=\; \frac{1}{s} \sum_{i|_{(n,m)}} e^{kE_{pd,i}} \tag{6.2}$$

with an unknown but polymer specific constant k and the dihedral energy cost E_{pd} of conformation i. The relative selectivity holds the sum over all conformation with (n,m)-SWCNTs. For consideration of the energetic threshold for stable conformations, amongst others arising from the entropic cost, a Heaviside step function can be added.

6.1. Prepararion of model representations

The geometrical representation of polymers in CG-PWM requires identification of building blocks in advance. In the model each building block has exactly two degrees of freedom, thus, each building block has to contain at least two rotatable dihedrals along the polymer backbone. If more than two backbone dihedrals are considered to build one building block, all but two have to stay put. Each building block has to contain a large conjugated structure assumed to form a wide electron orbital overlap, *i.e.* π-π stacking, with the SWCNT surface.

After identification of the intrinsic building blocks, the optimized molecular structure has to be obtained and the dihedral energy potential surfaces have to be calculated. For this, the dihedrals of the optimized structures are rotated and the ground-state energy with fixed coordinates is calculated in regular steps. From the obtained energies, the dihedral energy potential surface can be estimated, e.g by using B-splines or linear approximation in case of detailed data. The polymers studied in this work, were optimized with DFT methods using the B3-LYP exchange correlation functional and TZVP basis set.

Additionally, an effective nanotube diameter has to be defined. On the basis of the work of Wang [114], an additional distance between the SWCNTs and the polymers between 0.30 nm and 0.31 nm was selected.

6.2. Selectivity prediction of pyridine containing co-polymers

At first, the model was applied to four pyridine containing co-polymers [44]. The molecular structures are given in Figure 6.1. These polymers consist of alternating conjugated pyridine and fluorene in case of P1-P3 and of pyridine and carbazole in case of P4. The differences between the distinct polymers are merely small. For polymers P1-P3 only the connectivity of the pyridyl group varies as shown in the first column of Figure 6.1. P3 and P4 have the same connectivity of the pyridine group, but differ in the second moiety. Instead of a fluorene group, P4 has a carbazole-analogue. Furthermore, P1 is regiorandom in the position of the nitrogen in the pyridine group.

The four conjugated polymers P1-P4 consist of links containing exactly two backbone dihedrals. The identification of the building block therefore is strait-forward. To maximize the electron orbital overlap, the larger conjugated electron system is selected to be placed on the effective SWCNT radius. The second moiety is used as hinge. The building blocks for polymers P1-P4 can be seen in Figure 6.1 where first, the chemical formulae are given, second, the replacement with geometrical building blocks is depicted and finally, the obtained dihedral energy potential surfaces for each rotatable backbone dihedral is shown. The dihedral energy calculations were done every 10 degrees, *i.e.* 36 calculations in total for each dihedral rotation. The DFT calculations were done on a dimer with the evaluated dihedral centralized. The energy potentials show distinct minima and maxima.

Despite of the similarities in the polymer structures, two different patterns are observed for the dihedral energy potential surfaces. On the one hand, four maxima and minima are shown for polymer P2. Polymers P3 and P4 show only two strong maxima in energy and a wide low energy potential surface in between. For polymer P1 the shape differs depending on the location of nitrogen in the pyridine ring. While P2 - P4 have symmetrical energy potentials in both rotations, see Figure 6.1 b) to d)), polymer P1 involves an asymmetry in the two potential surfaces (see Figure 6.1 a)). Besides the differences in energy potential surfaces, the molecular structure, *i.e.* the fixed angles γ and δ between the moieties along the polymer backbone, differ as listed in Table 6.1.

With these data, CG-PWM was applied to the four pyridine containing polymers using seven different effective radii corresponding to tube diameter of 0.72 nm, 0.8 nm, 0.9 nm, 1.0 nm, 1.1 nm, 1.2 nm, 1.25 nm. The model outputs a list of mathematical conforma-
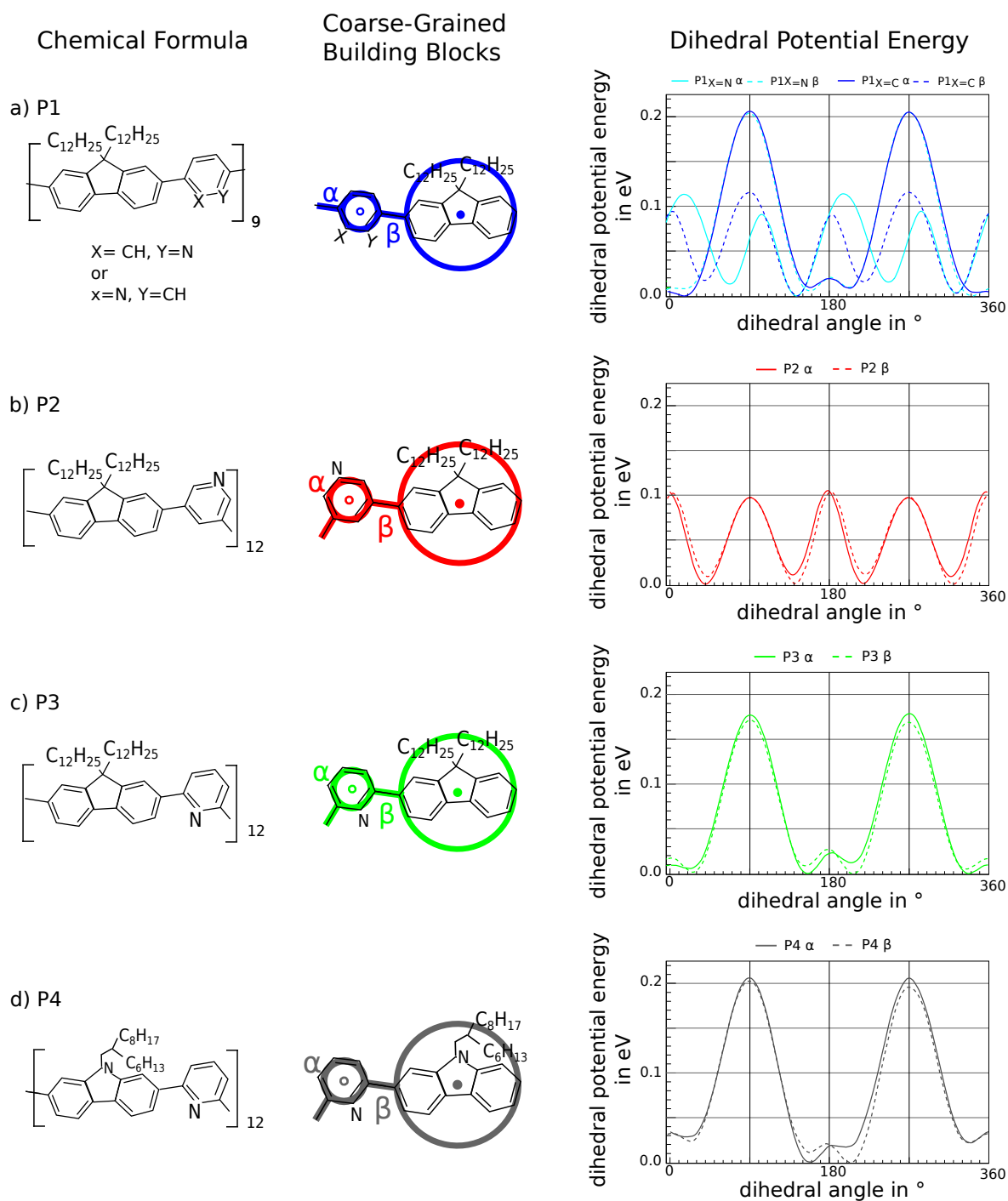
Figure 6.1.: Input data for CG-PWM. a)-d) show the data for the four studied pyridine co-polymers. The first column shows the chemical formulae, followed by the defined building blocks. The last column shows the dihedral energy potential surfaces for each rotatable bond.

Table 6.1.: Molecular, angular parameters of relaxed polymer geometry. The data was obtained by DFT calculations with B3-LYP functional and TZVP basis set.

polymer	γ in °	δ in °
P1	160.1	177.6
P2	160.1	121.8
P3	160.6	115.0
P4	156.2	115.1

tions with the corresponding flection energy costs per effective diameter. The results up to a flection energy of 1.2 eV are displayed in the 2D-histograms in Figure 6.2.
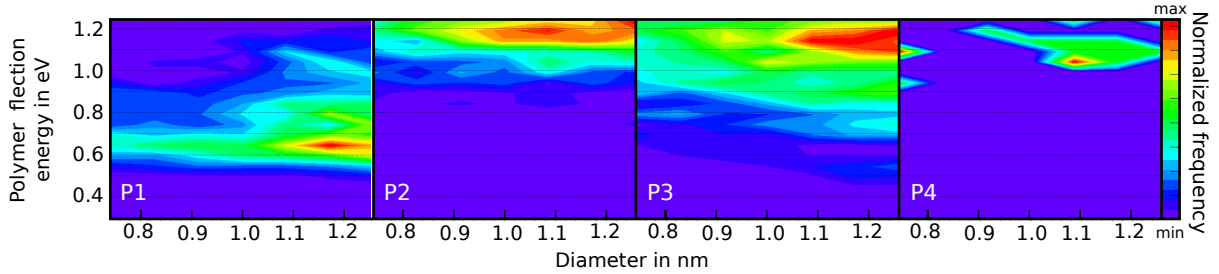
Figure 6.2.: Normalized frequency of conformations sorted by flection energy and SWCNT diameter.

The distributions of conformations show a clear trend of increasing number of conformations with rising SWCNT diameter for each pyridine co-polymer. Nonetheless, as the conformations with lower flection energy are more likely to be formed, the results have to be weighted in dependence of the energy. Also, as the energy level clearly differ between the distinct polymers, separate weighting should be applied. Since only few diameter were used to calculate the selectivity of the pyridine co-polymers, the sum in Equation 6.2 has to be changed from (n,m)-type SWCNTs to configurations of the same diameter d:

$$p_{\text{d}}(k) \quad = \quad \frac{1}{s} \sum_{i|_d} e^{kE_{pd,i}} \tag{6.3}$$

The results obtained by CG-PWM for the four polymers P1 - P4 and the corresponding experimental data for the relative selectivity p_d obtained by the research groups of Marcel Major and Manfred Kappes [44] are shown in Figure 6.3. The constant in Equation 6.3 was chosen to be 0 and the energy weight was applied as a plain energy threshold. The predicted relative selectivity (green circles) agrees well with the experimental data (black
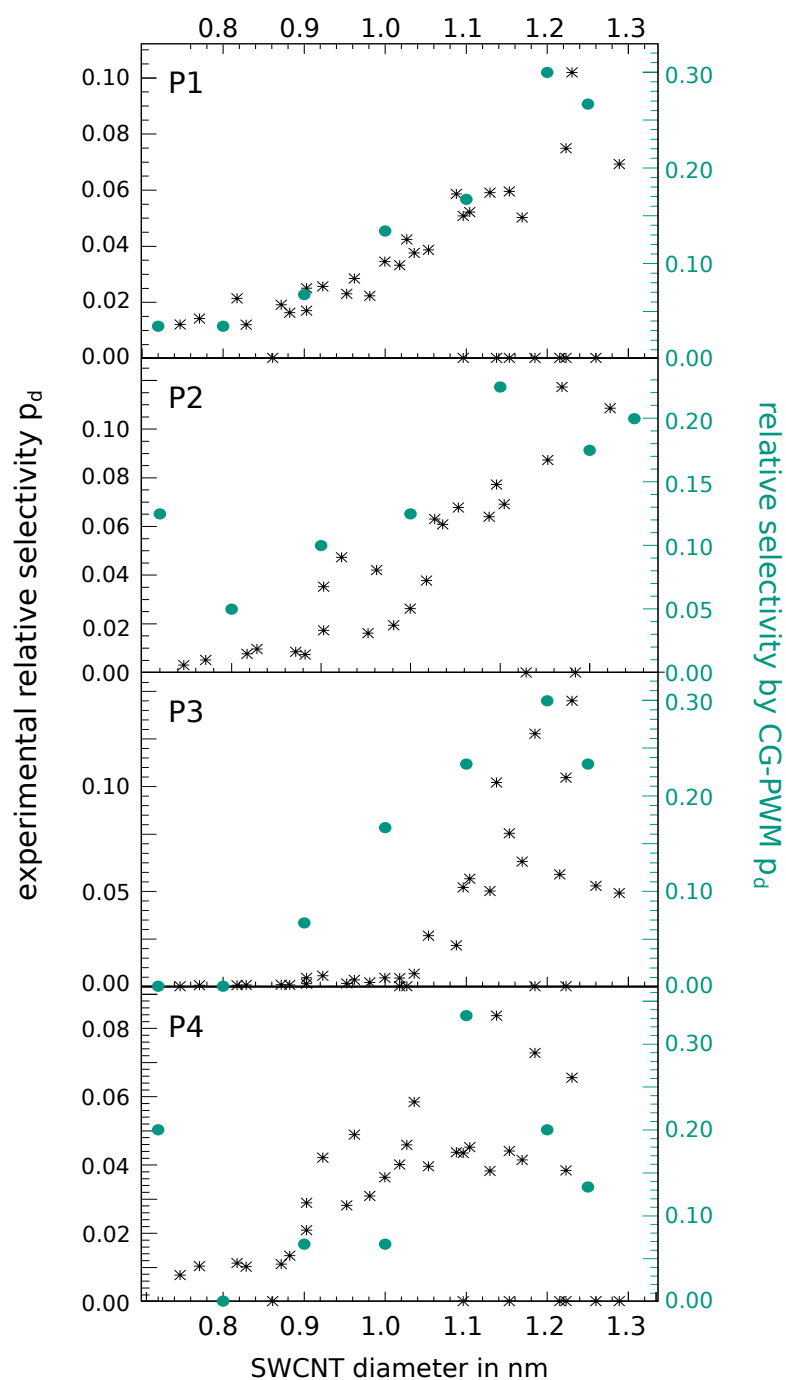
Figure 6.3.: Predicted relative selectivity p_d (green circles) and experimental PLE data (black stars) for pyridine co-polymers P1-P4 are shown. Due to the unequal number of data points, the y-axes are arranged so that the maxima are on the same height.

stars). For simplified comparison the maxima of the theoretical and experimental data are displayed at the same plot height and the scale is given on different axes. The agreement between the data for polymer P1 is excellent. The comparison for the other polymers show only small deviations, though, for small diameters, the selectivity of P2 and P4 is overestimated. Most data for P3 show consistent absence of conformations for smaller diameter than 0.9 nm. In summary, the trend in the plain numbers of conformations towards larger diameter is not retained but a maximum in selectivity is predicted and observed between 1.1 nm for P4 and 1.2 nm for P1 and P3.

Although, P1 - P4 show only small deviation in molecular structure, the relative selectivities of SWCNTs show noticeable differences. The distinct connectivity of the pyridine moiety results in intrinsic angles between the outgoing bonds for P1 - P3. While the pyridine moiety stays the same, these varieties account for the behavior. The change between P3 and P4 arise from the exchange of the larger moiety from fluorene to carbazole. Minimizing the angle between these outgoing bonds apparently leads to wrappings of smaller diameter SWNTs without confining the selectivity toward larger diameter tubes.

6.3. Selectivity prediction of 9,9-dioctylfluorene containing co-polymers

So far, the geometrical coarse-grained model was applied to rather simple polymers with only two alternating backbone moieties. CG-PWM is designed to fit all conjugated polymers which can be divided into specified building blocks. Here, the procedure is tested against more complex 9,9-dioctylfluorene co-polymers with more than one building block per monomer.

Polymer P5 in Figure 6.4 has five rotatable dihedrals per monomer and polymer P6 six dihedrals. The division into two, respectively three building blocks was decided according to the moiety size. Since each building block needs two degrees of freedom, *i.e.* two free rotatable dihedrals, the polymer P5 required one building block with a fixed dihedral. As seen before in the preparation of the pyridine co-polymers, each dihedral energy potential surface is calculated in DFT with B3-LYP functional and TZVP basis set.

To exhaust the polymer wrapping model, the 9,9-dioctylfluorene co-polymers were simulated on effective diameter between 0.7 nm and 1.3 nm. For the comparison with experimental data, an additional step was applied. As the coarse-grained polymer wrap-
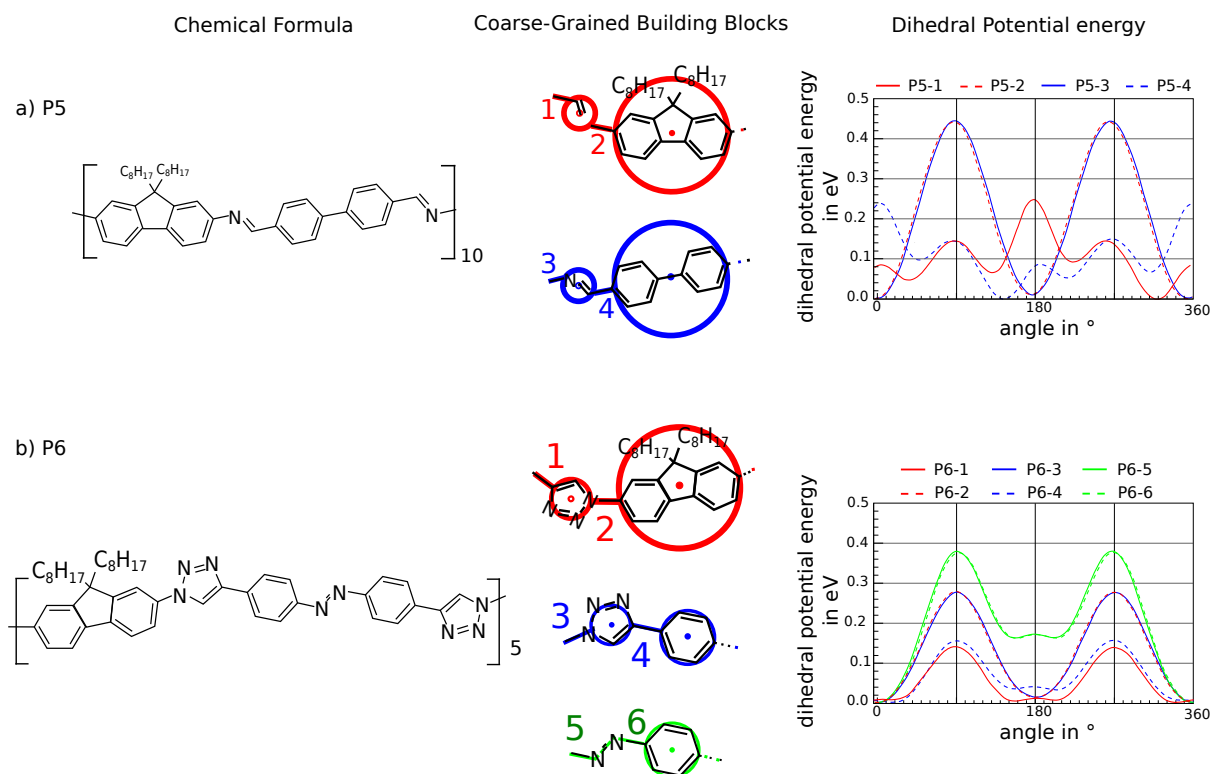
Figure 6.4.: Input data for CG-PWM for two conjugated 9,9-dioctylfluorene containing co-polymers. The first column shows the chemical formulae, followed by the defined building blocks. The last column shows the dihedral energy potential surfaces for each rotatable bond.

ping model delivers data of relative selectivity but experiments are based on SWCNTs mixtures with unequally distributed amount of distinct SWCNTs, the theoretical data now is weighted with the starting distribution $w_{(n,m),HiPco}$ of distinct SWCNTs.

As mentioned before, the experimental data used for this work were obtained using a HiPco fabricated SWCNT starting mixture[1]. The experimental measurements of SWCNT types in a probe is often done by a fluorescence spectra analysis as shown in Figure 6.5 a) and discussed in Section 2.4. Each emission peak stands for a defined SWCNT type [91]. The corresponding distribution of SWCNTs sorted by diameter and chiral angle is shown next to the experimental wavelength map in Figure 6.5 b) where the circle size represents the relative amount of SWCNT in the mixture. For the conformations of CG-PWM,

---

[1]The photoluminescence data were obtained by Nicolas Bertron and Fabien Lamasson from the research group of Marcel Mayor.
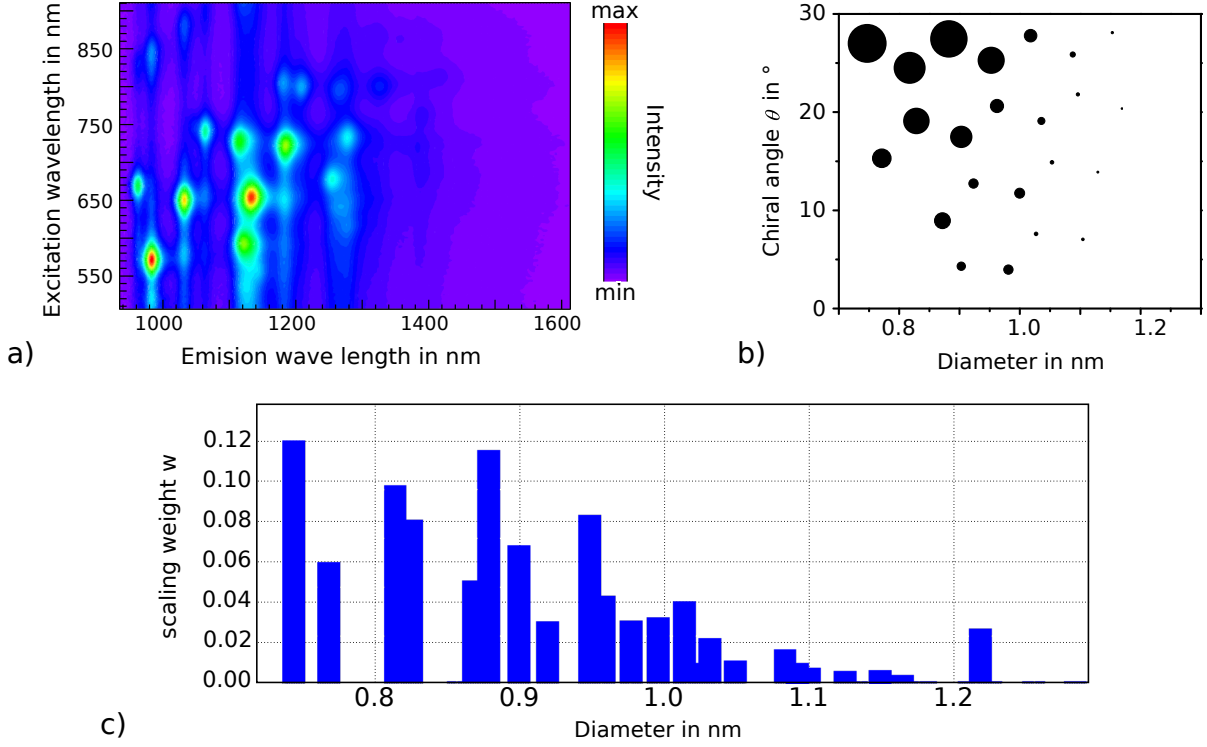
Figure 6.5.: Distribution of single walled carbon nanotubes created in HiPco [86] process. a) Photoluminescence data of intensity (color code) of emission wave lengths in dependence of the excitation wavelengths. b) Frequency of the SWCNTs in the HiPco mixture sorted by diameter and chiral angle. c) Histogram of weights $w_{(n,m),HiPco}$ to adjust the prediction to the experimental data.

only the diameter information is relevant, since the chirality is neglected. The extracted weights for the HiPco comparison are shown in the histogram 6.5 c).

The weighted relative selectivity $p_{(n,m),HiPco}$ is calculated from the weighted selectivity $s_{(n,m),HiPco}$.

$$s_{(n,m),HiPco}(k) \quad = \quad w_{(n,m),HiPco} \sum_i e^{kE_{pd,i}} \qquad (6.4)$$

$$p_{(n,m),HiPco}(k) \quad = \quad \frac{1}{s_{(n,m),HiPco}} \sum_{i|_{(n,m)}} e^{kE_{pd,i}} \qquad (6.5)$$

with $\sum_{(n,m)} w_{(n,m),HiPco} \equiv 1$.

After weighting the conformations by their energy and the relative SWCNT distribution w, the predicted relative selectivity $p_{(n,m),HiPco}$ is compared with the corresponding experimental data [45]. The findings are shown in Figure 6.3. The polymer specific constants

were set to k=1.67 for P5 and to k=4.33 for P6.
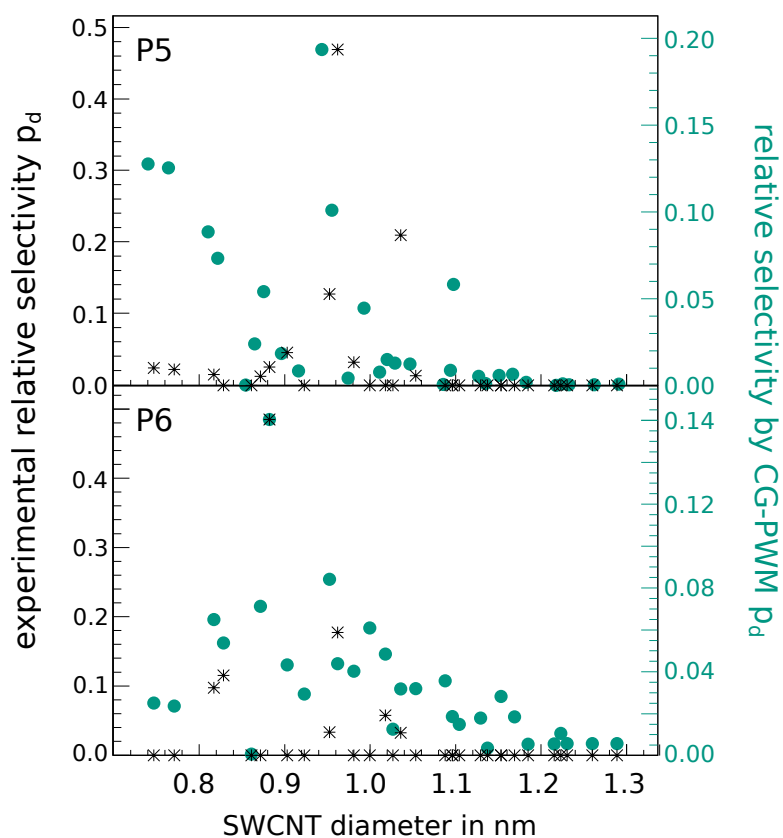
Figure 6.6.: Comparison of predicted relative selectivity (green circles) with experimental PLE data (black stars) for 9,9-dioctylfluorene co-polymers P5 and P6. The y-axes are arranged so that the maxima are on the same height.

The highest predicted selectivity lies in good agreement with the experimental data. But, as seen for P2 and P4, the selectivity for small SWCNT diameter is overestimated. The weighting of conformations with the experimentally available SWCNT distribution proved to be suitable and enhances the model for further studies.

6.4. Summary

The newly developed coarse-grained model for polymer wrapping around carbon nanotubes was verified to predict the selectivity of conjugated polymers for SWCNTs. The minor differences in the pyridine containing co-polymers' geometries could successfully be addressed and an excellent agreement with the experimental data was found. Also, the

more complex 9,9-dioctylfluorene containing co-polymers P5 and P6 could be studied and the relative and absolute selectivity determined. The results support the assumption of the dominant role of electron orbital overlap between the polymers and the SWCNT.

7. Conclusion and outlook

Modern electronic devices increasingly use organic materials components, thus making organic electronics and organic semiconductors an important research field.

The focus of this thesis was to develop and test multiscale simulation methods with application in three specific material aspects: the charge carrier mobility in amorphous semiconductors, the properties of organic-organic interfaces, and the investigation of specific conjugated polymers to help sort single-walled carbon nanotubes into pure species.

In the first part of the work, a sophisticated workflow was developed and tested to estimate the charge carrier mobility of amorphous organic semiconductors as an intrinsic material quantity from first principles. This approach is based on a recently developed effective medium theory, which was applied to seven different organic materials. The workflow starts with the generation of realistic molecular morphologies by molecular mechanics simulations. The atomistically resolved molecular model was then used in *ab-initio* methods to compute the material parameters.

The result of this effort was the computation of hole mobilities from first principles for a wide range of materials. The mobility covered a range of many orders of magnitude and were in order-of-magnitude agreement with experimental data. This result indicates that charge carrier mobility in many organic semiconductors is well described by an effective medium theory, an observation that is not easily reconciled with the prevailing models based on percolation theory. While it is an important step in the right direction, many questions need to be answered to develop a quantitatively predictive theory. Therefore, the dependence of results as function of both MD and DFT model was investigated and it was found that the statistical error in the energy disorder coming from the different representative morphologies was the main contribution to the uncertainty of the calculated mobilities.

In a second part, the work turned to the investigation of the properties of organic-organic interfaces that occur in many multi-layer devices. Utilization of organic materials evolves

7. Conclusion and outlook

in many types of interfaces within electronics devices, *e.g.* organic-organic, organic-inorganic and organic-metallic. To enable reliable analysis of interface processes, a better understanding of the material morphology, *i.e.* the transition from the bulk to the interface domain and the molecular orientation at the interface itself, was investigated. Detailed models were developed for morphologies at organic-organic interfaces of crystalline materials by means of molecular dynamics simulations. From these simulations two main conclusions could be drawn: First, an interface induced disorder was observed to propagate unevenly into the respective crystals depending on their relative orientation, indicating a different stiffness of the corresponding materials. Second, for a few specific choices of surface orientation, stable vacancies at the interface were observed.

Many important challenges remain to develop quantitative models for organic electronics: Future work can combine the two individually studied workflows for charge carrier mobility estimation and interface modeling towards whole device simulations. Additionally, the model needs to be extended to cover a wider range of interfacial combinations including metallic and semiconducting as well as organic and inorganic.

In the last part of the thesis, a model was developed to describe polymer wrapping around single-walled carbon nanotubes. Single-walled carbon nanotubes were found to be promising candidates for many applications in electronics and beyond. Their properties vary with diameter and angular pattern (chirality) so that each type of single-walled carbon nanotube has a unique character. Exploitation of this character may be beneficial for specific applications, though the production of chemically pure single-walled carbon nanotubes types remains challenging. Present day production processes deliver a mixture of many different single-walled carbon nanotubes types. In search of efficient sorting procedures for single-walled carbon nanotubes, this work focused on polymer aided sorting. To reduce the number of costly experiments, the simulation of the polymer wrapping process was modeled.

The model proposed is based on identification of common patterns occurring in the process of polymer wrapping. The model estimates the intrinsic selectivity of the polymers in dependence of the single-walled carbon nanotubes diameter. This was achieved in a multiscale approach, where each polymer is divided into specific building blocks. These are arranged on the nanotube by a recursive iterative method that quickly explores the whole configuration space of the polymer. This process explores the configuration space orders of magnitude faster than straightforward simulation of the wrapping process. The positioning of the polymer on the nanotube leads to changes in the angle between the

building blocks. *Ab-initio* methods were used to estimate the energy for each geometrically possible conformation, which permits a prediction of the relative propensity of a polymer to wrap specific nanotubes. For validation, the model was applied to six different polymers with varying lengths and composition and compared to experimental data. The agreement between experiment and simulation was excellent paving the way for quantitative predictions. Extensions of the model including chirality selectivity are the natural next step.

A. Appendix

A.1. Tables for QM parameters from charge mobility estimation

For completeness, all values obtained in the mobility estimation workflow is listed. The first two Tables A.1 and A.2 show the data for the electronic coupling parameter $\langle J^2 r^2 \rangle$ for HOMO and LUMO coupling, respectively. Afterwards the data for the energy disorder parameter σ is given in Table A.3 for HOMO and in Table A.4 for LUMO.

The results of the charge carrier mobility calculations are listed in Tables A.5 and A.6 for hole and electron mobility, respectively.

Table A.1.: Summary table for calculated electronic coupling for HOMO. For the calculations with BP86 functional together with SV(P) basis set of the amorphous materials an uncertainty $s_{\langle J^2 r^2 \rangle}$ is added obtained by the consideration of different snapshots.

material	N_{mols}	functional/basis	$\langle J^2 r^2 \rangle$ in $eV^2 m^2$	$s_{\langle J^2 r^2 \rangle}$ in %
DEPB	300	BP/SV(P)	0.1973e-22	6.42
	300	B3-LYP/TZVP	0.1946e-22	
	500	BP/SV(P)	0.1864e-22	5.33
mBPD	300	BP/SV(P)	0.1563e-22	8.82
	300	B3-LYP/TZVP	0.5900e-22	
NNP	300	BP/SV(P)	0.1740e-22	7.85
	300	B3-LYP/TZVP	0.5932e-22	
pFFA	300	BP/SV(P)	0.1246e-22	4.54
	300	B3-LYP/TZVP	0.1592e-22	
TPD	300	BP/SV(P)	0.1777e-22	7.48
	300	B3-LYP/TZVP	0.2279e-22	
tetracene	308	BP/SV(P)	1.4422e-22	
	308	B3-LYP/TZVP	2.2316e-22	
pentacene	288	BP/SV(P)	2.8908e-22	
	288	B3-LYP/TZVP	3.8984e-22	

Table A.2.: Summary table for calculated electronic coupling for LUMO. For the calculations with BP86 functional together with SV(P) basis set of the amorphous materials an uncertainty $s_{\langle J^2 r^2 \rangle}$ is added obtained by the consideration of different snapshots.

material	N_{mols}	functional/basis	$\langle J^2 r^2 \rangle$ in $eV^2 m^2$	$s_{\langle J^2 r^2 \rangle}$ in %
DEPB	300	BP/SV(P)	0.2417e-22	6.02
	300	B3-LYP/TZVP	0.2847e-22	
	500	BP/SV(P)	0.2227e-22	3.34
mBPD	300	BP/SV(P)	0.6831e-22	8.13
	300	B3-LYP/TZVP	0.1417e-22	
NNP	300	BP/SV(P)	0.9780e-22	13.34
	300	B3-LYP/TZVP	0.1172e-22	
pFFA	300	BP/SV(P)	0.4206e-22	10.68
	300	B3-LYP/TZVP	0.5723e-22	
TPD	300	BP/SV(P)	0.4000e-22	4.82
	300	B3-LYP/TZVP	0.4765e-22	
tetracene	308	BP/SV(P)	2.3561e-22	
	308	B3-LYP/TZVP	3.7107e-22	
pentacene	288	BP/SV(P)	4.3107e-22	
	288	B3-LYP/TZVP	5.8994e-22	

Table A.3.: Summary table for calculated local energy disorder for HOMO. The amorphous materials include an uncertainty s_σ obtained by the consideration of different snapshots while using BP86 functional together with SV(P) basis set and the dipole environment representation.

material	N_{mols}	func/basis	environment	σ_{local} in eV	s_σ in $\%$
DEPB	300	BP/SV(P)	dipole	0.1355	4.00
	300	BP/SV(P)	ESP	0.1266	
	300	B3-LYP/TZVP	dipole	0.1503	
	300	B3-LYP/TZVP	ESP	0.1474	
	500	BP/SV(P)	dipole	0.1326	2.49
mBPD	300	BP/SV(P)	dipole	0.1058	3.24
	300	BP/SV(P)	ESP	0.1129	
	300	B3-LYP/TZVP	dipole	0.1255	
	300	B3-LYP/TZVP	ESP	0.1294	
NNP	300	BP/SV(P)	dipole	0.1508	3.13
	300	BP/SV(P)	ESP	0.1594	
	300	B3-LYP/TZVP	dipole	0.1741	
	300	B3-LYP/TZVP	ESP	0.1738	
pFFA	300	BP/SV(P)	dipole	0.1202	2.39
	300	BP/SV(P)	ESP	0.1164	
	300	B3-LYP/TZVP	dipole	0.1397	
	300	B3-LYP/TZVP	ESP	0.1348	
TPD	300	BP/SV(P)	dipole	0.1052	4.61
	300	BP/SV(P)	ESP	0.0938	
	300	B3-LYP/TZVP	dipole	0.1224	
	300	B3-LYP/TZVP	ESP	0.1107	
tetracene	308	BP/SV(P)	dipole	0.0273	
	308	BP/SV(P)	ESP	1.2426	
	308	B3-LYP/TZVP	dipole	0.0193	
	308	B3-LYP/TZVP	ESP	1.0284	
pentacene	288	BP/SV(P)	dipole	0.0373	
	288	BP/SV(P)	ESP	4.6330	
	288	B3-LYP/TZVP	dipole	0.0327	
	288	B3-LYP/TZVP	ESP	3.5731	

Table A.4.: Summary table for calculated local energy disorder for LUMO. The amorphous materials include an uncertainty s_σ obtained by the consideration of different snapshots while using BP86 functional together with SV(P) basis set and the dipole environment representation.

material	N_{mols}	func/basis	environment	σ_{local} in eV	s_σ in %
DEPB	300	BP/SV(P)	dipole	0.1613	3.45
	300	BP/SV(P)	ESP	0.1546	
	300	B3-LYP/TZVP	dipole	0.1620	
	300	B3-LYP/TZVP	ESP	0.1614	
	500	BP/SV(P)	dipole	0.1675	3.10
mBPD	300	BP/SV(P)	dipole	0.1124	2.56
	300	BP/SV(P)	ESP	0.1165	
	300	B3-LYP/TZVP	dipole	0.1170	
	300	B3-LYP/TZVP	ESP	0.1168	
NNP	300	BP/SV(P)	dipole	0.0945	4.16
	300	BP/SV(P)	ESP	0.1025	
	300	B3-LYP/TZVP	dipole	0.0958	
	300	B3-LYP/TZVP	ESP	0.1041	
pFFA	300	BP/SV(P)	dipole	0.0979	2.70
	300	BP/SV(P)	ESP	0.0924	
	300	B3-LYP/TZVP	dipole	0.0961	
	300	B3-LYP/TZVP	ESP	0.0929	
TPD	300	BP/SV(P)	dipole	0.1497	3.22
	300	BP/SV(P)	ESP	0.1510	
	300	B3-LYP/TZVP	dipole	0.1662	
	300	B3-LYP/TZVP	ESP	0.1624	
tetracene	308	BP/SV(P)	dipole	0.0317	
	308	BP/SV(P)	ESP	1.2215	
	308	B3-LYP/TZVP	dipole	0.0288	
	308	B3-LYP/TZVP	ESP	1.0082	
pentacene	288	BP/SV(P)	dipole	0.0276	
	288	BP/SV(P)	ESP	4.5289	
	288	B3-LYP/TZVP	dipole	0.0204	
	288	B3-LYP/TZVP	ESP	3.3919	

Table A.5.: Estimated hole mobilities according to Equation 2.5. The reorganization energy λ was taken from Table 4.3 and the average number of hopping partners M from Table 4.4. The data for the electronic coupling parameter $\langle J^2 r^2 \rangle$ was taken from Table A.1 and the energy disorder σ from Table A.3. By the propagation of uncertainty for the parameters $\langle J^2 r^2 \rangle$ and σ for the BP86/SV(P) calculations with dipole environment an uncertainty was obtained according to Equation 4.4.

material	N_{mols}	func/basis	env	μ_{HOMO} in cm^2/Vs	$\Delta\mu$ in %
DEPB	300	BP/SV(P)	dipole	9.0040e-06	61.89
	300	BP/SV(P)	ESP	2.3983e-05	
	300	B3-LYP/TZVP	dipole	1.5173e-06	
	300	B3-LYP/TZVP	ESP	2.1743e-06	
	500	BP/SV(P)	dipole	1.2241e-05	37.13
mBPD	300	BP/SV(P)	dipole	3.1245e-04	32.32
	300	BP/SV(P)	ESP	1.6090e-04	
	300	B3-LYP/TZVP	dipole	1.6972e-04	
	300	B3-LYP/TZVP	ESP	1.1154e-04	
NNP	300	BP/SV(P)	dipole	4.0935e-07	59.63
	300	BP/SV(P)	ESP	1.3542e-07	
	300	B3-LYP/TZVP	dipole	6.0873e-08	
	300	B3-LYP/TZVP	ESP	6.3551e-08	
pFFA	300	BP/SV(P)	dipole	1.2108e-04	29.80
	300	BP/SV(P)	ESP	1.7776e-04	
	300	B3-LYP/TZVP	dipole	1.8085e-05	
	300	B3-LYP/TZVP	ESP	3.1885e-05	
TPD	300	BP/SV(P)	dipole	3.0005e-04	44.27
	300	BP/SV(P)	ESP	7.9550e-04	
	300	B3-LYP/TZVP	dipole	7.2811e-05	
	300	B3-LYP/TZVP	ESP	2.3175e-04	
tetracene	308	BP/SV(P)	dipole	1.9914	
	308	B3-LYP/TZVP	dipole	3.8032	
pentacene	288	BP/SV(P)	dipole	2.1968	
	288	B3-LYP/TZVP	dipole	3.5099	

Table A.6.: Estimated electron mobilities according to Equation 2.5. The reorganization energy λ was taken from Table 4.3 and the average number of hopping partners M from Table 4.4. The data for the electronic coupling parameter $\langle J^2 r^2 \rangle$ was taken from Table A.2 and the energy disorder σ from Table A.4. By the propagation of uncertainty for the parameters $\langle J^2 r^2 \rangle$ and σ for the BP86/SV(P) calculations with dipole environment an uncertainty was obtained according to Equation 4.4.

material	N_{mols}	func/basis	env	μ_{LUMO} in cm^2/Vs	$\Delta\mu$ in %
DEPB	300	BP/SV(P)	dipole	1.2080e-07	74.53
	300	BP/SV(P)	ESP	2.9028e-07	
	300	B3-LYP/TZVP	dipole	1.5873e-07	
	300	B3-LYP/TZVP	ESP	1.7200e-07	
	500	BP/SV(P)	dipole	6.0940e-08	71.94
mBPD	300	BP/SV(P)	dipole	4.1790e-04	28.65
	300	BP/SV(P)	ESP	2.8066e-04	
	300	B3-LYP/TZVP	dipole	5.5411e-05	
	300	B3-LYP/TZVP	ESP	5.6519e-05	
NNP	300	BP/SV(P)	dipole	1.3232e-02	35.23
	300	BP/SV(P)	ESP	6.6484e-03	
	300	B3-LYP/TZVP	dipole	1.4226e-03	
	300	B3-LYP/TZVP	ESP	6.9018e-04	
pFFA	300	BP/SV(P)	dipole	4.7853e-03	25.03
	300	BP/SV(P)	ESP	7.5761e-03	
	300	B3-LYP/TZVP	dipole	7.5872e-03	
	300	B3-LYP/TZVP	ESP	9.8964e-03	
TPD	300	BP/SV(P)	dipole	6.2715e-07	60.04
	300	BP/SV(P)	ESP	5.3331e-07	
	300	B3-LYP/TZVP	dipole	8.6473e-08	
	300	B3-LYP/TZVP	ESP	1.4483e-07	
tetracene	308	BP/SV(P)	dipole	1.6630	
	308	B3-LYP/TZVP	dipole	2.8661	
pentacene	288	BP/SV(P)	dipole	3.6467	
	288	B3-LYP/TZVP	dipole	5.9931	

A.2. Technical excursion: Challenges in workflows on multiple scales

The successful modeling of material properties usually requires to combine different tools acting on different length scales [172–174]. Each software package and each calculation come with many parameters, self written code and scripts typically are undocumented, under continuous changes and without version control. Sometimes, even small changes in the settings can have significant effects on the outcome. But in science the reproducibility is obligatory. This section shows approaches to address this challenge in complex workflows. Standardized methods in work- and dataflow provide a straightforward way to use, explain, re-use and share one's own work.

For the simulations and calculations performed for this thesis, several tools were used basing of different methods and models. Table A.7 gives an overview of the tools and the corresponding methods and models. A detailed description was given in the preceding chapters.

Table A.7.: Models, methods and tools used for the work in this thesis.

Model	Method	Tool
QM all-atom model	DFT	Turbomole
QM all-atom model	DFT	MOPAC
Classical all-atom model	MD	Amber
Classical all-atom model	MD	GROMACS
CG model	coarse-graining	self written code
Continuous model	EMT	analytical formula

Defined workflows on multiple scales ensure a consistent methodology for the calculation of material parameters and properties. The workflows lead step by step to the determination of the desired material property. These workflows typically involve the knowledge of the different tools and their specifications, especially of their data formats. This leads to a number of challenges for a sustainable usage:

- Specific knowledge about all tools

- Interconnection between tools and calculation steps

- Heterogeneous computing requirements for several steps

- Data management between the tools and calculation steps

- Sharing knowledge about workflow within and beyond the own group

These aspects are addressed in the following sections. First, in section A.2.1 interfacing between different simulation steps is discussed, followed by an overview of resource requirements and usage of different software packages in section A.2.2. Afterwards, in section A.2.3, benefits of workflows and workflow engines are presented. Finally a data model for a simulation of molecular systems is outlined in section A.2.4.

A.2.1. Interconnection between different tools

Each software package and script comes with its own interface, data model and file formats. Even common data such as positional data of atoms has different formatting. While the software package Amber, for instance, takes all coordinates in Angstrom, the open source package GROMACS requires nanometer and the commercial code Turbomole uses atomic units. To switch from one to another tool, the data have to be converted and different configuration files have to be created.

The simplest way is to write a script to convert the data from tool A to tool B. Typically each researcher has his own set of wrapper scripts, mostly called by hand. Collections of scripts lead to poorly scalable "all-to-all" converter. Defining workflows can help strengthen the procedures and automatize recurring calculations. This also helps to re-use once written code and scripts.

When interconnectivity is implemented, the next challenge is different requirements of tools towards computing resources; this will be addressed in the next section.

A.2.2. Serial or (massive) parallel - Matching different computing abilities of tools

Depending on the computational costs, *e.g.* the time consumption, to solve a problem and the scalability of the code one can or has to use high performance computing (HPC) clusters for parallel computing or just plain serial computing farms. MD simulations of large molecular systems, for example, require an adequate amount of parallelization. Most MD codes perform sufficiently on message passing interface (MPI) on several hundred cores and more. On the other hand, the DFT code Turbomole is more moderate in scaling,

whereas the high-performance computational chemistry and open source package Pacific Northwest National Laboratory, Washington State, USA), *e.g.* is scaling for monomer calculations of the organic molecule N1,N4-di(naphthalene-1-yl)-N1,N4-diphenylbenzene-1,4-diamine (NNP) up to 512 cores.

These different abilities determine the computing clusters suitable for calculations. In complex workflows, different steps are likely to require other environments. Sometimes one available cluster can process all workflow tasks, but on other occasions workflows have to run on several different clusters and computing environments. Here the management and automation are not as simple anymore. A way to overcome cluster borders and master heterogeneous environments with a unified workflow interface is described in the next section.

A.2.3. Automatized workflows - Sustainability and knowledge transfer within and between the research groups

Often, scientists have access to different computing resources through different institutes or projects. This usually comes with distinct batch systems and also authorization methods. The tool package UNICORE (UNiform Interface to COmputing REsources) addresses exactly this scenario, gives a transparent view and access to heterogeneous resources, offers a centralized storage server and a task manager for heterogeneous computing resources. The UNICORE Rich Client [175] bases on the integrated development environment eclipse and focuses on the interconnection of different computational steps in (complex) workflows.

Based on UNICORE, Ratering *et al.* implemented a GridBean Application Programming Interface [176] and present a "GridBean technology that bridges the gap between the constantly changing basic Grid or e-Science infrastructures and the need of stable application development environments for the Grid users". GridBeans enable the user to write modular workflow steps with defined interfaces to input and output data and program parameters. GridBeans for different tools with similar functionality can be exchanged in a workflow, making workflows more generalized and quickly adaptable. These workflows provide a way of standardization of calculations, straightforward re-usability, sharing and simple knowledge transfer to other scientists.

The MoSGrid Project (Molecular Simulation Grid) [177–179] offers a web service for "both

experienced users and beginners [..] to perform experiments in computational chemistry through this web portal on remote grid resources provided by the academic partners of the project." The users can operate through their preferred internet browser and need no knowledge about the computing resources used in their calculations.

In the Simulation Lab NanoMikro the interconnection between different tools is a steady flow [180]. But efficient workflows include both, an interconnection and data management. Although UNICORE provides a centralized storage and handles the in- and output files, for integration of the computing resources of tools a separate wrapper script has to be written. This can be overcome by using a distinct data model which is described in the following section.

A.2.4. A service-oriented, platform and language-independent framework using data models

There are several approaches to handle data and different data formats. An example for an "all-to-all" converter is the open source tool OpenBabel, a "chemical toolbox designed to speak the many languages of chemical data". OpenBabel is a powerful tool for many file formats. A different approach is the utilization of a common exchange format and wrapper script to and from this format, *e.g.* a convenient file format for chemistry related data is the Chemical Markup Language (CML) [181]. But CML has some limitations on the data since its format is too strict and does not include ways to add workflow specific quantities and parameters.

An integration of different frameworks was developed in this group and published by Bender *et al.* [182] aims at the implementation of domain-specific data models, or rather the ability to generate these models with a service-oriented framework. Similar to computing workflows, the data model is used to enable the data to "flow" through the work.

For the implementation of the framework as a toolkit five major aspects and requirements are identified [182]:

1. "Generic and domain-independent"

2. "Simple meta-modeling environment"

3. "Bridge for access to heterogeneous and distributed resources"

4. "Fully automatic code generation"

5. "Interoperability with grid and cloud middleware"

Utilizing the framework and data workflow in scientific workflows requires only understanding of the data needed within the workflow. Knowing the details, a data model can be freely specified. The framework then enables the available storage system to store data and handle the access by applications through transparent web services. As storage back-end several options are possible, *e.g.* data bases, plain text files or cloud storage services.

In the end, the data is stored on a central or distributed storage with defined web interfaces for communication. The access is independent of the running storage system and databases implemented on the server. This is achieved by standardized web services which can be addressed with all major programming and scripting languages. In an advanced case, the communication with the web services can be implemented in the software packages themselves and the data exchange is shifted totally into the code getting input data from the storage instead from the input files. No file format converters would be necessary anymore.

A.3. Tools used for this thesis

All data plots were generated with the open source package root (CERN, Geneva, Switzerland) and consistent colored and styled with the open source vector graphic package Inkscape (http://inkscape.org/en/), *e.g.* all axis titles were redone in inkscape. All pictures of molecules were created using visual molecular dynamics (VMD) package (University of Illinois, Urbana-Champaign).

The thesis was written in the open source package eclipse platform (Apache Software Foundation) using the addon texlipse. The bibliography was managed with the open source software zotero (Center for History and New Media, George Mason University). Furthermore, the Grammar Checker (Ginger Software, Inc.) was used.

B. Nomenclature

ACPYPE .... AnteChamber PYthon Parser interfacE

AMOEBA .... Atomic Multipole Optimized Energetics for Biomolecular Applications

AMOLED .... Active-Matrix Organic Light-Emitting Diode

CC BY-SA 3.0 ...... License: Creative Commons Attribution-Share Alike 3.0 Unported, http://creativecommons.org/licenses/by-sa/3.0/legalcode

CCDC .... Cambridge Crystallographic Data Centre

CG-PWM .... Coarse-Grained Polymer Wrapping Model

CML .... Chemical Markup Language

CoMoCAT .... Co/Mo catalyst

DEPB .... 1,1-bis-(4,4'-diethylaminophenyl)-4,4-diphenyl-1,3,butadiene

DNA .... Deoxyribonucleic acid

ESP .... Electrostatic Potential Charge

FET .... Field Effect Transistor

flop .... floating point operations per second

fs .... femto second(s)

GAFF .... Generalized Amber Force Field

B. Nomenclature

GGA .... Generalized gradient approximations

HF .... Hartree-Fock

HiPco .... SWCNT production by high pressure CO disproportionation of Fe(CO)

HOMO .... Highest Occupied Molecular Orbital

HPC .... High Performance Computing

HT .... High temperature

IC .... Integrated Circuit

LT .... Low temperature

LUMO .... Lowest Unoccupied Molecular Orbital

mBPD .... N4,N4'-di(biphenyl-3-yl)-N4,N4-diphenylbiphenyl-4,4'-diamine

MD .... Molecular Dynamics

Mflop .... Megaflop $= 10^6$ flops $= 10^6$ floating point operations per second

MNDO .... Modified Neglect of Diatomic Overlap

MOPAC .... Molecular Orbital PACkage

MOSFET .... Metal-Oxide-Semiconductor Field-Effect Transistor

MPI .... Message Passing Interface

NNP .... N1,N4-di(naphthalene-1-yl)-N1,N4-diphenylbenzene-1,4-diamine

ns .... nano second(s)

OLED .... Organic Light Emitting Diode

OPV .... Organic Photovoltaic

pbc .... periodic boundary condition

100

PEN .... pentacene

pFFA .... N,N'-bis-[9,9-dimethyl-2-fluorenyl]-N,N'-diphenyl-9,9-dimethylfluorene-
2,7-diamine

Pflop .... Pflop $= 10^{15}$ flops

PME .... Particle-Mesh Ewald

PTCDA .... perylene-3,4,9,10-tetracarboxylic dianhydride

QM .... Quantum Mechanics

RESP .... Restricted Electrostatic Potential charges

SWCNT .... Single-Walled Carbon Nanotube

TET .... tetracene

TFT .... Thin-Film Transistor

TOF .... time-of-flight

TPD .... N,N'-diphenyl-N,N'-bis-(3-methylphenylene)-1,1'-diphenyl-4,4'-diamine

UNICORE .... UNiform Interface to COmputing REsources

Wgsimon .... http://commons.wikimedia.org/wiki/User:Wgsimon

[?]

C. Bibliography

[1] Julius Edgar Lilienfeld. Device for controlling electric current, March 1933. US Patent 1,900,018.

[2] Julius Edgar Lilienfeld. Method and apparatus for controlling electric currents, January 1930. US Patent 1,745,175.

[3] Julius Edgar Lilienfeld. Amplifier for electric currents, September 1932. US Patent 1,877,140.

[4] Oskar Heil. Improvements in or relating to electrical amplifiers and other control arrangements and devices, December 1935. CIB: H01L29/00; H01L29/78; H01L29/786; H02G3/08; H03F3/16.

[5] J. Haynes and W. Shockley. Investigation of hole injection in transistor action. *Physical Review*, 75(4):691–691, February 1949.

[6] Peter J. Denning. Third generation computer systems. *ACM Computing Surveys*, 3(4):175–216, December 1971.

[7] 2013 Nobel Media AB. The nobel prize in physics 1956, 1956.

[8] G.E. Moore. Cramming more components onto integrated circuits. *Proceedings of the IEEE*, 86(1):82–85, January 1998.

[9] O. Richard, F. Iacopi, H. Bender, and G. Beyer. Sidewall damage in silica-based low-k material induced by different patterning plasma processes studied by energy filtered and analytical scanning TEM. *Microelectronic Engineering*, 84(3):517–523, March 2007.

[10] Scott Mueller. *Upgrading and repairing PCs*. Que, Indianapolis, Ind., 2006.

[11] Jack J. Dongarra. The LINPACK benchmark: An explanation. In E.N. Houstis, T.S. Papatheodorou, and C.D. Polychronopoulos, editors, *Supercomputing*, volume 297 of *Lecture Notes in Computer Science*, pages 456–474. Springer Berlin Heidelberg, 1988.

[12] Juan Manuel Rodriguez, Cristian Mateos, and Alejandro Zunino. Are smartphones really useful for scientific computing? In Francisco Cipolla-Ficarra, Kim Veltman, Domen Verber, Miguel Cipolla-Ficarra, and Florian Kammller, editors, *Advances in New Technologies, Interactive Interfaces and Communicability*, volume 7547 of *Lecture Notes in Computer Science*, pages 38–47. Springer Berlin Heidelberg, 2012.

[13] 2013 The Royal Swedish Academy of Sciences. The nobel prize in chemistry 2013 - press release, September 2013.

Bibliography

[14] C. W. Tang and S. A. VanSlyke. Organic electroluminescent diodes. *Applied Physics Letters*, 51(12):913–915, September 1987.

[15] Dong-Un Jin, Jae-Sup Lee, Tae-Woong Kim, Sung-Guk An, Denis Straykhilev, Young-Shin Pyo, Hyung-Sik Kim, Dong-Bum Lee, Yeon-Gon Mo, Hye-Dong Kim, and Ho-Kyoon Chung. Distinguished paper: World-largest (6.5) flexible full color top emission AMOLED display on plastic film and its bending properties. *SID Symposium Digest of Technical Papers*, 40(1):983–985, 2009.

[16] M. F. L. De Volder, S. H. Tawfick, R. H. Baughman, and A. J. Hart. Carbon nanotubes: Present and future commercial applications. *Science*, 339(6119):535–539, January 2013.

[17] Anatoliy N. Sokolov, Sule Atahan-Evrenk, Rajib Mondal, Hylke B. Akkerman, Roel S. Snchez-Carrera, Sergio Granados-Focil, Joshua Schrier, Stefan C.B. Mannsfeld, Arjan P. Zoombelt, Zhenan Bao, and Aln Aspuru-Guzik. From computational discovery to experimental characterization of a high hole mobility organic crystal. *Nature Communications*, 2:437–1–437–8, August 2011.

[18] Choongkeun Lee, Robert Waterland, and Karl Sohlberg. Prediction of charge mobility in amorphous organic materials through the application of hopping theory. *Journal of Chemical Theory and Computation*, 7(8):2556–2567, August 2011.

[19] Dae Sung Chung, Jong-Soo Lee, Jing Huang, Angshuman Nag, Sandrine Ithurria, and Dmitri V. Talapin. Low voltage, hysteresis free, and high mobility transistors from all-inorganic colloidal nanocrystals. *Nano Letters*, 12(4):1813–1820, April 2012.

[20] David Beljonne, Jerome Cornil, Luca Muccioli, Claudio Zannoni, Jean-Luc Bredas, and Frederic Castet. Electronic processes at organic-organic interfaces: Insight from modeling and implications for opto-electronic devices. *Chemistry of Materials*, 23(3):591–609, February 2011.

[21] Brian A. Gregg and Mark C. Hanna. Comparing organic to inorganic photovoltaic cells: Theory, experiment, and simulation. *Journal of Applied Physics*, 93(6):3605, 2003.

[22] Nir Tessler, Yevgeni Preezant, Noam Rappaport, and Yohai Roichman. Charge transport in disordered organic materials and its relevance to thin-film devices: A tutorial review. *Advanced Materials*, 21(27):2741–2761, July 2009.

[23] R Saito, G Dresselhaus, and M. S Dresselhaus. *Physical properties of carbon nanotubes*. Imperial College Press, London, 1998.

[24] Martin Cinke, Jing Li, Bin Chen, Alan Cassell, Lance Delzeit, Jie Han, and M Meyyappan. Pore structure of raw and purified HiPco single-walled carbon nanotubes. *Chemical Physics Letters*, 365(1-2):69–74, October 2002.

[25] B. Kitiyanan, W.E. Alvarez, J.H. Harwell, and D.E. Resasco. Controlled production of single-wall carbon nanotubes by catalytic decomposition of CO on bimetallic CoMo catalysts. *Chemical Physics Letters*, 317(3-5):497–503, February 2000.

[26] Mark C. Hersam. Progress towards monodisperse single-walled carbon nanotubes. *Nature Nanotechnology*, 3(7):387–394, July 2008.

[27] G. Zhang, P. Qi, X. Wang, Y. Lu, X. Li, R. Tu, S. Bangsaruntip, D. Mann, L. Zhang, and H. Dai. Selective etching of metallic carbon nanotubes by gas-phase reaction. *Science*, 314(5801):974–977, November 2006.

[28] Paul W. K. Rothemund. Folding DNA to create nanoscale shapes and patterns. *Nature*, 440(7082):297–302, March 2006.

[29] Claudia Caddeo, Claudio Melis, Luciano Colombo, and Alessandro Mattoni. Understanding the helical wrapping of poly(3-hexylthiophene) on carbon nanotubes. *The Journal of Physical Chemistry C*, 114(49):21109–21113, December 2010.

[30] Jia Gao, Maria Antonietta Loi, Elton Jose Figueiredo de Carvalho, and Maria Cristina dos Santos. Selective wrapping and supramolecular structures of PolyfluoreneCarbon nanotube hybrids. *ACS Nano*, 5(5):3993–3999, May 2011.

[31] Widianta Gomulya, Guadalupe Diaz Costanzo, Elton J. Figueiredo de Carvalho, Satria Zulkarnaen Bisri, Vladimir Derenskyi, Martin Fritsch, Nils Frhlich, Sybille Allard, Pavlo Gordiichuk, Andreas Herrmann, Siewert Jan Marrink, Maria Cristina dos Santos, Ulrich Scherf, and Maria Antonietta Loi. Semiconducting single-walled carbon nanotubes on demand by polymer wrapping. *Advanced Materials*, 25(21):2948–2956, June 2013.

[32] Youn K. Kang, One-Sun Lee, Pravas Deria, Sang Hoon Kim, Tae-Hong Park, Dawn A. Bonnell, Jeffery G. Saven, and Michael J. Therien. Helical wrapping of single-walled carbon nanotubes by water soluble poly(p-phenyleneethynylene). *Nano Letters*, 9(4):1414–1418, April 2009.

[33] Fabien A. Lemasson, Timo Strunk, Peter Gerstel, Frank Hennrich, Sergei Lebedkin, Christopher Barner-Kowollik, Wolfgang Wenzel, Manfred M. Kappes, and Marcel Mayor. Selective dispersion of single-walled carbon nanotubes with specific chiral indices by poly(n-decyl-2,7-carbazole). *Journal of the American Chemical Society*, 133(4):652–655, February 2011.

[34] Adrian Nish, Jeong-Yuan Hwang, James Doig, and Robin J. Nicholas. Highly selective dispersion of single-walled carbon nanotubes using aromatic polymers. *Nature Nanotechnology*, 2(10):640–646, September 2007.

[35] Syamal S. Tallury and Melissa A. Pasquinelli. Molecular dynamics simulations of flexible polymer chains wrapping single-walled carbon nanotubes. *The Journal of Physical Chemistry B*, 114(12):4122–4129, April 2010.

[36] Christopher D. Von Bargen, Christopher M. MacDermaid, One-Sun Lee, Pravas Deria, Michael J. Therien, and Jeffery G. Saven. Origins of the helical wrapping of phenyleneethynylene polymers about single-walled carbon nanotubes. *The Journal of Physical Chemistry B*, pages 12953–12965, August 2013.

Bibliography

[37] Chenyu Wei. Radius and chirality dependent conformation of polymer molecule at nanotube interface. *Nano Letters*, 6(8):1627–1631, August 2006.

[38] Huiliang Wang, Jianguo Mei, Peng Liu, Kristin Schmidt, Gonzalo Jimnez-Oss, Slvia Osuna, Lei Fang, Christopher J. Tassone, Arjan Pieter Zoombelt, Anatoliy N. Sokolov, Kendall N. Houk, Michael F. Toney, and Zhenan Bao. Scalable and selective dispersion of semiconducting arc-discharged carbon nanotubes by Dithiafulvalene/Thiophene copolymers for thin film transistors. *ACS Nano*, 7(3):2659–2668, March 2013.

[39] Allen Miller and Elihu Abrahams. Impurity conduction at low concentrations. *Physical Review*, 120(3):745–755, November 1960.

[40] R. A. Marcus. On the theory of oxidation-reduction reactions involving electron transfer. i. *The Journal of Chemical Physics*, 24(5):966–978, May 1956.

[41] Ralph H. Young. Dipolar lattice model of disorder in random media analytical evaluation of the gaussian disorder model. *Philosophical Magazine Part B*, 72(4):435–457, October 1995.

[42] R. Coehoorn, W. Pasveer, P. Bobbert, and M. Michels. Charge-carrier concentration dependence of the hopping mobility in organic materials with gaussian disorder. *Physical Review B*, 72(15):155206-1–155206–20, October 2005.

[43] Vadim Rodin, Gabriele Nelles, Florian von Wrochem, Velimir Meded, Angela Poschlad, and Wolfgang Wenzel. A first principles effective medium model for mobility in amorphous organic semiconductors. *submitted*, May 2014.

[44] Nicolas Berton, Fabien Lemasson, Angela Poschlad, Velimir Meded, Frank Tristram, Wolfgang Wenzel, Frank Hennrich, Manfred M. Kappes, and Marcel Mayor. Selective dispersion of large-diameter semiconducting single-walled carbon nanotubes with pyridine-containing copolymers. *Small*, 10(2):360367, January 2014.

[45] Peter Gerstel, Stefanie Klumpp, Frank Hennrich, Angela Poschlad, Velimir Meded, Eva Blasco, Wolfgang Wenzel, Manfred M. Kappes, and Christopher Barner-Kowollik. Highly selective dispersion of single-walled carbon nanotubes via polymer wrapping: A combinatorial study via modular conjugation. *ACS Macro Letters*, 3(1):10–15, January 2014.

[46] Roland Faller. Coarse-grained modeling of soft condensed matter. *Physical Chemistry Chemical Physics*, 11(12):1867–1868, March 2009.

[47] Holger Gohlke and M.F. Thorpe. A natural coarse graining for simulating large biomolecular motion. *Biophysical Journal*, 91(6):2115–2120, September 2006.

[48] Young C. Kim and Gerhard Hummer. Coarse-grained models for simulations of multiprotein complexes: Application to ubiquitin binding. *Journal of Molecular Biology*, 375(5):1416–1433, February 2008.

[49] Pavel A. Golubkov and Pengyu Ren. Generalized coarse-grained model based on point multipole and gay-berne potentials. *The Journal of Chemical Physics*, 125(6):064103–1–064103–11, August 2006.

[50] Giuseppe Milano and Florian Mller-Plathe. Mapping atomistic simulations to mesoscopic models: A systematic coarse-graining procedure for vinyl polymer chains. *The Journal of Physical Chemistry B*, 109(39):18609–18619, October 2005.

[51] Florian Mller-Plathe. Coarse-graining in polymer simulation: From the atomistic to the mesoscopic scale and back. *ChemPhysChem*, 3(9):754–769, September 2002.

[52] Yanting Wang, W. G. Noid, Pu Liu, and Gregory A. Voth. Effective force coarse-graining. *Physical Chemistry Chemical Physics*, 11(12):2002–2015, February 2009.

[53] Sergei Izvekov and Gregory A. Voth. A multiscale coarse-graining method for biomolecular systems. *The Journal of Physical Chemistry B*, 109(7):2469–2473, February 2005.

[54] Nobel Media AB 2013. The Nobel Prize in Chemistry 1992, 1992.

[55] Frank H. Allen. The cambridge structural database: a quarter of a million crystal structures and rising. *Acta Crystallographica Section B Structural Science*, 58(3):380–388, May 2002.

[56] Clare F. Macrae, Paul R. Edgington, Patrick McCabe, Elna Pidcock, Greg P. Shields, Robin Taylor, Matthew Towler, and Jacco van de Streek. Mercury : visualization and analysis of crystal structures. *Journal of Applied Crystallography*, 39(3):453–457, June 2006.

[57] Tobias Neumann, Denis Danilov, Christian Lennartz, and Wolfgang Wenzel. Modeling disordered morphologies in organic semiconductors. *Journal of Computational Chemistry*, 34(31):2716–2725, December 2013.

[58] Erik Lindahl, Berk Hess, and David van der Spoel. GROMACS 3.0: a package for molecular simulation and trajectory analysis. *Molecular modeling annual*, 7(8):306–317, 2001.

[59] David Van Der Spoel, Erik Lindahl, Berk Hess, Gerrit Groenhof, Alan E. Mark, and Herman J. C. Berendsen. GROMACS: fast, flexible, and free. *Journal of Computational Chemistry*, 26(16):1701–1718, December 2005.

[60] H.J.C. Berendsen, D. van der Spoel, and R. van Drunen. GROMACS: a message-passing parallel molecular dynamics implementation. *Computer Physics Communications*, 91(1-3):43–56, September 1995.

[61] Berk Hess, Carsten Kutzner, David van der Spoel, and Erik Lindahl. GROMACS 4: Algorithms for highly efficient, load-balanced, and scalable molecular simulation. *Journal of Chemical Theory and Computation*, 4(3):435–447, March 2008.

[62] Stephen F. Nelsen, Silas C. Blackstock, and Yaesil Kim. Estimation of inner shell marcus terms for amino nitrogen compounds by molecular orbital calculations. *Journal of the American Chemical Society*, 109(3):677–682, February 1987.

Bibliography

[63] Per-Olov Lowdin. On the non-orthogonality problem connected with the use of atomic wave functions in the theory of molecules and crystals. *The Journal of Chemical Physics*, 18(3):365–375, March 1950.

[64] V. Stehr, J. Pfister, R. F. Fink, B. Engels, and C. Deibel. First-principles calculations of anisotropic charge-carrier mobilities in organic semiconductor crystals. *Physical Review B*, 83(15):155208–1–155208–14, April 2011.

[65] Slawomir Braun, William R. Salaneck, and Mats Fahlman. Energy-level alignment at Organic/Metal and Organic/Organic interfaces. *Advanced Materials*, 21(14-15):1450–1472, April 2009.

[66] Hisao Ishii, Kiyoshi Sugiyama, Eisuke Ito, and Kazuhiko Seki. Energy level alignment and interfacial electronic structures at Organic/Metal and Organic/Organic interfaces. *Advanced Materials*, 11(8):605–625, June 1999.

[67] H. Najafov, B. Lee, Q. Zhou, L. C. Feldman, and V. Podzorov. Observation of long-range exciton diffusion in highly ordered organic semiconductors. *Nature Materials*, 9(11):938–943, November 2010.

[68] Jean-Luc Brdas, Joseph E. Norton, Jrme Cornil, and Veaceslav Coropceanu. Molecular understanding of organic solar cells: The challenges. *Accounts of Chemical Research*, 42(11):1691–1699, November 2009.

[69] X.-Y. Zhu, Q. Yang, and M. Muntwiler. Charge-transfer excitons at organic semiconductor surfaces and interfaces. *Accounts of Chemical Research*, 42(11):1779–1787, November 2009.

[70] Stijn Verlaak, David Beljonne, David Cheyns, Cedric Rolin, Mathieu Linares, Frdric Castet, Jrme Cornil, and Paul Heremans. Electronic structure and geminate pair energetics at OrganicOrganic interfaces: The case of Pentacene/C_{60} heterojunctions. *Advanced Functional Materials*, 19(23):3809–3814, December 2009.

[71] Angela Poschlad, Velimir Meded, Robert Maul, and Wolfgang Wenzel. Different interface orientations of pentacene and PTCDA induce different degrees of disorder. *Nanoscale Research Letters*, 7(1):248–1–248–5, May 2012.

[72] Yao-Tsung Fu, Chad Risko, and Jean-Luc Brdas. Intermixing at the pentacene-fullerene bilayer interface: A molecular dynamics study. *Advanced Materials*, 25(6):878–882, February 2013.

[73] Thorsten Vehoff, Bjorn Baumeier, Alessandro Troisi, and Denis Andrienko. Charge transport in organic crystals: Role of disorder and topological connectivity. *Journal of the American Chemical Society*, 132(33):11702–11708, August 2010.

[74] Jeramy D. Zimmerman, Xin Xiao, Christopher Kyle Renshaw, Siyi Wang, Vyacheslav V. Diev, Mark E. Thompson, and Stephen R. Forrest. Independent control of bulk and interfacial morphologies of small molecular weight organic heterojunction solar cells. *Nano Letters*, 12(8):4366–4371, August 2012.

[75] J. Cornil, S. Verlaak, N. Martinelli, A. Mityashin, Y. Olivier, T. Van Regemorter, G. DAvino, L. Muccioli, C. Zannoni, F. Castet, D. Beljonne, and P. Heremans. Exploring the energy landscape of the charge transport levels in organic semiconductors at the molecular scale. *Accounts of Chemical Research*, 46(2):434–443, February 2013.

[76] Sumio Iijima. Helical microtubules of graphitic carbon. *Nature*, 354:56–58, November 1991.

[77] Sumio Iijima and Toshinari Ichihashi. Single-shell carbon nanotubes of 1-nm diameter. *Nature*, 363(6430):603–605, June 1993.

[78] Noriaki Hamada, Shin-ichi Sawada, and Atsushi Oshiyama. New one-dimensional conductors: Graphitic microtubules. *Physical Review Letters*, 68(10):1579–1581, March 1992.

[79] Xin Lu and Zhongfang Chen. Curved pi-conjugation, aromaticity, and the related chemistry of small fullerenes (<c $_{60}$) and single-walled carbon nanotubes. *Chemical Reviews*, 105(10):3643–3696, October 2005.

[80] C. White, D. Robertson, and J. Mintmire. Helical and rotational symmetries of nanoscale graphitic tubules. *Physical Review B*, 47(9):5485–5488, March 1993.

[81] Teri Wang Odom, Jin-Lin Huang, Philip Kim, and Charles M. Lieber. Atomic structure and electronic properties of single-walled carbon nanotubes. *Nature*, 391(6662):62–64, January 1998.

[82] Max M. Shulaker, Gage Hills, Nishant Patil, Hai Wei, Hong-Yu Chen, H.-S. Philip Wong, and Subhasish Mitra. Carbon nanotube computer. *Nature*, 501(7468):526–530, September 2013.

[83] Qing Cao, Shu-jen Han, George S. Tulevski, Yu Zhu, Darsen D. Lu, and Wilfried Haensch. Arrays of single-walled carbon nanotubes with full surface coverage for high-performance electronics. *Nature Nanotechnology*, 8(3):180–186, January 2013.

[84] N. W. Shi Kam. Carbon nanotubes as multifunctional biological transporters and near-infrared agents for selective cancer cell destruction. *Proceedings of the National Academy of Sciences*, 102(33):11600–11605, August 2005.

[85] Wei-Fang Du, Lee Wilson, John Ripmeester, Rgent Dutrisac, Benoit Simard, and Stphane Dnomme. Investigation of the pore structure of as-prepared and purified HiPco single-walled carbon nanotubes by N_2 /Ar AdsorptionImplication for H_2 storage. *Nano Letters*, 2(4):343–346, April 2002.

[86] Pavel Nikolaev, Michael J Bronikowski, R.Kelley Bradley, Frank Rohmund, Daniel T Colbert, K.A Smith, and Richard E Smalley. Gas-phase catalytic growth of single-walled carbon nanotubes from carbon monoxide. *Chemical Physics Letters*, 313(1-2):91–97, November 1999.

[87] M. Yudasaka, H. Kataura, T. Ichihashi, L.-C. Qin, S. Kar, and S. Iijima. Diameter enlargement of HiPco single-wall carbon nanotubes by heat treatment. *Nano Letters*, 1(9):487–489, September 2001.

Bibliography

[88] Cheol-Min Yang, Katsumi Kaneko, Masako Yudasaka, and Sumio Iijima. Effect of purification on pore structure of HiPco single-walled carbon nanotube aggregates. *Nano Letters*, 2(4):385–388, April 2002.

[89] Theerapol Thurakitseree, Erik Einarsson, Rong Xiang, Pei Zhao, Shinya Aikawa, Shohei Chiashi, Junichiro Shiomi, and Shigeo Maruyama. Diameter controlled chemical vapor deposition synthesis of single-walled carbon nanotubes. *Journal of Nanoscience and Nanotechnology*, 12(1):370–376, January 2012.

[90] M. J. O'Connell. Band gap fluorescence from individual single-walled carbon nanotubes. *Science*, 297(5581):593–596, July 2002.

[91] S. M. Bachilo. Structure-assigned optical spectra of single-walled carbon nanotubes. *Science*, 298(5602):2361–2366, December 2002.

[92] K. Hata. Water-assisted highly efficient synthesis of impurity-free single-walled carbon nanotubes. *Science*, 306(5700):1362–1364, November 2004.

[93] Jeffrey A. Fagan, Matthew L. Becker, Jaehun Chun, and Erik K. Hobbie. Length fractionation of carbon nanotubes using centrifugation. *Advanced Materials*, 20(9):1609–1613, May 2008.

[94] Michael S. Arnold, Alexander A. Green, James F. Hulvat, Samuel I. Stupp, and Mark C. Hersam. Sorting carbon nanotubes by electronic structure using density differentiation. *Nature Nanotechnology*, 1(1):60–65, October 2006.

[95] M. Zheng. Structure-based carbon nanotube sorting by sequence-dependent DNA assembly. *Science*, 302(5650):1545–1548, November 2003.

[96] Hang Qian, Cheng Tian, Jinwen Yu, Fei Guo, Ming-Sen Zheng, Wen Jiang, Quan-Feng Dong, and Chengde Mao. Self-assembly of DNA nanotubes with defined diameters and lengths. *Small*, 10(5):855–858, November 2013.

[97] Xiaomin Tu, Suresh Manohar, Anand Jagota, and Ming Zheng. DNA sequence motifs for structure-specific recognition and separation of carbon nanotubes. *Nature*, 460:250–253, July 2009.

[98] S. M. Douglas, J. J. Chou, and W. M. Shih. DNA-nanotube-induced alignment of membrane proteins for NMR structure determination. *Proceedings of the National Academy of Sciences*, 104(16):6644–6648, April 2007.

[99] Robert R. Johnson, A. T. Charlie Johnson, and Michael L. Klein. The nature of DNA-BaseCarbon-Nanotube interactions. *Small*, 6(1):31–34, January 2010.

[100] Fabien Lemasson, Nicolas Berton, Jana Tittmann, Frank Hennrich, Manfred M. Kappes, and Marcel Mayor. Polymer library comprising fluorene and carbazole homo- and copolymers for selective single-walled carbon nanotubes extraction. *Macromolecules*, 45(2):713–722, January 2012.

[101] Peter Gerstel, Stefanie Klumpp, Frank Hennrich, Ozcan Altintas, Thomas R. Eaton, Marcel Mayor, Christopher Barner-Kowollik, and Manfred M. Kappes. Selective dispersion of single-walled carbon nanotubes via easily accessible conjugated click polymers. *Polymer Chemistry*, 3(8):1966–1970, May 2012.

[102] Pravas Deria, Christopher D. Von Bargen, Jean-Hubert Olivier, Amar S. Kumbhar, Jeffery G Saven, and Michael J. Therien. Single-handed helical wrapping of single-walled carbon nanotubes by chiral, ionic, semiconducting polymers. *Journal of the American Chemical Society*, pages 16220–16234, September 2013.

[103] Hiroaki Ozawa, Natsuko Ide, Tsuyohiko Fujigaya, Yasuro Niidome, and Naotoshi Nakashima. Supramolecular hybrid of metal nanoparticles and semiconducting single-walled carbon nanotubes wrapped by a fluorene-carbazole copolymer. *Chemistry - A European Journal*, 17(48):13438–13444, November 2011.

[104] Florian Jakubka, Stefan P. Schiel, Sebastian Martin, Jan M. Englert, Frank Hauke, Andreas Hirsch, and Jana Zaumseil. Effect of polymer molecular weight and solution parameters on selective dispersion of single-walled carbon nanotubes. *ACS Macro Letters*, 1(7):815–819, July 2012.

[105] Bin Mu, Thomas P. McNicholas, Jingqing Zhang, Andrew J. Hilmer, Zhong Jin, Nigel F. Reuel, Jong-Ho Kim, Kyungsuk Yum, and Michael S. Strano. A StructureFunction relationship for the optical modulation of phenyl boronic acid-grafted, polyethylene glycol-wrapped single-walled carbon nanotubes. *Journal of the American Chemical Society*, 134(42):17620–17627, October 2012.

[106] Eugen S. Zarudnev, Alexander M. Plokhotnichenko, Victor S. Leontiev, Igor A. Levitsky, and Victor A. Karachevtsev. Unusual aggregation of poly(rC)-wrapped carbon nanotubes in aqueous suspension induced by cationic porphyrin. *Journal of Materials Chemistry*, 22(21):1079510804, March 2012.

[107] Masayoshi Tange, Toshiya Okazaki, and Sumio Iijima. Selective extraction of large-diameter single-wall carbon nanotubes with specific chiral indices by poly(9,9-dioctylfluorene-*alt*-benzothiadiazole). *Journal of the American Chemical Society*, 133(31):11908–11911, August 2011.

[108] Michael J. O'Connell, Peter Boul, Lars M. Ericson, Chad Huffman, Yuhuang Wang, Erik Haroz, Cynthia Kuper, Jim Tour, Kevin D. Ausman, and Richard E. Smalley. Reversible water-solubilization of single-walled carbon nanotubes by polymer wrapping. *Chemical Physics Letters*, 342(3-4):265–271, July 2001.

[109] Jeong-Yuan Hwang, Adrian Nish, James Doig, Sigrid Douven, Chun-Wei Chen, Li-Chyong Chen, and Robin J. Nicholas. Polymer structure and solvent effects on the selective dispersion of single-walled carbon nanotubes. *Journal of the American Chemical Society*, 130(11):3543–3553, March 2008.

[110] Wenhui Yi, Andrey Malkovskiy, Qinghui Chu, Alexei P. Sokolov, Marisabel Lebron Colon, Michael Meador, and Yi Pang. Wrapping of single-walled carbon nanotubes by a -conjugated polymer:

Bibliography

The role of polymer conformation-controlled size selectivity. *The Journal of Physical Chemistry B*, 112(39):12263–12269, October 2008.

[111] Jiyao Wang, Yuqing Deng, and Benoit Roux. Absolute binding free energy calculations using molecular dynamics simulations with restraining potentials. *Biophysical Journal*, 91(6):2798–2814, October 2006.

[112] Yuichi Kato, Yasuro Niidome, and Naotoshi Nakashima. Thermodynamics of the exchange of solubilizers on single-walled carbon nanotubes. *Chemistry Letters*, 40(7):730–732, June 2011.

[113] Yuichi Kato, Ayaka Inoue, and Naotoshi Nakashima. Thermodynamics on soluble carbon nanotubes: How do dna molecules replace surfactants on carbon nanotubes? *Scientific Reports*, 2:730–732, October 2012.

[114] Y. J. Wang. Noncovalent modification of carbon nanotubes by conjugated polymer: A theoretical study. *International Journal of Quantum Chemistry*, 111(14):3897–3903, November 2010.

[115] H. C. Longuet-Higgins and L. Salem. The alternation of bond lengths in long conjugated chain molecules. *Proceedings of the Royal Society A: Mathematical, Physical and Engineering Sciences*, 251(1265):172–185, May 1959.

[116] M. Born and R. Oppenheimer. Zur quantentheorie der molekeln. *Annalen der Physik*, 389(20):457–484, 1927.

[117] P. Hohenberg and W Kohn. Inhomogeneous electron gas. *Physical Review*, 136(3B):B864–B871, November 1964.

[118] David M. Hayes and Peter A. Kollman. Electrostatic potentials of proteins. 1. carboxypeptidase a. *Journal of the American Chemical Society*, 98(11):3335–3345, May 1976.

[119] David M. Hayes and Peter A. Kollman. Electrostatic potentials of proteins. 2. role of electrostatics in a possible catalytic mechanism for carboxypeptidase a. *Journal of the American Chemical Society*, 98(24):7811–7816, November 1976.

[120] U. Chandra Singh and Peter A. Kollman. An approach to computing electrostatic charges for molecules. *Journal of Computational Chemistry*, 5(2):129–145, April 1984.

[121] Brent H. Besler, Kenneth M. Merz, and Peter A. Kollman. Atomic charges derived from semiempirical methods. *Journal of Computational Chemistry*, 11(4):431–439, May 1990.

[122] Christopher I. Bayly, Piotr Cieplak, Wendy Cornell, and Peter A. Kollman. A well-behaved electrostatic potential based method using charge restraints for deriving atomic charges: the RESP model. *The Journal of Physical Chemistry*, 97(40):10269–10280, October 1993.

[123] Reinhart Ahlrichs, Filipp Furche, Christof Haettig, Willem M. Klopper, Marek Sierka, and Florian Weigend. Turbomole, 1989.

[124] Reinhart Ahlrichs, Michael Br, Marco Hser, Hans Horn, and Christoph Klmel. Electronic structure calculations on workstation computers: The program system turbomole. *Chemical Physics Letters*, 162(3):165–169, October 1989.

[125] Florian Weigend and Reinhart Ahlrichs. Balanced basis sets of split valence, triple zeta valence and quadruple zeta valence quality for h to rn: Design and assessment of accuracy. *Physical Chemistry Chemical Physics*, 7(18):3297–3305, August 2005.

[126] Christof Hättig and Florian Weigend. CC2 excitation energy calculations on large molecules using the resolution of the identity approximation. *The Journal of Chemical Physics*, 113(13):5154–5161, October 2000.

[127] Ansgar Schafer, Hans Horn, and Reinhart Ahlrichs. Fully optimized contracted gaussian basis sets for atoms li to kr. *The Journal of Chemical Physics*, 97(4):2571, 1992.

[128] Ansgar Schafer, Christian Huber, and Reinhart Ahlrichs. Fully optimized contracted gaussian basis sets of triple zeta valence quality for atoms li to kr. *The Journal of Chemical Physics*, 100(8):5829–5835, April 1994.

[129] C. Roothaan. New developments in molecular orbital theory. *Reviews of Modern Physics*, 23(2):69–89, April 1951.

[130] Michael J. S. Dewar and Walter Thiel. Ground states of molecules. 38. the MNDO method. approximations and parameters. *Journal of the American Chemical Society*, 99(15):4899–4907, June 1977.

[131] Michael J. S. Dewar, Michael L. McKee, and Henry S. Rzepa. MNDO parameters for third period elements. *Journal of the American Chemical Society*, 100(11):3607–3607, May 1978.

[132] James J. P. Stewart. MOPAC: a semiempirical molecular orbital program. *Journal of Computer-Aided Molecular Design*, 4(1):1–103, March 1990.

[133] James J. P. Stewart. Optimization of parameters for semiempirical methods v: Modification of NDDO approximations and application to 70 elements. *Journal of Molecular Modeling*, 13(12):1173–1213, October 2007.

[134] Wendy D. Cornell, Piotr Cieplak, Christopher I. Bayly, Ian R. Gould, Kenneth M. Merz, David M. Ferguson, David C. Spellmeyer, Thomas Fox, James W. Caldwell, and Peter A. Kollman. A second generation force field for the simulation of proteins, nucleic acids, and organic molecules. *Journal of the American Chemical Society*, 117(19):5179–5197, May 1995.

[135] William L. Jorgensen, David S. Maxwell, and Julian Tirado-Rives. Development and testing of the OPLS all-atom force field on conformational energetics and properties of organic liquids. *Journal of the American Chemical Society*, 118(45):11225–11236, January 1996.

Bibliography

[136] Bernard R. Brooks, Robert E. Bruccoleri, Barry D. Olafson, David J. States, S. Swaminathan, and Martin Karplus. CHARMM: a program for macromolecular energy, minimization, and dynamics calculations. *Journal of Computational Chemistry*, 4(2):187–217, 1983.

[137] Falk May, Mustapha Al-Helwi, Bjrn Baumeier, Wolfgang Kowalsky, Evelyn Fuchs, Christian Lennartz, and Denis Andrienko. Design rules for charge-transport efficient host materials for phosphorescent organic light-emitting diodes. *Journal of the American Chemical Society*, 134(33):13818–13822, August 2012.

[138] Junmei Wang, Romain M. Wolf, James W. Caldwell, Peter A. Kollman, and David A. Case. Development and testing of a general amber force field. *Journal of Computational Chemistry*, 25(9):1157–1174, July 2004.

[139] Gl Altnba zpnar, Wolfgang Peukert, and Timothy Clark. An improved generalized AMBER force field (GAFF) for urea. *Journal of Molecular Modeling*, 16(9):1427–1440, August 2010.

[140] Shichi Nos. A molecular dynamics method for simulations in the canonical ensemble. *Molecular Physics*, 52(2):255–268, June 1984.

[141] William Hoover. Canonical dynamics: Equilibrium phase-space distributions. *Physical Review A*, 31(3):1695–1697, March 1985.

[142] Glenn J. Martyna, Michael L. Klein, and Mark Tuckerman. NoseHoover chains: The canonical ensemble via continuous dynamics. *The Journal of Chemical Physics*, 97(4):2635–2643, August 1992.

[143] H. J. C. Berendsen, J. P. M. Postma, W. F. van Gunsteren, A. DiNola, and J. R. Haak. Molecular dynamics with coupling to an external bath. *The Journal of Chemical Physics*, 81(8):3684–3690, October 1984.

[144] Henrik G. Petersen. Accuracy and efficiency of the particle mesh ewald method. *The Journal of Chemical Physics*, 103(9):3668–3679, September 1995.

[145] M. Parrinello and A. Rahman. Crystal structure and pair potentials: A molecular-dynamics study. *Physical Review Letters*, 45(14):1196–1199, October 1980.

[146] Shuichi Nos and M.L. Klein. Constant pressure molecular dynamics for molecular systems. *Molecular Physics*, 50(5):1055–1076, December 1983.

[147] Romelia Salomon-Ferrer, David A. Case, and Ross C. Walker. An overview of the amber biomolecular simulation package. *Wiley Interdisciplinary Reviews: Computational Molecular Science*, 3(2):198–210, March 2013.

[148] Alan W Sousa da Silva and Wim F Vranken. ACPYPE - AnteChamber PYthon parser interfacE. *BMC Research Notes*, 5(1):367–1–367–8, July 2012.

[149] Junmei Wang, Wei Wang, Peter A. Kollman, and David A. Case. Automatic atom type and bond type perception in molecular mechanical calculations. *Journal of Molecular Graphics and Modelling*, 25(2):247–260, October 2006.

[150] J. Mort and G. Pfister. Photoelectronic properties of disordered organic solids: Molecularly-doped polymers. *Polymer-Plastics Technology and Engineering*, 12(2):89–139, January 1979.

[151] Lay-Lay Chua, Jana Zaumseil, Jui-Fen Chang, Eric C.-W. Ou, Peter K.-H. Ho, Henning Sirringhaus, and Richard H. Friend. General observation of n-type field-effect behaviour in organic semiconductors. *Nature*, 434(7030):194–199, March 2005.

[152] M. Abkowtz and D. M. Pai. Comparison of the drift mobility measured under transient and steady-state conditions in a prototypical hopping system. *Philosophical Magazine Part B*, 53(3):193–216, March 1986.

[153] R. B. Campbell, J. M. Robertson, and J. Trotter. The crystal structure of hexacene, and a revision of the crystallographic data for tetracene. *Acta Crystallographica*, 15(3):289–290, March 1962.

[154] Makoto Yoneya, Masahiro Kawasaki, and Masahiko Ando. Molecular dynamics simulations of pentacene thin films: The effect of surface on polymorph selection. *Journal of Materials Chemistry*, 20(46):10397–10402, August 2010.

[155] Karl Pearson. Note on regression and inheritance in the case of two parents. *Proceedings of the Royal Society of London (1854-1905)*, 58(-1):240–242, January 1895.

[156] Yasuhiko Shirota and Hiroshi Kageyama. Charge carrier transporting molecular materials and their applications in devices. *Chemical Reviews*, 107(4):953–1010, April 2007.

[157] Kenji Okumoto and Yasuhiko Shirota. Development of new hole-transporting amorphous molecular materials for organic electroluminescent devices and their charge-transport properties. *Materials Science and Engineering: B*, 85(2-3):135–139, August 2001.

[158] T Mori, E Sugimura, and T Mizutani. Estimate of hole mobilities of some organic photoconducting materials using the time-of-flight method. *Journal of Physics D: Applied Physics*, 26(3):452–455, March 1993.

[159] E. L. Frankevich and E. I. Balabanov. Investigation of current carrier drift in organic substances (tetracene). *physica status solidi (b)*, 14(2):523–529, 1966.

[160] V.Y. Butko, X. Chi, and A.P. Ramirez. Free-standing tetracene single crystal field effect transistor. *Solid State Communications*, 128(11):431–434, December 2003.

[161] Hagen Klauk, Marcus Halik, Ute Zschieschang, Gunter Schmid, Wolfgang Radlik, and Werner Weber. High-mobility polymer gate dielectric pentacene thin film transistors. *Journal of Applied Physics*, 92(9):5259, 2002.

[162] Tommie W. Kelley, Dawn V. Muyres, Paul F. Baude, Terry P. Smith, and Todd D. Jones. High performance organic thin film transistors. *MRS Proceedings*, 771, January 2003.

Bibliography

[163] S. F. Nelson, Y.-Y. Lin, D. J. Gundlach, and T. N. Jackson. Temperature-independent transport in high-mobility pentacene transistors. *Applied Physics Letters*, 72(15):1854, 1998.

[164] H. Klauk, D.J. Gundlach, J.A. Nichols, and T.N. Jackson. Pentacene organic thin-film transistors for circuit and display applications. *IEEE Transactions on Electron Devices*, 46(6):1258–1263, June 1999.

[165] Antonio Facchetti. Semiconductors for organic transistors. *Materials Today*, 10(3):28–37, March 2007.

[166] Tetsuya Ogawa, Kiyoshi Kuwamoto, Seiji Isoda, Takashi Kobayashi, and Norbert Karl. 3,4:9,10-perylenetetracarboxylic dianhydride (PTCDA) by electron crystallography. *Acta Crystallographica Section B Structural Science*, 55(1):123–130, February 1999.

[167] P. Sehati, S. Braun, and M. Fahlman. Energy level alignment in Au/pentacene/PTCDA trilayer stacks. *Chemical Physics Letters*, 583:38–41, September 2013.

[168] R. B. Campbell, J. M. Robertson, and J. Trotter. The crystal and molecular structure of pentacene. *Acta Crystallographica*, 14(7):705–711, July 1961.

[169] R.G Endres, C.Y Fong, L.H Yang, G Witte, and Ch Wll. Structural and electronic properties of pentacene molecule and molecular pentacene solid. *Computational Materials Science*, 29(3):362–370, March 2004.

[170] Yu-Wu Wang, Horng-Long Cheng, Yi-Kai Wang, Tang-Hsiang Hu, Jia-Chong Ho, Cheng-Chung Lee, Tan-Fu Lei, and Ching-Fa Yeh. Influence of measuring environment on the electrical characteristics of pentacene-based thin film transistors. *Thin Solid Films*, 467(1-2):215–219, November 2004.

[171] Jay W. Ponder, Chuanjie Wu, Pengyu Ren, Vijay S. Pande, John D. Chodera, Michael J. Schnieders, Imran Haque, David L. Mobley, Daniel S. Lambrecht, Robert A. DiStasio, Martin Head-Gordon, Gary N. I. Clark, Margaret E. Johnson, and Teresa Head-Gordon. Current status of the AMOEBA polarizable force field. *The Journal of Physical Chemistry B*, 114(8):2549–2564, March 2010.

[172] J A Elliott. Novel approaches to multiscale modelling in materials science. *International Materials Reviews*, 56(4):207–225, July 2011.

[173] T.E. Karakasidis and C.A. Charitidis. Multiscale modeling in nanomaterials science. *Materials Science and Engineering: C*, 27(5-8):1082–1089, September 2007.

[174] Stefan Bozic, Ivan Kondov, Velimir Meded, and Wolfgang Wenzel. UNICORE based workflows for the simulation of organic light-emitting diodes. In *UNICORE Summit 2012: proceedings, 30 - 31 May 2012, Dresden, Germany*, volume 15 of *IAS Series*, pages 15–25. Forschungszentrum Julich, Zentralbibliothek, Julich, 2012.

[175] Bastian Demuth, Bernd Schuller, Sonja Holl, Jason Daivandy, Andre Giesler, Valentina Huber, and Sulev Sild. The UNICORE rich client: Facilitating the automated execution of scientific workflows. pages 238–245. IEEE, December 2010.

[176] Ralf Ratering, Alexander Lukichev, Morris Riedel, Daniel Mallmann, A. Vanni, C. Cacciari, S. Lanzarini, K. Benedyczak, M. Borcz, R. Kluszcynski, Piotr Bala, and Gert Ohme. GridBeans: support e-science and grid applications. pages 45–45. IEEE, December 2006.

[177] G Birkenheuer, D Blunk, S Breuers, A Brinkmann, I dos Santos Vieira, G Fels, S Gesing, R Grunzke, S Herres-Pawlis, O Kohlbacher, N Kruber, J Krger, U Lang, L Packschies, R Mller-Pfefferkorn, P Schfer, H-G Schmalz, T Steinke, K-D Warzecha, and M Wewior. MoSGrid a molecular simulation grid as a new tool in computational chemistry, biology and material science. *Journal of Cheminformatics*, 3(1):P14, April 2011.

[178] Sandra Gesing, Richard Grunzke, Jens Krger, Georg Birkenheuer, Martin Wewior, Patrick Schfer, Bernd Schuller, Johannes Schuster, Sonja Herres-Pawlis, Sebastian Breuers, kos Balask, Miklos Kozlovszky, Anna Szikszay Fabri, Lars Packschies, Peter Kacsuk, Dirk Blunk, Thomas Steinke, Andr Brinkmann, Gregor Fels, Ralph Mller-Pfefferkorn, Ren Jkel, and Oliver Kohlbacher. A single sign-on infrastructure for science gateways on a use case for structural bioinformatics. *Journal of Grid Computing*, 10(4):769–790, December 2012.

[179] Richard Grunzke, Sebastian Breuers, Sandra Gesing, Sonja Herres-Pawlis, Martin Kruse, Dirk Blunk, Luis dela Garza, Lars Packschies, Patrick Schfer, Charlotta Schrfe, Tobias Schlemmer, Thomas Steinke, Bernd Schuller, Ralph Mller-Pfefferkorn, Ren Jkel, Wolfgang E. Nagel, Malcolm Atkinson, and Jens Krger. Standards-based metadata management for molecular simulations: METADATA MANAGEMENT. *Concurrency and Computation: Practice and Experience*, September 2013.

[180] Ivan Kondov, Robert Maul, Konstantin Klenin, Martin Brieg, Angela Poschlad, Alexej Bagrets, Velimir Meded, and Stefan Bozic. Multiscale materials and biomolecular simulations at simulation lab NanoMikro. *Proceedings:(SimLabs KIT 2010); Karlsruhe, Germany, November 29-30, 2010*, page 5, 2011.

[181] Peter Murray-Rust, Henry S. Rzepa, and Michael Wright. Development of chemical markup language (CML) as a system for handling complex chemical content. *New Journal of Chemistry*, 25(4):618–634, March 2001.

[182] Andreas Bender, Angela Poschlad, Stefan Bozic, and Ivan Kondov. A service-oriented framework for integration of domain-specific data models in scientific workflows. *Procedia Computer Science*, 18:1087–1096, January 2013.

D. List of publications

D.1. Articles

1. V. Rodin, G. Nelles, F. von Wrochem , V. Meded, D. Danilov, A. Poschlad, W. Wenzel; A First Principles Effective Medium Model for Mobility in Amorphous Organic Semiconductors, (submitted)

2. P. Gerstel, S. Klumpp, F. Hennrich, A. Poschlad, V. Meded, E. Blasco, W. Wenzel, M. M. Kappes and C. Barner-Kowollik; Highly Selective Dispersion of Single-Walled Carbon Nanotubes via Polymer Wrapping: A Combinatorial Study via Modular Conjugation, *ACS Macro Letters*, 2014, 3 (1): 10-15. doi: 10.1021/mz400472q

3. N. Berton, F. Lemasson, A. Poschlad, V. Meded, F. Tristram, W. Wenzel, F. Hennrich, M.M. Kappes and M. Mayor; Selective Dispersion of Large-Diameter Semiconducting Single-Walled Carbon Nanotubes with Pyridine-Containing Copolymers. *Small*, 2014, 10: 360-367.
   doi: 10.1002/smll.201301295

4. A. Bender, A. Poschlad, S. Bozic, I. Kondov; A Service-oriented Framework for Integration of Domain-specific Data Models in Scientific Workflows, *Procedia Computer Science*, 2013, 18: 1087-1096. doi: 10.1016/j.procs.2013.05.274

5. A. Poschlad, V. Meded, R. Maul, W. Wenzel; Different interface orientations of pentacene and PTCDA induce different degrees of disorder, *Nanoscale Research Letters*, 2012, 7: 248. doi: 10.1186/1556-276X-7-248

E. Acknowledgement

---

[1]web: http://www.bw-grid.de